

# ENGINEERING OF BIOMATERIALS

INŻYNIERIA BIOMATERIAŁÓW

JOURNAL OF POLISH SOCIETY FOR BIOMATERIALS AND FACULTY OF MATERIALS SCIENCE AND CERAMICS AGH-UST

CZASOPISMO POLSKIEGO STOWARZYSZENIA BIOMATERIAŁÓW I WYDZIAŁU INŻYNIERII MATERIAŁOWEJ I CERAMIKI AGH

**Number 166**

Numer 166

**Volume XXV**

Rocznik XXV

**Year 2022**

(Issue 3)

Rok 2022

(Zeszyt 3)

**ISSN 1429-7248**

**PUBLISHER:**

WYDAWCA:

**Polish Society  
for Biomaterials  
in Krakow**

Polskie

Stowarzyszenie

Biomateriałów

w Krakowie

**EDITORIAL  
COMMITTEE:**

KOMITET

REDAKCYJNY:

**Editor-in-Chief**

Redaktor naczelny

**Elżbieta Pamuła**

**Editor**

Redaktor

**Patrycja**

**Domalik-Pyzik**

**Secretary of editorial**

Sekretarz redakcji

**Design**

Projekt

**Katarzyna Trała**

**ADDRESS OF  
EDITORIAL OFFICE:**

ADRES REDAKCJI:

**AGH-UST**

**30/A3, Mickiewicz Av.**

**30-059 Krakow, Poland**

Akademia

Górnico-Hutnicza

al. Mickiewicza 30/A-3

30-059 Kraków

**Issue: 250 copies**

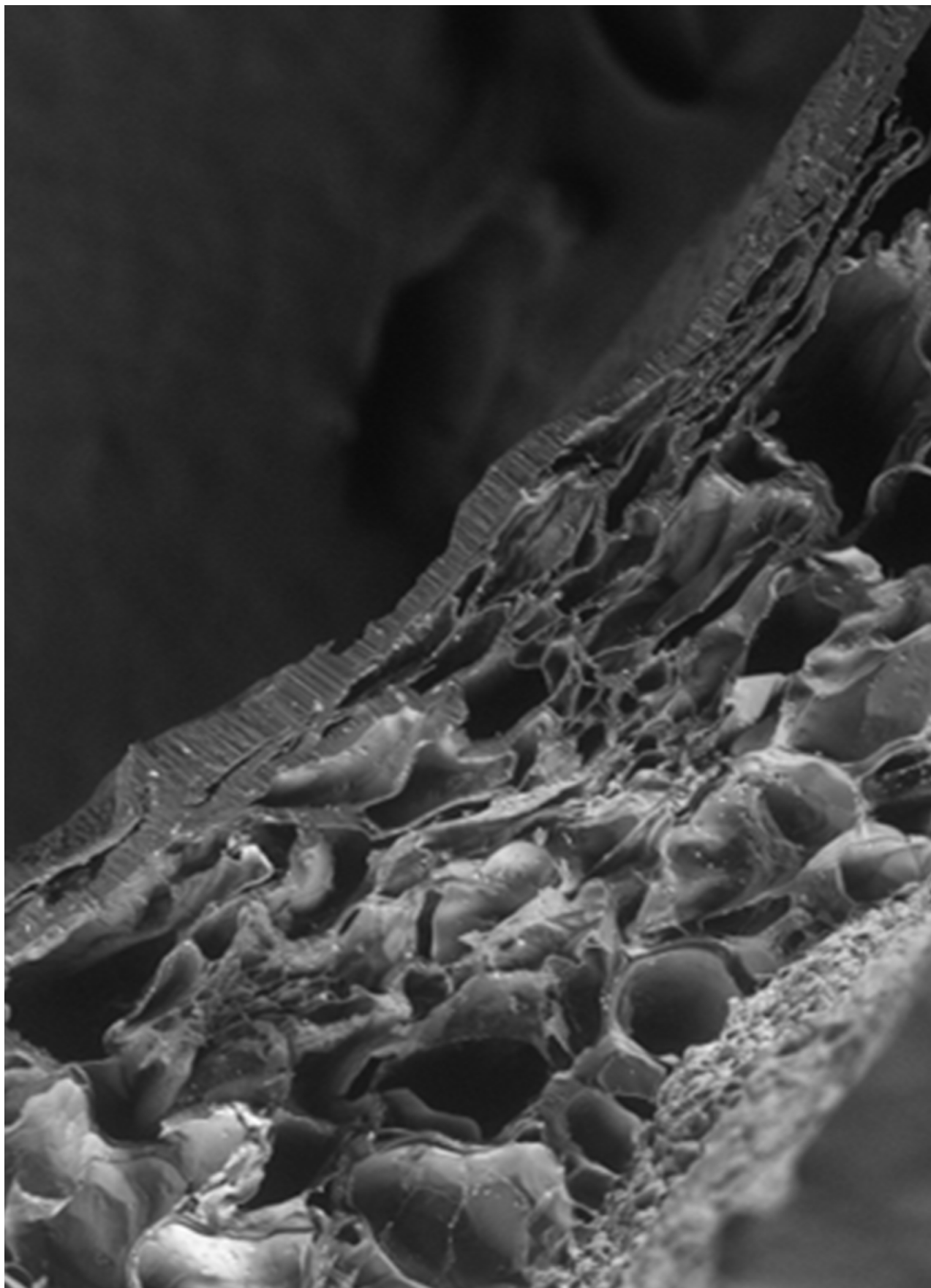
Nakład: 250 egz.

**Scientific Publishing  
House AKAPIT**

Wydawnictwo Naukowe

AKAPIT

e-mail: [wn@akapit.krakow.pl](mailto:wn@akapit.krakow.pl)



**EDITORIAL BOARD  
KOMITET REDAKCYJNY**

**EDITOR-IN-CHIEF**

Elżbieta Pamuła - AGH UNIVERSITY OF SCIENCE AND TECHNOLOGY, KRAKOW, POLAND

**EDITOR**

Patrycja Domalik-Pyzik - AGH UNIVERSITY OF SCIENCE AND TECHNOLOGY, KRAKOW, POLAND

**INTERNATIONAL EDITORIAL BOARD  
MIĘDZYNARODOWY KOMITET REDAKCYJNY**

Iulian Antoniac - UNIVERSITY POLITEHNICA OF BUCHAREST, ROMANIA

Lucie Bacakova - ACADEMY OF SCIENCE OF THE CZECH REPUBLIC, PRAGUE, CZECH REPUBLIC

Romuald Będziński - UNIVERSITY OF ZIELONA GÓRA, POLAND

Marta Błażewicz - AGH UNIVERSITY OF SCIENCE AND TECHNOLOGY, KRAKOW, POLAND

Stanisław Błażewicz - AGH UNIVERSITY OF SCIENCE AND TECHNOLOGY, KRAKOW, POLAND

Wojciech Chrzanowski - UNIVERSITY OF SYDNEY, AUSTRALIA

Jan Ryszard Dąbrowski - BIAŁYSTOK TECHNICAL UNIVERSITY, POLAND

Timothy Douglas - LANCASTER UNIVERSITY, UNITED KINGDOM

Christine Dupont - UNIVERSITÉ CATHOLIQUE DE LOUVAIN, BELGIUM

Matthias Epple - UNIVERSITY OF DUISBURG-ESSEN, GERMANY

Robert Hurt - BROWN UNIVERSITY, PROVIDENCE, USA

James Kirkpatrick - JOHANNES GUTENBERG UNIVERSITY, MAINZ, GERMANY

Ireneusz Kotela - CENTRAL CLINICAL HOSPITAL OF THE MINISTRY OF THE INTERIOR AND ADMINISTR. IN WARSAW, POLAND

Małgorzata Lewandowska-Szumieł - MEDICAL UNIVERSITY OF WARSAW, POLAND

Jan Marciniak - SILESIA UNIVERSITY OF TECHNOLOGY, ZABRZE, POLAND

Ion N. Mihailescu - NATIONAL INSTITUTE FOR LASER, PLASMA AND RADIATION PHYSICS, BUCHAREST, ROMANIA

Sergey Mikhalovsky - UNIVERSITY OF BRIGHTON, UNITED KINGDOM

Stanisław Mitura - TECHNICAL UNIVERSITY OF LIBEREC, CZECH REPUBLIC

Piotr Niedzielski - TECHNICAL UNIVERSITY OF LODZ, POLAND

Abhay Pandit - NATIONAL UNIVERSITY OF IRELAND, GALWAY, IRELAND

Stanisław Pielka - WROCLAW MEDICAL UNIVERSITY, POLAND

Vehid Salih - UCL EASTMAN DENTAL INSTITUTE, LONDON, UNITED KINGDOM

Jacek Składzień - JAGIELLONIAN UNIVERSITY, COLLEGIUM MEDICUM, KRAKOW, POLAND

Andrei V. Stanishevsky - UNIVERSITY OF ALABAMA AT BIRMINGHAM, USA

Anna Ślósarczyk - AGH UNIVERSITY OF SCIENCE AND TECHNOLOGY, KRAKOW, POLAND

Tadeusz Trzaska - UNIVERSITY SCHOOL OF PHYSICAL EDUCATION, POZNAŃ, POLAND

Dimitris Tsipas - ARISTOTLE UNIVERSITY OF THESSALONIKI, GREECE

## Wskazówki dla autorów

1. Prace do opublikowania w kwartalniku „Engineering of Biomaterials / Inżynieria Biomateriałów” przyjmowane będą wyłącznie w języku angielskim.

2. Wszystkie nadsyłane artykuły są recenzowane.

3. Materiały do druku prosimy przysyłać za pomocą systemu online ([www.biomaterials.pl](http://www.biomaterials.pl)).

4. Struktura artykułu:

• TYTUŁ • Autorzy i instytucje • Streszczenie (200-250 słów) • Słowa kluczowe (4-6) • Wprowadzenie • Materiały i metody • Wyniki i dyskusja • Wnioski • Podziękowania • Piśmiennictwo

5. Autorzy przesyłają pełną wersję artykułu, łącznie z ilustracjami, tabelami, podpisami i literaturą w jednym pliku. Artykuł w tej formie przesyłany jest do recenzentów. Dodatkowo autorzy proszeni są o przesłanie materiałów ilustracyjnych (rysunki, schematy, fotografie, wykresy) w oddzielnych plikach (format np. .jpg, .gif, .tiff, .bmp). Rozdzielczość rysunków min. 300 dpi. Wszystkie rysunki i wykresy powinny być czarno-białe lub w odcieniach szarości i ponumerowane cyframi arabskimi. W tekście należy umieścić odnośniki do rysunków i tabel.

6. Na końcu artykułu należy podać wykaz piśmiennictwa w kolejności cytowania w tekście i kolejno ponumerowany.

7. Redakcja zastrzega sobie prawo wprowadzenia do opracowań autorskich zmian terminologicznych, poprawek redakcyjnych, stylistycznych, w celu dostosowania artykułu do norm przyjętych w naszym czasopiśmie. Zmiany i uzupełnienia merytoryczne będą dokonywane w uzgodnieniu z autorem.

8. Opinia lub uwagi recenzentów będą przekazywane Autorowi do ustosunkowania się. Nie dostarczenie poprawionego artykułu w terminie oznacza rezygnację Autora z publikacji pracy w naszym czasopiśmie.

9. Za publikację artykułów redakcja nie płaci honorarium autorskiego.

10. Adres redakcji:

Czasopismo

„Engineering of Biomaterials / Inżynieria Biomateriałów”

Akademia Górniczo-Hutnicza im. St. Staszica

Wydział Inżynierii Materiałowej i Ceramiki

al. Mickiewicza 30/A-3, 30-059 Kraków

tel. (48) 12 617 44 48, 12 617 25 61

e-mail: [epamula@agh.edu.pl](mailto:epamula@agh.edu.pl), [kabe@agh.edu.pl](mailto:kabe@agh.edu.pl)

Szczegółowe informacje dotyczące przygotowania manuskryptu oraz procedury recenzowania dostępne są na stronie internetowej czasopisma:

[www.biomaterials.pl](http://www.biomaterials.pl)

## Instructions for authors

1. Papers for publication in quarterly journal „Engineering of Biomaterials / Inżynieria Biomateriałów” should be written in English.

2. All articles are reviewed.

3. Manuscripts should be submitted to editorial office through online submission system ([www.biomaterials.pl](http://www.biomaterials.pl)).

4. A manuscript should be organized in the following order:

• TITLE • Authors and affiliations • Abstract (200-250 words) • Keywords (4-6) • Introduction • Materials and Methods • Results and Discussion • Conclusions • Acknowledgements • References

5. All illustrations, figures, tables, graphs etc. preferably in black and white or grey scale should be additionally sent as separate electronic files (format .jpg, .gif, .tiff, .bmp). High-resolution figures are required for publication, at least 300 dpi. All figures must be numbered in the order in which they appear in the paper and captioned below. They should be referenced in the text. The captions of all figures should be submitted on a separate sheet.

6. References should be listed at the end of the article. Number the references consecutively in the order in which they are first mentioned in the text.

7. The Editors reserve the right to improve manuscripts on grammar and style and to modify the manuscripts to fit in with the style of the journal. If extensive alterations are required, the manuscript will be returned to the authors for revision.

8. Opinion or notes of reviewers will be transferred to the author. If the corrected article will not be supplied on time, it means that the author has resigned from publication of work in our journal.

9. Editorial does not pay author honorarium for publication of article.

10. Address of editorial office:

Journal

„Engineering of Biomaterials / Inżynieria Biomateriałów”

AGH University of Science and Technology

Faculty of Materials Science and Ceramics

30/A-3, Mickiewicz Av., 30-059 Krakow, Poland

tel. (48) 12) 617 44 48, 12 617 25 61

e-mail: [epamula@agh.edu.pl](mailto:epamula@agh.edu.pl), [kabe@agh.edu.pl](mailto:kabe@agh.edu.pl)

Detailed information concerning manuscript preparation and review process are available at the journal's website:

[www.biomaterials.pl](http://www.biomaterials.pl)





# 32<sup>nd</sup> Biomaterials in Medicine and Veterinary Medicine Annual Conference

12 – 15 October 2023 Rytro, Poland

SAVE THE DATE

12-15

OCTOBER  
2023

[www.biomat.agh.edu.pl](http://www.biomat.agh.edu.pl)



REGISTER  
AND  
SUBMIT  
AN ABSTRACT



## SPIS TREŚCI CONTENTS

<p>FABRICATION OF FILTER MEMBRANE          OF ORGANIC COMPOUND TO PROTECT          THE UPPER RESPIRATORY TRACT          FROM VIRAL AND BACTERIAL INFECTIONS,          INCLUDING SARS-COV-2, COMPLIANT          WITH FFP2 STANDARD          NATALIA BRZEZIŃSKA, MACIEJ PYZA,          ANNA KŁECZEK, KAROLINA KULIŃSKA,          JADWIGA GABOR, ŻANETA GARCZYK-MUNDAŁA,          ANDRZEJ SWINAREW</p>	<b>2</b>
<p>COMPOSITE SCAFFOLDS ENRICHED WITH          CALCIUM CARBONATE MICROPARTICLES          LOADED WITH EPIGALLOCATECHIN GALLATE          FOR BONE TISSUE REGENERATION          KRZYSZTOF PIETRYGA, ANCA-ALEXANDRA          PANAITE, ELŻBIETA PAMUŁA</p>	<b>12</b>
<p>VASCULAR STENTS – MATERIALS          AND MANUFACTURING TECHNOLOGIES          KLAUDIA MALISZ, BEATA ŚWIECZKO-ŻUREK</p>	<b>22</b>
<p>POLYLACTIDE-BASED COMPOSITE          MATERIALS FOR 3D PRINTING AND          MEDICAL APPLICATIONS - THE EFFECT          OF BASALT AND SILICON DIOXIDE ADDITION          MACIEJ PYZA, NATALIA BRZEZIŃSKA,          KAROLINA KULIŃSKA, JADWIGA GABOR,          ADRIAN BARYLSKI, KRZYSZTOF ANIOŁEK,          ŻANETA GARCZYK-MUNDAŁA,          KAYODE ADEBESIN, ANDRZEJ SWINAREW</p>	<b>29</b>

# FABRICATION OF FILTER MEMBRANE OF ORGANIC COMPOUND TO PROTECT THE UPPER RESPIRATORY TRACT FROM VIRAL AND BACTERIAL INFECTIONS, INCLUDING SARS-CoV-2, COMPLIANT WITH FFP2 STANDARD

NATALIA BRZEZIŃSKA<sup>1\*</sup> , MACIEJ PYZA<sup>1</sup> , ANNA KŁECZEK<sup>1</sup> , KAROLINA KULIŃSKA<sup>2</sup> , JADWIGA GABOR<sup>1</sup> , ŻANETA GARCZYK-MUNDAŁA<sup>1</sup> , ANDRZEJ SWINAREW<sup>1,2</sup> 

<sup>1</sup> FACULTY OF SCIENCE AND TECHNOLOGY, UNIVERSITY OF SILESIA, 75 PUŁKU PIECHOTY 1A, 41-500 CHORZÓW, POLAND

<sup>2</sup> INSTITUTE OF SPORT SCIENCE, THE JERZY KUKUCZKA ACADEMY OF PHYSICAL EDUCATION, MIKOŁOWSKA 72A, 40-065 KATOWICE, POLAND

\*E-MAIL: NATALIA.BRZEZINSKA9@OP.PL

## Abstract

*Bacteria, viruses, and other pathogens in the surrounding environment are biological threat to human health and life. The development of various diseases in the world, as well as the pandemic caused by the rapid spread of the SARS-CoV-2 virus, have increased the demand for the use of upper respiratory protection devices. Out of concern for the natural environment, the aim of this work was to develop an innovative solution i.e. the FFP3 filtering membrane made of an organic compound. First, preliminary tests of the FFP2 mask were carried out to assess the chemical composition, morphological structure - fibers geometry, thickness, density, and arrangement. The FTIR analysis study was conducted to confirm that the main chemical in the mask was polypropylene (PP) and high-density polyethylene (HDPE). Optical, confocal microscopy and computer microtomography studies showed the fibers structure. They were densely arranged and their thickness was less than 1 den. The fiber structure of the FFP2 mask was also compared before and after immersing in betulin, an organic compound obtained from birch bark via the Soxhlet extraction. In addition, the assessment of microbiological activity was made on the reference strain Escherichia coli ATCC 25922, and the anti-inflammatory activity on normal human skin fibroblasts on polycarbonate with betulin. The studies showed that betulin supported the material antibacterial and anti-inflammatory properties.*

**Keywords:** face masks, viral and bacterial infections, betulin, filtering membrane, FFP2 standard

[Engineering of Biomaterials 166 (2022) 2-11]

doi:10.34821/eng.biomat.166.2022.2-11

Submitted: 2022-12-31, Accepted: 2023-02-24, Published: 2023-02-28



Copyright © 2022 by the authors. Some rights reserved. Except otherwise noted, this work is licensed under <https://creativecommons.org/licenses/by/4.0>

## Introduction

Bacterial and viral infections pose a real threat to human health and life. In current times, the need for the use of upper respiratory protection devices has increased significantly due to the rapid spread of the SARS-CoV-2 virus around the world which is highly contagious and dangerous. The virus is one of the  $\beta$ -coronaviruses that causes a contagious respiratory disease called Covid-19. It is characterized by a round, near-oval shape and has a diameter of 0.06-0.14  $\mu\text{m}$ . The SARS-CoV-2, like other RNA viruses, can evolve genetically with the development of mutations over time, resulting in variants that may have different characteristics from the original virus strain [1]. During the ongoing pandemic, several cases of SARS-CoV-2 have been singled out, only a few of which have been recognized according to the World Health Organization (WHO) as variants of concern in terms of both the impact on public health and the spread rate. According to the WHO epidemiological data as of 22 June 2021, 4 variants of SARS-CoV-2 have been detected since the pandemic beginning: Alpha, Beta, Gamma, and Delta. As of 22/06/21, according to WHO, the Alpha variant has spread to 170 countries, the Beta variant to 199, the Gamma variant to 71, and the Delta variant to 85. The global case fatality rate for Covid-19 is 2.2%, according to WHO estimates [2]. It should also be mentioned that new mutations of the virus may still appear and therefore differ in the structure and course of the disease [3]. The SARS-CoV-2 virus is transmitted by the droplet route. The infection can occur not only through contact with an infected person, but also through exposure to the environment in which the sick individual has previously lived. This was proven by a study by N. van Doremalen et al. who showed that SARS-CoV-2 virions suspended as an aerosol in an environment with a temperature of 21-23°C and a relative humidity of 65% was still infectious 3 hours after spraying. It also turned out that the SARS-CoV-2 virus was able to survive on different types of surfaces - e.g. on copper for about 4 hours, up to 24 hours on cardboard and up to 72 hours on stainless steel or plastic [4].

To protect the population, it is necessary to maintain an appropriate social distance and use masks with high filtration efficiency. Their function is to trap airborne particles (natural or man-made) as well as biological organisms, e.g. bacteria, viruses, fungi, or other pathogens [5]. Respiratory masks equipped with a suitable filtering membrane can effectively protect the respiratory system [6].

There is a variety of masks available on the medical market. There are simple surgical masks which are designed to protect the wearer from the spread of microorganisms, loosely fitted to the wearer's face as well as FFP3/N95 masks used as protection against inhalation of small airborne particles. Each of these devices is also characterized by different filtration efficiency and performance [7].

The classification divides masks into three FFP (filtering facepiece) safety classes, depending on the degree of protection according to the European standard (EN 149) [8]. The protection classes FFP1, FFP2, and FFP3 provide respiratory protection against various concentrations of contaminants found in the surrounding environment. The FFP1 class has the least protection against biohazards - it allows for the filtration of at least 80% of the particles found in the air which are no larger than 0.6  $\mu\text{m}$ . The FFP2 standard provides protection against solid and liquid dust, smoke and aerosol particles that can have adverse effects on health, especially on the respiratory system. The threshold value for capturing these types of particles from the air is at least 94%, and their size does not exceed 0.6  $\mu\text{m}$ .

The highest degree of respiratory protection against various types of contaminants is provided by the FFP3 class which filters out carcinogenic particles and radioactive substances. It also ensures defence against pathogens, such as viruses, bacteria, and even fungi. It protects against solid and liquid dust that is harmful to the human body and smoke and aerosol particles up to 0.6  $\mu\text{m}$  in size. The filtration value is at least 99% - therefore, it can be considered high and effective protection [9].

Particles found in the surrounding environment have different sizes, shapes and properties, that is why it is so important to develop a mask with a filtering membrane with high performance while maintaining the comfort of use and good breathability [10]. As viruses and bacteria are very small particles that can easily penetrate the layers of the filter, the right material is a key issue. The specifications should focus on the proper chemical composition, porosity, as well as the thickness and density of the fibers arrangement in the material [5].

In order to provide the material with antibacterial and antiviral properties, a well-established method is the use of silver ions. However, from the point of view of clinical microbiology, silver is unfavourable since its ions can sterilize the environment due to the wide spectrum of their activity. Another important factor that also limits the use of nanosilver is the relatively high price [11,12]. Therefore, it is necessary to look for alternative and safer materials with antimicrobial properties.

Current joint solutions are neither economical nor environmentally friendly, which motivates researchers to find an environmentally friendly material that can be used to build the filter membrane in respiratory protective equipment.

The aim of the study was to obtain the biostatic surface on the personal protective face mask. We used betulin, an organic compound easily obtained via extraction with simple alcohol. Large amounts of betulin are found in the outer bark of white birch species (25-30% content). Bark is a readily available raw material as a by-product in paper mills; therefore, betulin can be produced in a low-cost extraction process, even on an industrial scale [13]. Betulin and its easily obtained derivatives show not only antimicrobial and antiviral properties, but also other beneficial biological behaviours, e.g. anticancer, anti-inflammatory, hepatoprotective, and antilithic activity already at very low concentrations, in the absence of toxicity both *in vitro* and *in vivo* [14-16]. The anti-inflammatory effect results from the inhibition of cell migration to the inflammation sites, thus it will not cause dermatitis. The antiviral betulin property results from inhibiting the virus life cycle in the infected cell at an early stage, which prevents its further development and infection induction. Betulin has an interesting structure with two hydroxyl groups (FIG. 1) at C-3 and C-28, and an isopropenyl group at C-19. As a biofunctional monomer of natural origin, it provides a convenient starting material for many chemical modifications, including polymer synthesis.

The use of betulin as a modifier in the material is one of the goals of this study, in which we evaluated the betulin-modified polycarbonate for antibacterial and anti-inflammatory activity.

The test was also carried out on samples of KN95 (FFP2) mask layers. The chemical composition of these samples was characterized by the Fourier transform infrared (FTIR) spectroscopy.

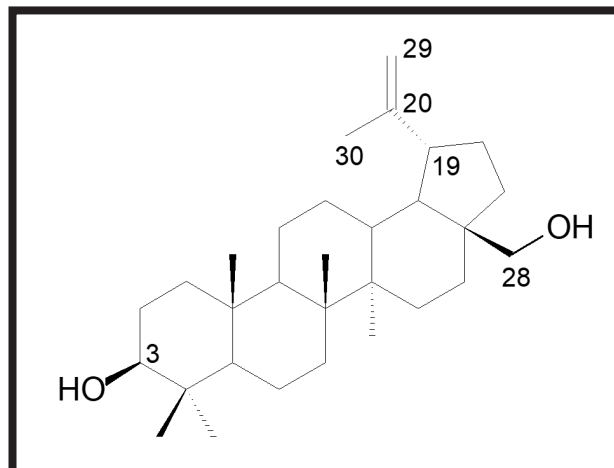


FIG. 1. Chemical formula of betulin.

The geometry of the fibers, their structure, thickness, and arrangement density were assessed using optical and confocal microscopy, as well as computed microtomography. The sample was immersed in a solution of betulin obtained via the Soxhlet extraction, and the results were compared on an optical and confocal microscope to illustrate the differences in the fibers structure.

## Materials and Methods

The facemask subjected to preliminary testing regarding the filtration efficiency was a medical KN95 one- equivalent to the FFP2 class (FIG. 2). The tests provided information on the material properties, chemical composition and morphological structure of the mask layers.

The first research step was the FTIR infrared spectroscopy test used to obtain an IR spectrum based on the amount of absorption or IR transmittance in a sample. For accurate testing, the KN95 mask was separated into layers (FIG. 3), and then each layer was subjected to the FTIR analysis to determine the chemical composition of the mask.

The study was carried out on an FTIR spectrophotometer - IRTracer-100, equipped with an ATR accessory (attenuated total reflectance, ATR). The measurements were carried out at 100 scans per sample. The obtained results were compared with the spectra library.



FIG. 2. KN95 mask.

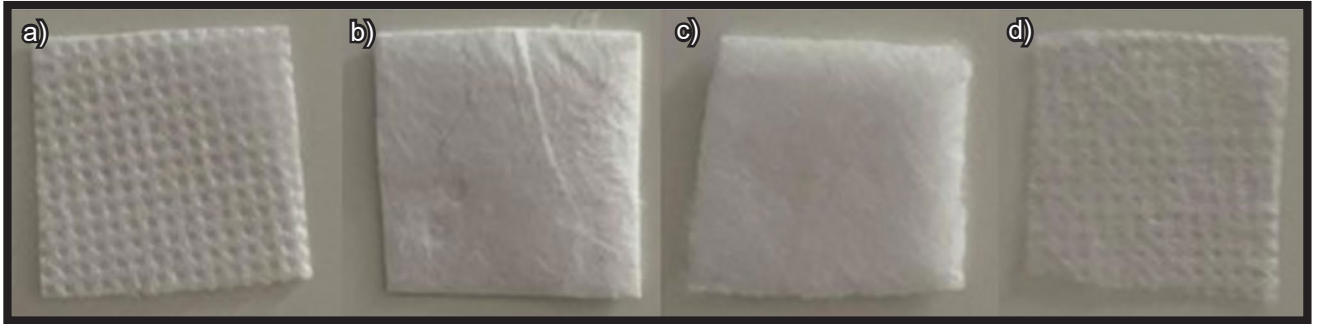


FIG. 3. Layers of the mask filter: a) first layer – outer part, b) first layer – inner part, c) second layer, d) third layer.

To ensure high filtration efficiency against harmful particles, it is important to select the right material with regard to its chemical composition, morphological structure - the diameter, thickness, and density of the fibers arrangement. For this purpose, a test was carried out using an Axiovert 40 MAT optical microscope connected to a PowerShot A640 camera. After placing the sample on the table, the microscope was adjusted to obtain better-quality images. They were taken at different magnifications so as to achieve a detailed analysis of the fibers structure. The surface images were analyzed using ImageJ software.

To obtain the microscopic images, the LEXT OLS4000 scanning confocal microscope was used. The surface images were analyzed using MountainsMap® Premium software.

The next stage of the research was computed microtomography to thoroughly examine the object without interfering with its structure. The technique also made it possible to distinguish areas with different values of the linear X-ray attenuation coefficient, proportional to the density of the tested material. This study was conducted using the GE Phoenix v|tome|x high-resolution x-ray scanner. The parameters of the microtomographic examination were as follows: voxel size ( $\mu\text{m}^3$ ): 10, number of projections: 1000, image resolution (px):  $2024 \times 2024$ , detector type: dxv-250, number of photos to average: 3, number of skips: 0, accelerating voltage (kV): 80, glow current ( $\mu\text{A}$ ): 130, filters: none, scan time (min): 15.

The result was a three-dimensional density map creating a precise 3D model used in further research [17]. Three-dimensional images of the samples were obtained using the MyVgl2 program. Computed microtomography yielded results on the structure of the material and the pore size.

In addition to the structural studies of the mask, we assessed the microbiological activity of the produced polymer modified with betulin. Betulin was obtained by the Soxhlet extraction using ethanol in the Soxhlet apparatus consisting of three parts: a flask, an extractor, and a reflux condenser. The solid - birch bark - was placed in a thimble made of filter paper. The flask contained the solvent - ethanol which boiled after the flask was heated with a heating mantle. The alcohol vapor passed to the reflux condenser. After condensation, the solvent accumulated in the thimble. The liquid with the extracted substance was poured into the flask through a siphon closure where the solvent was then distilled again. The process was long as the sample was extracted repeatedly, while changing the thimble and its contents, until the betulin appropriate concentration was obtained, namely when its colour changed. The higher the concentration, the more brown the substance in the flask. The proper concentration was achieved due to the closed circulation and distillation of the solvent. FIG. 4a shows the colour of the substance in the flask before heating, FIG. 4b during the boiling process, after the liquid with the extracted substance was transferred to the flask, and FIG. 4c depicts the concentration of betulin after several extractions.



FIG. 4. Process of extracting betulin from birch bark: a) before heating, b) during boiling, c) high concentration of botulin.

The modifier obtained according to patent 235673 - can be applied to the material in several ways, e.g. by spraying a betulin solution onto the finished material by ultrasonic atomization (nebulization). The disadvantage of this technique is the high cost of the equipment. Another option is to immerse the material in a betulin solution to endow it with antibacterial and antiviral properties. However, the easiest approach is to mix a betulin modifier into already available polymeric materials, such as polycarbonate, polylactide, polypropylene, polyvinyl chloride, high pressure polyethylene, and polyamide. According to the patent 235673, the method of obtaining a modified thermoplastic polymer with antimicrobial and anti-inflammatory properties is essential. It consists in introducing a thermoplastic base polymer and its modifier into the reactor. The polymer is in the form of granules, aggregates or meal, betulin with a purity of  $\geq 75\%$  is in the form of a purified powder or a suspension in alkoxides, preferably in propylene glycol, in a weight ratio of from 5:1 to 100,000:1, preferably from 20:1 to 100:1. The ingredients are mixed for 10 to 90 min until a uniform coverage of the polymer surface is obtained, and then dried for at least 1 h at a temperature of 10 to 110°C, depending on the technological parameters, i.e. the structure and processing temperature of the polymer used (granulate or aggregate or grits). The resulting mixture of betulin with a suitable polymeric material is a blend. Then, a granulate or a filament of neutral colour is obtained from the blend, following further plastic processing carried out by a selected method.

In our study, the polycarbonate mixed with betulin was obtained as follows: the granulated polycarbonate (1500 g) and the betulin powder (7500 mg) with a purity of  $\geq 98\%$  were introduced into the reactor i.e. a stainless steel mixer with a capacity of 3000 cm<sup>3</sup>, equipped with an electric charge discharge system at 25°C. The ingredients were mixed using a Teflon agitator with scraper blades for 30 min at a speed of 50 rpm, after which the mixture was aerostatically dried at 100°C for 24 h. The dry mixture was extruded using a single-screw, four-zone screw extruder with a screw of 32 l/d using the temperatures of heating zones on the head and the next three zones (265°C, 230°C, 210°C and 160°C, respectively) and an extrusion speed of 60 rpm. The resulting material was collected on a conveyor belt, air-cooled over a three-meter section, and then tested for microbiological activity.

As described above, the studied material was obtained according to the patent 235673 - it was the polycarbonate containing betulin in the range of 0.025-0.5%. This evaluation of its antimicrobial activity was performed in accordance with ISO 22196: 2007 (E) "Plastics - Measurement of antibacterial activity on plastics surfaces". The manufactured material was prepared as a control and test sample in the form of a square with a size and thickness of 50 mm x 50 mm. A reference strain of *Escherichia coli* ATCC 25922 was used as the reference material, with a bacterial inoculum of 0.4 ml and a concentration of  $6 \times 10^5$  bacteria/ml. The incubation of inoculum samples took place at 35°C, with a humidity of no less than 90%, for 24 h. The neutralization of each sample was carried out in accordance with PN ISO 18593: 2005; PN ISO 14562: 2006. After a series of 10-fold dilutions, the samples were incubated in Petri dishes under the conditions described in the standard. For both the test and control samples, the factor N, the number of live bacteria recovered per cm<sup>2</sup> of the sample, was calculated.

In addition to evaluating the antimicrobial activity, the anti-inflammatory activity of the obtained polymeric materials was also tested in accordance with ISO10993-5:2009(E). The study was carried out using normal human dermal fibroblasts (NHDF cell line, CC-2511; Clonetics, San Diego, CA, USA), cultured for 24 h in the FBM medium (Fibroblast Basal Medium; Lonza, Basel, Switzerland), enriched with hFGF-B (Human Fibroblast Growth Factor-basic), insulin and gentamicin (FGMTMSingleQuots™; Lonza, Basel, Switzerland). The anti-inflammatory activity was assessed by analyzing changes in the cell transcriptome, determined by expression microarray, using HG-U133A plates. The validation of the array experiment was performed by the qRT-PCR.

## Results and Discussions

The preliminary studies on the structure and layering of the FFP2 mask filter proved that several factors affected its antibacterial and anti-viral efficiency, e.g. the material of the filter, its porosity, and the fibers properties - density, diameter, and thickness of the arrangement. Such material characteristics was studied by the FTIR analysis, optical microscopy and computed microtomography.

The FTIR spectroscopy was chosen because of its speed and the lack of interference with the sample structure. Thus, we could identify the type of material, the structures of matter at the molecular scale, and the additives that may change its properties. The FTIR analysis consists in producing an optical signal with all IR frequencies encoded in it. The next step is decoding the signal using the Fourier transform and then mapping the spectral information [17]. The result is a graph, a spectrum, which in turn is searched in reference libraries to identify a given sample. In our study, after placing the samples (the KN95 mask layers) in the IRTracer-100 spectrophotometer, the following spectra plots were obtained sequentially.

Based on the obtained reports, the main chemical compound was polypropylene (PP) found in the first layer (outer and inner), as well as in the third layer (FIGs 5, 6, 8). It is a polymer that belongs to the polyolefin group and is used in the production of plastics in both industry and in medicine. It is characterized by high chemical resistance, good air permeability and low water vapor permeability. Therefore, it is suitable for use in masks or other upper respiratory protection devices.

The chemical compound found in the second layer was high-density polyethylene, HDPE (high density PE) (FIG. 7). It is a thermoplastic polymer made from ethylene which has high tensile strength and is chemically unreactive. Both polypropylene (PP) and polyethylene (HDPE) are suitable materials for use in upper respiratory protection devices. On the other hand, for an innovative and more environmentally friendly solution, a better material for filters in masks would be cellulose fibers obtained from an organic compound. Natural fibers are not antibacterial or antiviral. It is modifiers, e.g. silver ions, that can provide such antibacterial and antiviral properties. In addition, silver ions also exhibit antifungal properties [18]. However, it should be noted that the silver release can lead to environmental sterilization as a result of its broad action spectrum. Therefore, silver must not be present in the filter layer in direct contact with the user's face. Moreover, silver ions exhibit many cytotoxic characteristics against human cells [11,19]. Another important factor that inhibits the widespread use of nanosilver is its relatively high cost. For this purpose, we produced a filter membrane with betulin and subjected it to biological activity tests with a polymeric material.

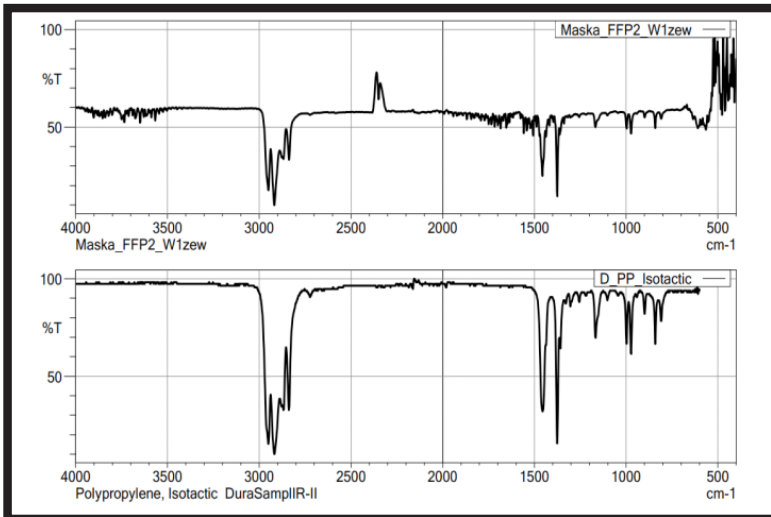


FIG. 5. FTIR analysis plot for the first layer - outer part.

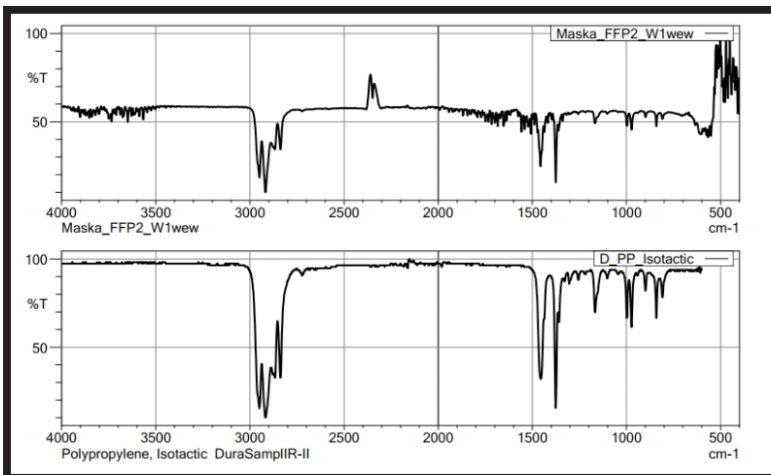


FIG. 6. FTIR analysis plot for the first layer - inner part.

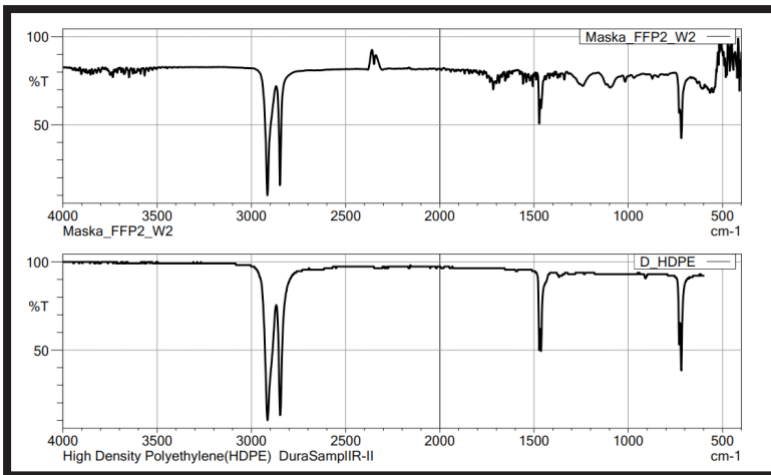


FIG. 7. FTIR analysis plot for the middle layer.

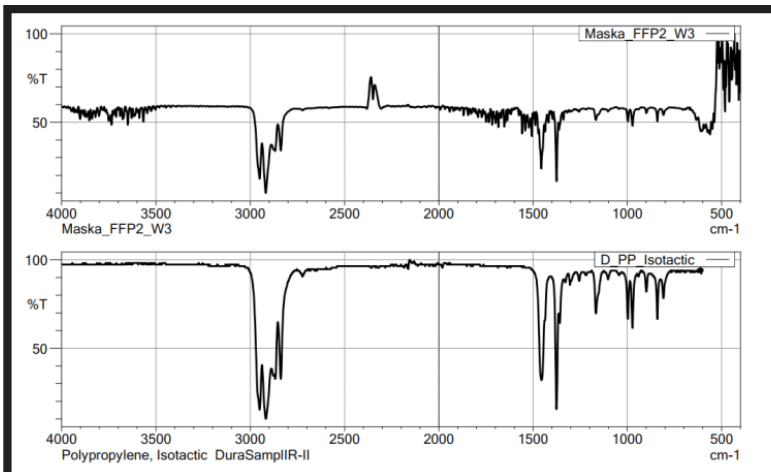


FIG. 8. FTIR analysis plot for the third layer.

Besides betulin, the filter material can also be enriched with electrostatic charges. Filters using electrostatic fields can separate various ionized impurities. After electret treatment, the filter material will receive a positive charge, allowing the filtration efficiency to increase significantly. Biological particles, such as viruses, bacteria and aerosols, are negatively charged and become trapped or blocked by the generated electric field as they are carried by the airflow through the positively charged fibers [20].

Thanks to the optical microscopy images, the geometry (length, thickness) and fibers arrangement of the FFP2 mask was clearly seen before immersing it in the betulin solution (FIGs 9, 12, 15). The LEXT OLS4000 scanning confocal microscope was also used to analyze the mask after the immersion in order to impart antibacterial, antiviral and anti-inflammatory properties (FIGs 10, 11, 13, 14, 16, 17), and to compare the fibers structure.

Using a confocal microscope, changes in the morphology of the mask fibers were observed and compared to the optical microscopy samples that showed smooth fibers. The uneven distribution of betulin particles was clearly observed in the confocal microscope images (FIGs 10, 13, 16). Numerous particles gathered in some areas, while other areas were covered with only a few particles.

The fibers diameter of less than 100 nm defined them as nanofibers, and their thickness was less than 1 denier (unit of linear density of synthetic fibers). The synthetic polypropylene fibers were densely spaced and had characteristic folds, providing a barrier to viruses and bacteria or other airborne contaminants. The shorter the fibers, the more air they are able to hold, and this will allow them to retain more particles and further aid thermal insulation. The appropriate size of the fibers or their arrangement significantly improves effectiveness of filtration, which should be taken into account when choosing the right filter material.

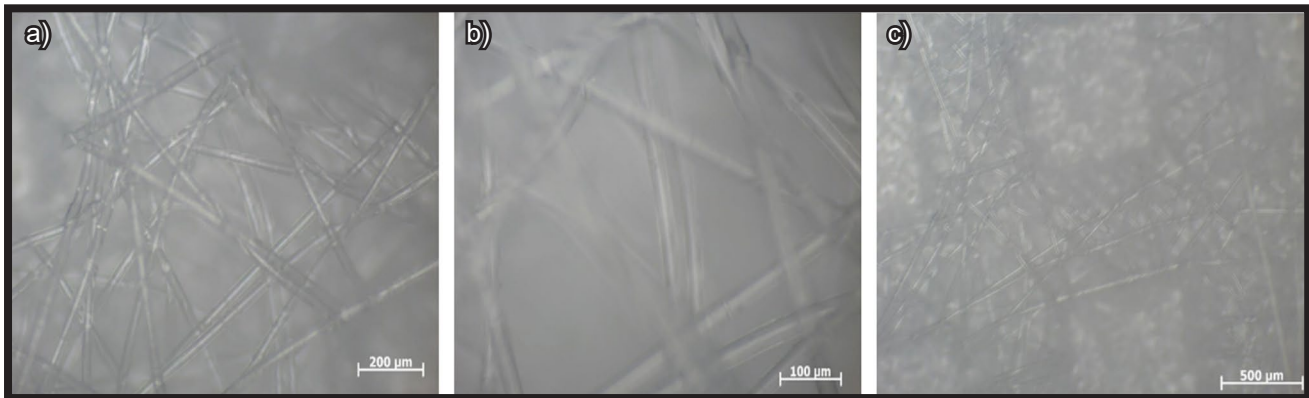


FIG. 9. Optical microscope images of fibers for the first layer (inner and outer).

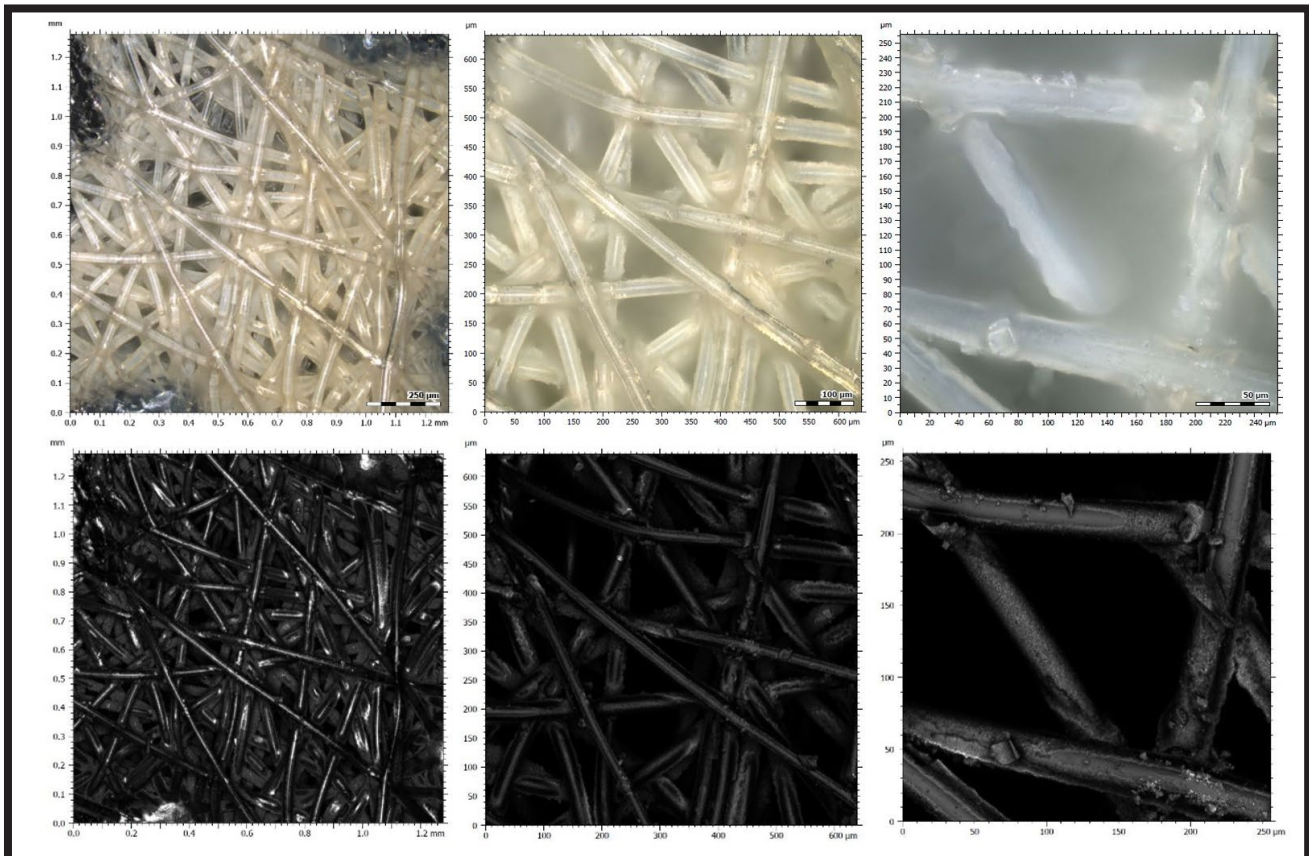


FIG. 10. Confocal microscope images of fibers for the first layer (inner and outer).

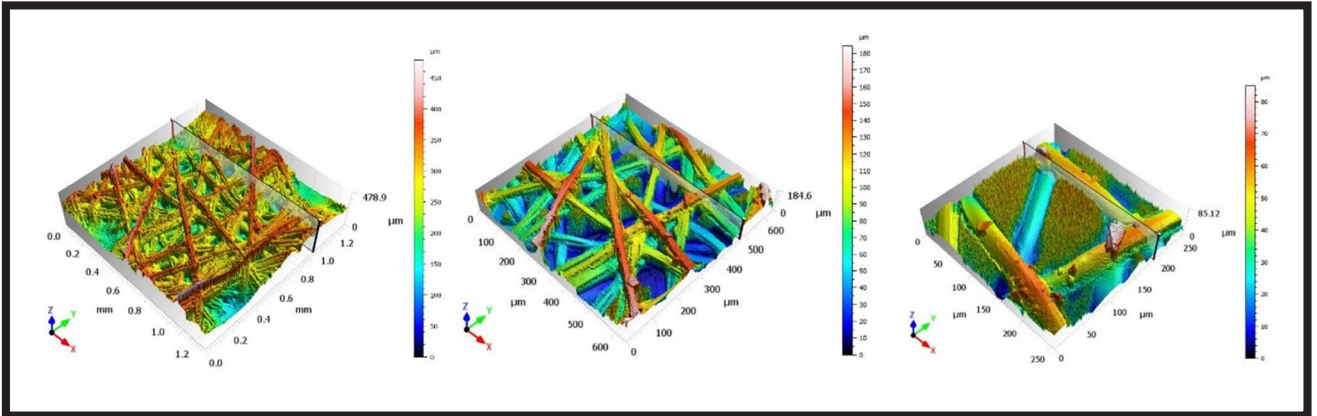


FIG. 11. 3-D view of fibers for the first layer (inner and outer).

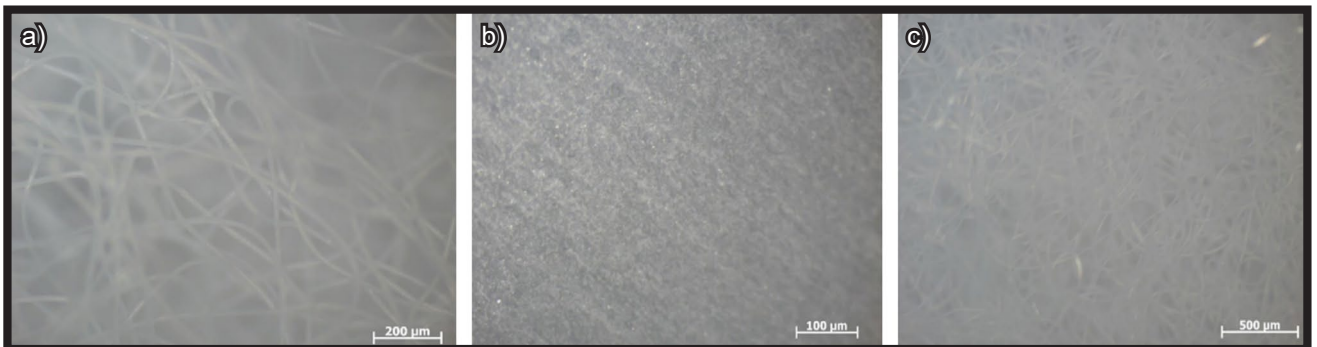


FIG. 12. Optical microscope images of fibers for the second layer.

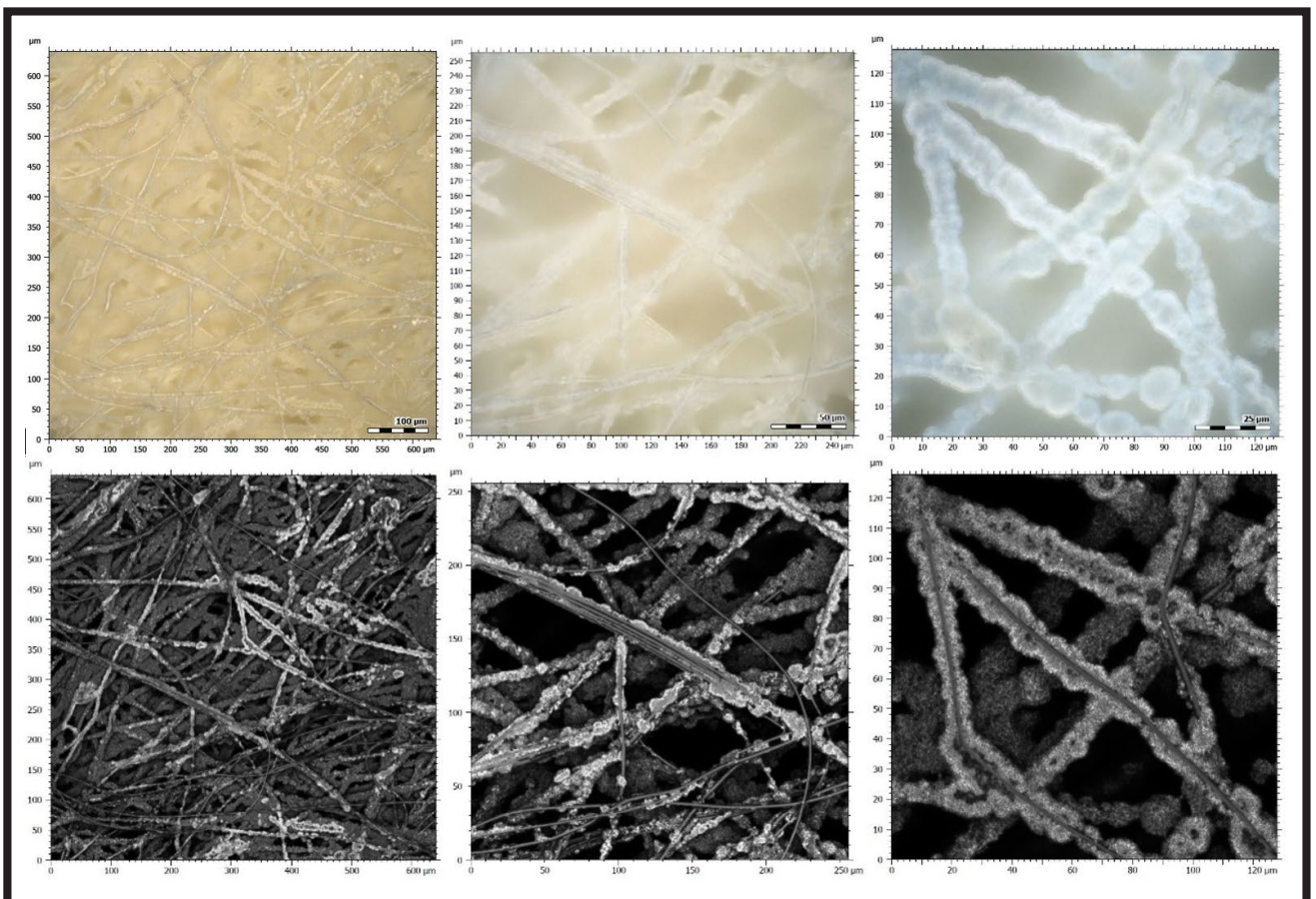


FIG. 13. Confocal microscope images of fibers for the second layer.

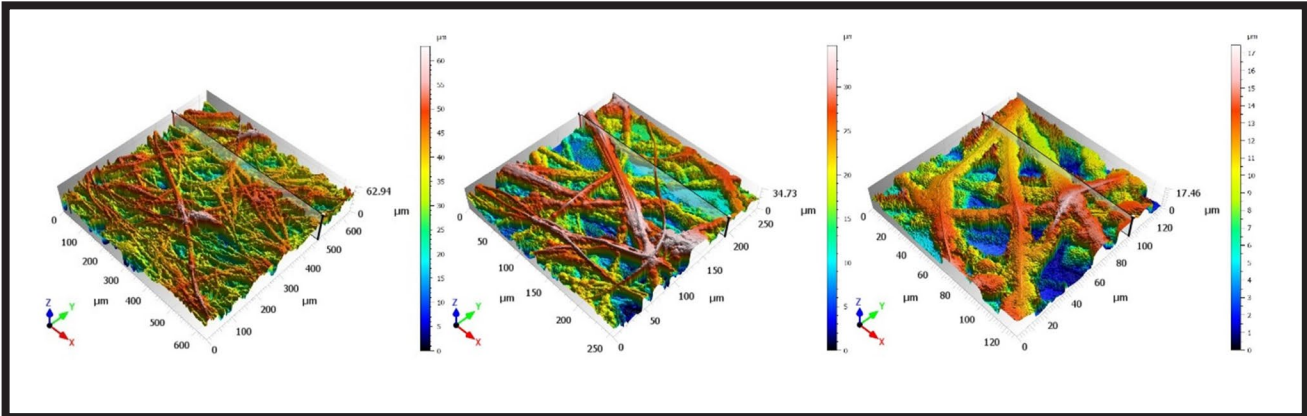


FIG. 14. 3-D view of fibers for the second layer.



FIG. 15. Optical microscope images of fibers for the third layer.

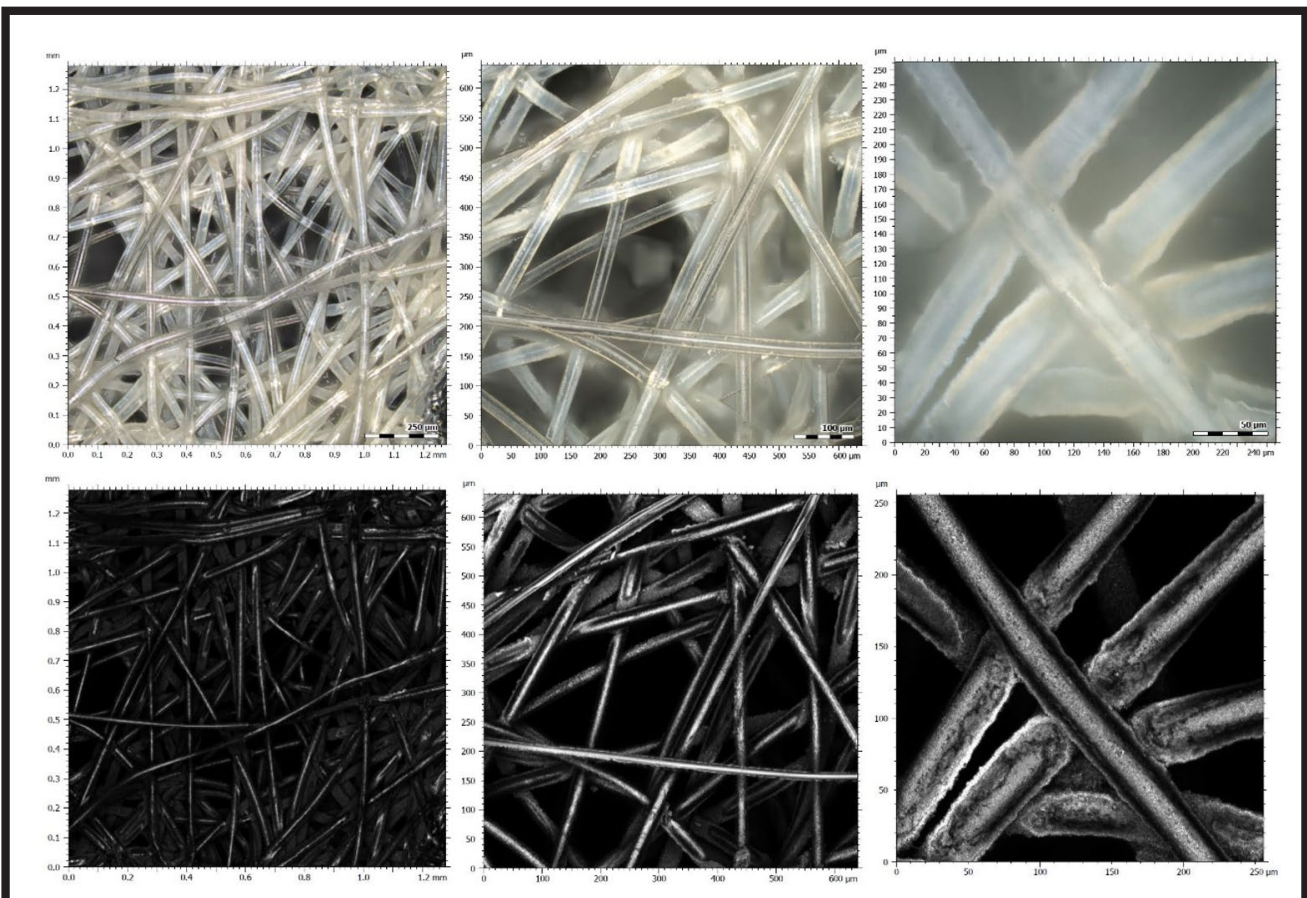


FIG. 16. Confocal microscope images of fibers for the third layer.

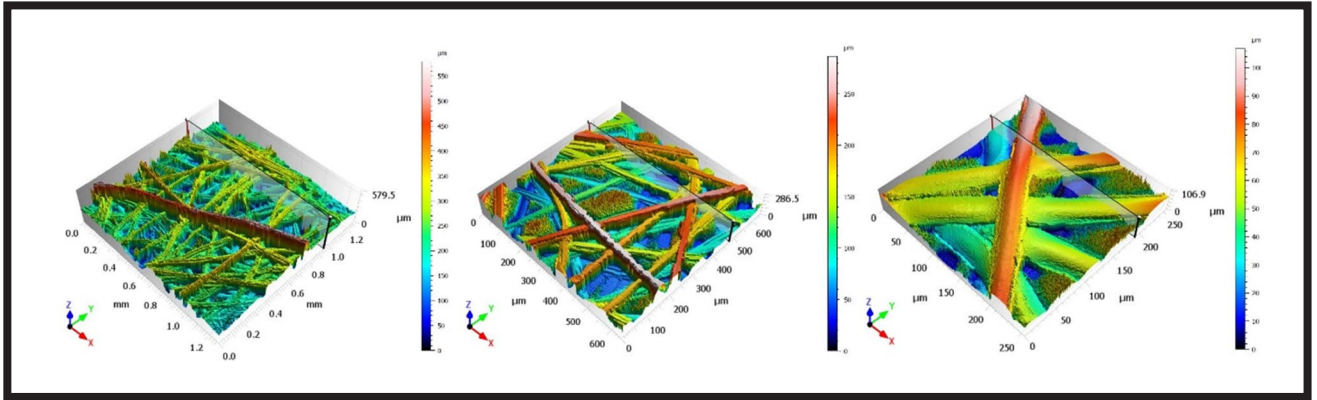


FIG. 17. 3-D view of fibers for the third layer.

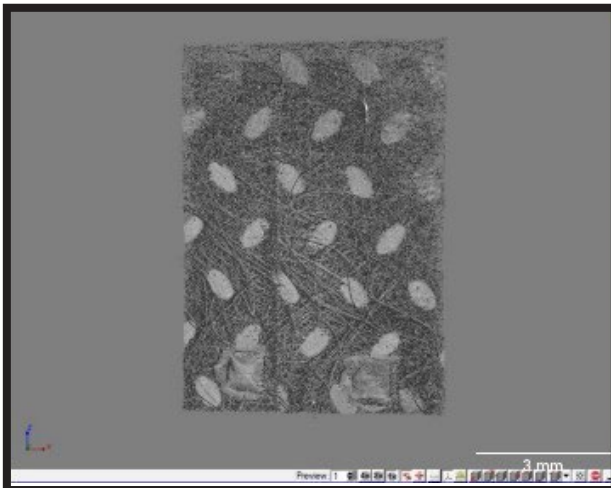


FIG. 18. Image of FFP2 mask from computed microtomography with visible pores.

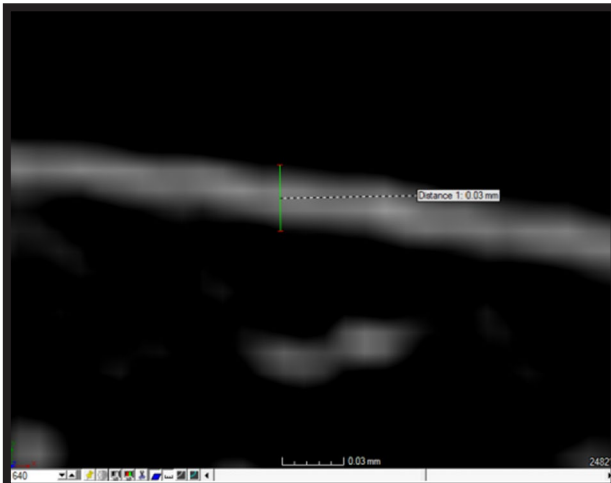


FIG. 19. Fiber thickness.

The difference in the fibers arrangement and density was studied via a non-invasive method of computed microtomography. The obtained images revealed how specific layers were separated. Each layer had a different fiber density. The most dense layer was the middle one, due to HDPE which is a high-density thermoplastic polymer. Pores were seen (FIG. 18), which is very important in terms of the protective filter. The appropriate sized pores retain and “trap” very small particles so that they do not reach the mask user’s face. Microtomography revealed the density of the fibers arrangement (FIG. 18) and the fibers thickness, which was about 0.03 mm (FIG. 19).

The tests led to the evaluation of biological activity. Based on the results, the R antimicrobial activity of the 0.025-0.5% betulin polymer plates was found to be in the range ( $R = 1.45 - 2.0$ ) compared to the starting material without betulin. The average antibacterial activity (R) for the tested material, in this case, was 1.85, according to the following values - *Escherichia coli*:  $U_0 = 4.21$ ,  $U_t = 4.91$  and  $A_t = 3.46$ :

$$R = (U_t - U_0) - (A_t - U_0) = U_t - A_t$$

where:

$U_0$  - mean of the decimal logarithm of the number of live bacteria, number of cells/cm<sup>2</sup>, recovered from the untreated samples after culture,

$U_t$  - mean of the decimal logarithm of the number of viable bacteria, number of cells/cm<sup>2</sup>, recovered from the untreated samples after 24 h,

$A_t$  - mean of the decimal logarithm of the number of live bacteria, number of cells/cm<sup>2</sup>, recovered from the samples treated after 24 h.

The polymers modified with betulin showed significant antimicrobial and anti-inflammatory activity. The observed changes in the expression profile of genes involved in inflammatory processes indicated the anti-inflammatory effect of the obtained polymeric materials, as compared to the starting material without betulin. Due to the achieved properties, the betulin-enhanced materials can be advantageously used in medicine and biotechnology.

## Conclusions

In order for the filter to effectively protect the respiratory tract, it is necessary to develop appropriate materials that will contribute to the antibacterial and antiviral functions. Materials with this type of properties are becoming more and more popular on the medical market, especially during the current pandemic, where the demand for antimicrobial activity has increased. That is why we decided to test the innovative solution - a filtering membrane of organic compound - to protect the upper respiratory tract from viral and bacterial infections, compliant with the FFP2 standard.

In our study, betulin was isolated from the outer bark of the birch via the Soxhlet extraction. The evaluation of the microbiological and anti-inflammatory activity of the betulin polymeric material proved it highly useful. The FTIR analysis showed that the main compounds in the FFP2 mask were polymers - polypropylene and high-density polyurethane (HDPE), the surface of which was easily modified with betulin, both by applying it as an aerosol and by immersion via the layer-by-layer method. The described materials are also suitable for modification at the synthesis stage, i.e. in bulk. In the optical and confocal microscope images, the morphological changes of the mask fibers were observed, as compared to the optical microscopy samples showing smooth fibers. The betulin particles were clearly visible in the confocal microscope images.

Despite the uneven betulin distribution, the bacteriostatic properties were confirmed and maintained at a satisfactory level. In the future, the immersion method should be replaced with the spray method, due to the formation of low-energy agglomerates. Many particles gathered in some areas, while other areas were covered with only a few particles. The presence of pores and the structure of the fibers were also examined using a non-invasive test - computer microtomography.

In summary, our study proved the applicability of the proposed solution.

## Acknowledgements

*The work was carried out as part of the statutory research of the Institute of Biomedical Engineering, University of Silesia.*

### ORCID iD

N. Brzezińska: <https://orcid.org/0000-0002-8648-2498>  
 M. Pyza: <https://orcid.org/0000-0002-7904-9303>  
 A. Kłeczek: <https://orcid.org/0000-0001-6066-3349>  
 K. Kulińska: <https://orcid.org/0000-0002-6676-1502>  
 J. Gabor: <https://orcid.org/0000-0003-4850-1608>  
 Ż. Garczyk-Mundała: <https://orcid.org/0000-0003-4345-5315>  
 A. Swinarew: <https://orcid.org/0000-0001-6116-9510>

## References

- [1] Regli A., Sommerfield A., Ungern-Sternberg B.S.: The role of fit testing N95/FFP2/FFP3 masks: a narrative review. *Anaesthesia* 76(1) (2021) 91-100, doi: 10.1111/anae.15261
- [2] Cascella M., Rajnik M., Aleem A., et al.: Features, Evaluation, and Treatment of Coronavirus (COVID-19). StatPearls Publishing (2021)
- [3] Nowakowska E., Michalak S.S.: Covid-19 – Choroba wywołana zakażeniem wirusem SARS-Cov-2 globalnym zagrożeniem dla zdrowia publicznego. *Postępy Mikrobiologii – Advancements of Microbiology* 59(3) (2020) 227-236, doi: 10.21307/pm-2020.59.3.16
- [4] Pawlik L., Śpiołek E., Fichna J., Tarasiuk A.: Charakterystyka wirusa SARS-CoV-2 i potencjalne farmakologiczne sposoby leczenia. *Postępy Biochemii: Zakład Biochemii, Katedra Chemii i Biochemii Medycznej, Uniwersytet Medyczny w Łodzi* 66(2) (2020), doi: 10.18388/pb.2020\_321
- [5] Fenner F.: Epidemiology and Evolution. In: Baron S., editor. *Medical Microbiology*. 4th edition. Galveston (TX): University of Texas Medical Branch at Galveston (1996)
- [6] Tcharkhtchi A., Abbasnezhad N., Zarbini Seydan M. et al.: An overview of filtration efficiency through the masks: Mechanisms of the aerosols penetration. *Bioactive Materials* 6(1) (2021) 106-122, doi: 10.1016/j.bioactmat.2020.08.002
- [7] Ippolito M., Vitale F., Accurso G. et al.: Medical masks and Respirators for the Protection of Healthcare Workers from SARS-CoV-2 and other viruses. *Pulmonology* 26(4) (2020) 204-212, doi: 10.1016/j.pulmoe.2020.04.009
- [8] Smreka J., Ruetzler K. et al.: Role of Mask/Respirator Protection Against SARS-CoV-2. *Anesthesia and analgesia* 131(1) (2020) e33-e34, doi:10.1213/ANE.0000000000004873
- [9] Zhou J., Hu Z., Zabihi F. et al.: Progress and Perspective of Antiviral Protective Material. *Advanced Fiber Materials* 2 (2020) 123-139, doi: 10.1007/s42765-020-00047-7
- [10] Li K.K.W., Jousen A.M., Kwan J.K.C. et al.: FFP3, FFP2, N95, surgical masks and respirators: what should we be wearing for ophthalmic surgery in the COVID-19 pandemic? *Graefes Arch Clin Exp Ophthalmol.* 258(8) (2020) 1587-1589, doi: 10.1007/s00417-020-04751-3
- [11] Palaniappan P., Sathishkumar G., Sankar R.: Fabrication of nano-silver particles using *Cymodocea serrulata* and its cytotoxicity effect against human lung cancer A549 cells line, *Spectrochimica Acta Part A: Molecular and Biomolecular Spectroscopy* 138 (2015) 885-890 doi: <https://doi.org/10.1016/j.saa.2014.10.072>.
- [12] Massarsky A., Abraham R., Nguyen K.C. et al.: Nanosilver cytotoxicity in rainbow trout (*Oncorhynchus mykiss*) erythrocytes and hepatocytes. *Comp. Biochem. Physiol. Pt. C.* 159 (2014) 10-21.
- [13] Swinarew A., Boryczka S., Mazurek U. et al.: Modyfikowany polimer termoplastyczny o właściwościach przeciwbakteryjnych i przeciwzapalnych oraz sposób jego otrzymywania, *Polska*, 422092 B1, 03.07.2017
- [14] Tolstikova T.G., Sorokina I.V., Tolstikov G.A. et al.: Biological activity and pharmacological prospects of lupane terpenoids: II. Semisynthetic lupane derivatives. *Chem.* 32 (2006) 37-49.
- [15] Huang T., Li D., Elc M., Water repellency improvement of cellulosic textile fibers by betulin and a betulin-based copolymer. *Cellulose* 25, 2115-2128 (2018), doi: <https://doi.org/10.1007/s10570-018-1695-5>.
- [16] Alakurti S., Mäkelä T., Koskimies S., et al.: Pharmacological properties of the ubiquitous natural product betulin. *Eur J Pharm Sci.* 29(1) (2006) 1-13.
- [17] Kowalczyk D., Pitucha M.: Application of FTIR Method for the Assessment of Immobilization of Active Substances in the Matrix of Biomedical Materials. *Materials (Basel)* 12(18) (2019) 2972, doi: 10.3390/ma12182972;
- [18] Pulit J., Banach M., Kowalski Z.: Właściwości nanocząsteczek miedzi, platyny, srebra, złota i palladu. *Czasopismo techniczne, Wydawnictwo Politechniki Krakowskiej* 10 (2011)
- [19] Massarsky A., Abraham R., Nguyen K.C. et al.: Nanosilver cytotoxicity in rainbow trout (*Oncorhynchus mykiss*) erythrocytes and hepatocytes. *Comp. Biochem. Physiol. Pt. C.* 159 (2014) 10-21.
- [20] Brown R.C.: Effect of electric charge in filter materials. *Filtration & Separation* 26(1) (1989) 46-51, doi: 10.1016/S0015-1882(89)80057-6.

# COMPOSITE SCAFFOLDS ENRICHED WITH CALCIUM CARBONATE MICROPARTICLES LOADED WITH EPIGALLOCATECHIN GALLATE FOR BONE TISSUE REGENERATION

KRZYSZTOF PIETRYGA<sup>1,2\*</sup> , ANCA-ALEXANDRA PANAIT<sup>3</sup> , ELŹBIETA PAMUŁA<sup>1</sup> 

<sup>1</sup> AGH UNIVERSITY OF SCIENCE AND TECHNOLOGY, FACULTY OF MATERIALS SCIENCE AND CERAMICS, DEPARTMENT OF BIOMATERIALS AND COMPOSITES, AL. MICKIEWICZA 30, 30-059 KRAKÓW, POLAND

<sup>2</sup> SILESIAN PARK OF MEDICAL TECHNOLOGY KARDIO-MED SILESIA, UL. MARIII SKŁODOWSKIEJ-CURIE 10C, 41-800 ZABRZE, POLAND

<sup>3</sup> UNIVERSITY POLITECHNICA OF BUCHAREST, FACULTY OF MEDICAL ENGINEERING, SPLAIUL INDEPENDENTEI 313, 060042 BUCHAREST, ROMANIA

\*E-MAIL: PIETRYGA@AGH.EDU.PL

## Abstract

*There is a need to develop advanced multifunctional scaffolds for the treatment of bone tissue lesions, which apart from providing support for infiltrating cells could assure the delivery of drugs or biologically active molecules enhancing bone formation. We developed composite scaffolds for bone tissue engineering based on gellan gum (GG) and gelatin (Gel) hydrogel enriched with epigallocatechin gallate (EGCG) loaded CaCO<sub>3</sub> microparticles and subjected to enzymatic mineralization with calcium phosphate (CaP). The method of manufacturing CaCO<sub>3</sub> microparticles was optimized. The EGCG-loaded microparticles were smaller than those unloaded, and the release of EGCG was prolonged for up to 14 days, as shown by the Folin-Ciocalteu test. The particles reduced the viability of the MG-63 cells as compared to the control. However, when they were loaded with EGCG, their cytotoxicity was reduced. The particles were suspended in a GG/Gel hydrogel containing alkaline phosphatase (ALP), soaked in calcium glycerophosphate (CaGP) solution to create CaP deposits, and submitted to freeze-drying, in order to produce a porous scaffold. The microstructure of the scaffolds was characterized by optical and scanning electron microscopy and showed that the size of the pores corresponds to that of the spongy bone. In vitro tests with MG-63 cells confirmed that mineralized scaffolds support cell adhesion and growth to a higher extent than nonmineralized ones.*

**Keywords:** gellan gum, gelatin, hydrogel, calcium carbonate microparticles, enzymatic mineralization, epigallocatechin gallate (EGCG)

[Engineering of Biomaterials 166 (2022) 12-21]

doi:10.34821/eng.biomat.166.2022.12-21

Submitted: 2022-11-21, Accepted: 2023-02-10, Published: 2023-02-28



Copyright © 2022 by the authors. Some rights reserved. Except otherwise noted, this work is licensed under <https://creativecommons.org/licenses/by/4.0>

## Introduction

Although bone tissue as such displays remarkable regenerative properties, bone tissue defects require special attention, especially for lesions with large size [1]. Today, tissue engineering approaches that apply scaffolds able to support adhesion, viability, and proliferation of cells to improve tissue healing are widely studied [2]. In this context, composite scaffolds, designed to mimic phase composition, structure, and properties of bone extracellular matrix, seem to be particularly promising [3]. Among the different approaches to producing such biomimetic scaffolds, one is especially interesting, which is based on the enzymatic mineralization of hydrogels [4,5]. Moreover, additional functionalities to stimulate bone tissue defects treatment, such as modifying scaffolds with drug delivery carriers, are of particular importance [6].

Gellan gum (GG) is an anionic calcium-binding polysaccharide produced by bacteria (*Sphingomonas elodea*) during aerobic fermentation; it is widely used in the food industry as a thickener and stabilizer [7]. More recently, GG submitted to mineralization has been applied as a bone tissue engineering scaffold [5,8]. In brief, mineralization of GG can be achieved by the addition of an enzyme, alkaline phosphatase (ALP), and incubation in a calcium glycerophosphate (CaGP) solution. The ALP uses the CaGP as the substrate, cleaving the phosphate, resulting in the precipitation of insoluble phosphate salts (CaP) inside the hydrogel.

Calcium carbonate microparticles due to their high surface-to-volume ratio, high specific surface area, easy synthesis, and ability to exist in a variety of morphologies and polymorphs are considered for medical applications, especially as drug delivery systems and as a mineral phase in polymer/ceramic composites [9,10]. They have been found to possess excellent biocompatibility with bone tissue and negligible cytotoxicity toward mammalian cells [9].

Epigallocatechin gallate (EGCG), belonging to a group of catechins, has been shown to have a pharmacological effect on bone metabolism, induce osteogenic differentiation, and inhibit osteoclastogenesis [11,12]. Despite the positive properties, its delivery to the bone tissue lesion is challenging.

The aim of this study was to develop innovative composite scaffolds for bone tissue engineering based on GG and Gel enriched with CaCO<sub>3</sub> microparticles loaded with EGCG and submitted to enzymatic mineralization and to test their microstructure, properties, and cytocompatibility with osteoblast-like MG-63 cells.

## Materials and Methods

### Materials and chemicals

All materials, including GG (G1910, "Low-Acyl", 200-300 kD), gelatin (G2500, from porcine skin), calcium glycerophosphate (CaGP, 50043), alkaline phosphatase (ALP, P7640), EGCG (E4143, >95%), and Folin-Ciocalteu reagents, were acquired from Sigma-Aldrich, unless otherwise stated. Calcium chlorate and sodium carbonate were purchased from Avantor Performance Materials Poland.

### Particles preparation

Calcium carbonate particles were prepared by the precipitation method. The 0.33M Na<sub>2</sub>CO<sub>3</sub> solution and the 0.33M CaCl<sub>2</sub> solution were mixed and immediately stirred with a magnetic stirrer or ultrasound. For the stirring method, two intensives were used: magnetic stirrer with 120 rpm (Ms120) and 1000 rpm (Ms1000) or sonicated (VCX 130 with 6 mm probe, Sonics & Materials, USA) at 20% and 60% amplitude (So20 and So60, respectively). The particles were centrifuged and washed 2 times with ddH<sub>2</sub>O.

### Hydrogel preparation

Hydrogels were prepared from GG and gelatin and cross-linked by  $\text{CaCl}_2$  and containing ALP for the mineralization process. Smaller particles obtained by sonication were also added to the hydrogels. The procedure for obtaining hydrogels was as follows: GG, Gel, and  $\text{CaCl}_2$  solutions were prepared and heated to  $90^\circ\text{C}$  for 30 min. The temperature was lowered to  $70^\circ\text{C}$ . The ALP solution in water and the suspension of particles in water were prepared. The gelatin solution was mixed with  $\text{CaCl}_2$  and then with ALP solution (in  $\text{H}_2\text{O}$ ), the suspension of particles, and finally GG. The solution was poured between two Petri dishes separated with 1 mm spacers. The final concentration of the ingredients in the hydrogel was: 0.5% w/v GG, 10% w/v gelatin, 0.03%  $\text{CaCl}_2$ , 1 mg/ml ALP, and 0.15% particles with EGCG. The hydrogel was cooled to room temperature until gelation and then stored at  $4^\circ\text{C}$  for 30 min for further hardening. Cylindrical samples of 8 mm diameter and 1 mm height were cut.

### Hydrogel mineralization

Right after the preparation, cylindrical 8 mm samples of the resulting hydrogel were incubated in 0.1M CaGP for one day. After mineralization, the samples were washed until the next day in  $\text{ddH}_2\text{O}$  to remove by-products.

### Particle size distribution

The size of the microparticles was determined by light microscopy (Axiovert 40, Zeiss). Particles were prepared by dropping the suspension of diluted particles into a glass slide and collecting microscopic images in transmitted light. For each particle type, 500 particles were measured in ImageJ and the collected data was presented as histograms.

### EGCG release test

The concentration of EGCG released from the particles was measured using the Folin-Ciocalteu method. The particles (10 mg) were incubated in 1 ml of PBS in a 24-well plate for 14 days. The supernatant was collected after 1 h and 1, 3, 7, and 14 days of incubation. For each measurement, 100  $\mu\text{l}$  extract was mixed with 10  $\mu\text{l}$  20%  $\text{Na}_2\text{CO}_3$  and 10  $\mu\text{l}$  Folin-Ciocalteu reagent. The mixture was incubated for 30 min and then the absorbance was measured at 760 nm (FLUOstar Omega Microplate Reader, BMG LABTECH). The EGCG was calculated from the calibration curve in the range of 1-50  $\mu\text{M}$  EGCG. For each interval, percentage release was calculated based on the initial measurement of the EGCG concentration in particles after complete dissolution in 0.1 M HCl.

### Microstructure

The microstructure of the particles and freeze-dried hydrogels was analyzed by SEM microscopy (Hitachi S3400N, Japan). The material was mounted using carbon tape on holders. Observations were carried out under a low vacuum (70 Pa) without carbon sputtering. Before measurements, the hydrogels were frozen at  $-80^\circ\text{C}$  and freeze-dried for 1 day. Additional microphotography of the freeze-dried hydrogel scaffold was recorded on AxioZoom (Zeiss, Germany) light microscopy. The images were taken in transmitted angular light.

### Biological properties

Cytotoxicity and viability tests on osteoblast-like MG-63 cells (European Collection of Cell Cultures, Salisbury, UK) were performed in contact with particles. First cells were cultured in 100  $\mu\text{l}$  Dulbecco's Modified Eagle Medium (DMEM PAA, Austria) supplemented with 2% fetal bovine serum (FBS), 1% penicillin/streptomycin, 2 mM L-glutamine, 1% non-essential amino acids in a 96-well plate (Nunclon).

The particles (So20 and So60) were first incubated with 70% EtOH for 10 min for sterilization. Subsequently, the particles were washed 2 times with phosphate buffered saline (PBS) and resuspended in cell culture medium at concentrations of 10, 5 and 2.5 mg/ml. After the MG-63 cells confluence was reached, 10% of the suspension of particles was added to the cell culture. Cell culture with particles concentration of 1 mg/ml, 0.5 mg/ml, and 0.25 mg/ml was continued for 2 days.

Cytotoxicity was measured by the lactate dehydrogenase (LDH) test (Sigma-Aldrich) on medium collected from cell culture. 50  $\mu\text{l}$  of medium was mixed with 50  $\mu\text{l}$  reagent and the reaction was carried out for 15 min and then stopped by adding 50  $\mu\text{l}$  of 0.1 M HCl. The absorbance was measured by the Tecan Sparck microplate reader at 492 nm.

Viability was tested by resazurin reduction (Alamar Blue, R7017, Sigma-Aldrich). Cell media from the cultures were removed and replaced by the same volume of media containing 0.05 mg/ml of resazurin. The culture was then continued for the next 4 h until a visible change of colour was observed. The fluorescence of the analyzed culture medium was measured for emission within 585 nm with extinction at 570 nm. Collected values were normalized to 100% viability of the control culture (cells without particles).

Viability, cytotoxicity, and morphology were additionally visualized by live-dead staining. The medium was removed from each well and replaced with a staining solution – 0.1% calcein AM (17783, Sigma Aldrich) and 0.1% propidium iodide (537060, Sigma-Aldrich) in PBS. After 20 min of incubation, fluorescence images were taken using AxioVert 40 with HXP 120 C metal halide illuminator (Zeiss, Germany).

## Results and Discussion

### Calcium carbonate microparticles

Calcium carbonate microparticles obtained by the precipitation method could be prepared relatively easily by mixing a  $\text{Na}_2\text{CO}_3$  solution with a 0.33M  $\text{CaCl}_2$  solution [9]. Particle precipitation is spontaneous, but particle size depends on the intensity of mixing (shear rate) (FIG. 1).

In our work, we tested two methods of mixing: magnetic stirrer and sonication. Magnetic stirrer at low speed (120 rpm) led to larger particles (median 7.5  $\mu\text{m}$ ) whereas fast stirring (1000 rpm) led to much smaller particles (median 3.5  $\mu\text{m}$ ) (FIG. 2). Similar particles as the latter (median 4  $\mu\text{m}$ ) could be obtained by ultrasound set to 20% amplitude. Much smaller particles (median 1.5  $\mu\text{m}$ ) were obtained using 60% amplitude ultrasound. For all conditions, except Ms120, the particles obtained had similar sizes and a narrow size distribution. The varied size of the particles that correlate with the increase in shear rate was an expected phenomenon. This correlation is consistent with the findings of the literature [10].

All produced particles tended to agglomerate, and this was especially visible for the smaller So60 particles (FIG. 1D). The shape of the particles was diverse. Some of the particles had irregular shapes, some had cuboid shapes, and some were rounded. Calcium carbonate particles which have a form of thermodynamically unstable vaterite undergo phase transition into stable calcite [9,10]. It is specifically visible in our SEM images: So20 and So60 particles were subjected to air drying and during that time their phase transition occurred (FIG. 1C, D). Only a small portion of the So20 particles remained rounded (i.e., vaterite), and in the case of So60, all the particles had a cuboid shape (i.e., calcite).

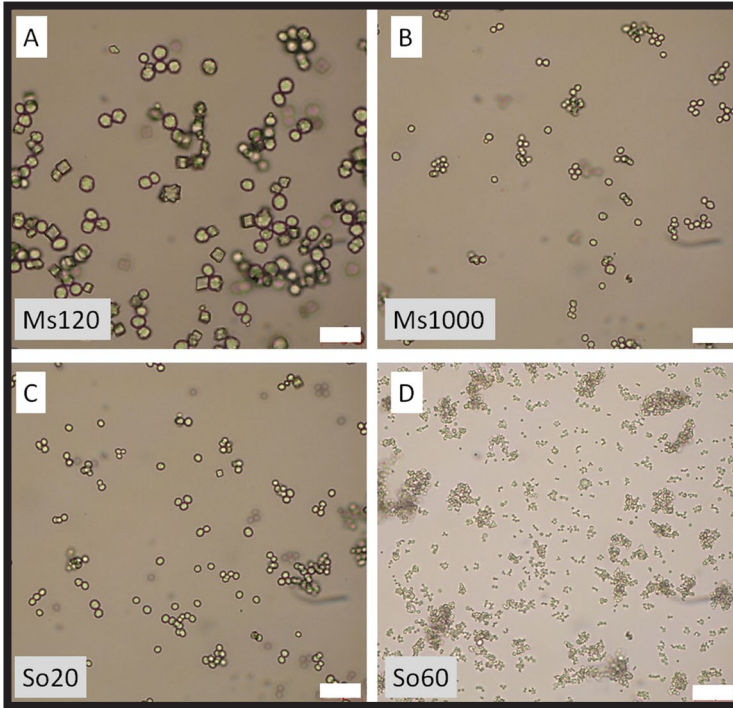


FIG. 1. Optical microscopy images of the unloaded calcium carbonate particles produced at different conditions: slow magnetic stirring (120 rpm, Ms120) (A); fast magnetic stirring (1000 rpm, Ms1000) (B); 20% amplitude sonication (So20) (C); 60% amplitude sonication (So60) (D). Scale bar = 20  $\mu\text{m}$ .

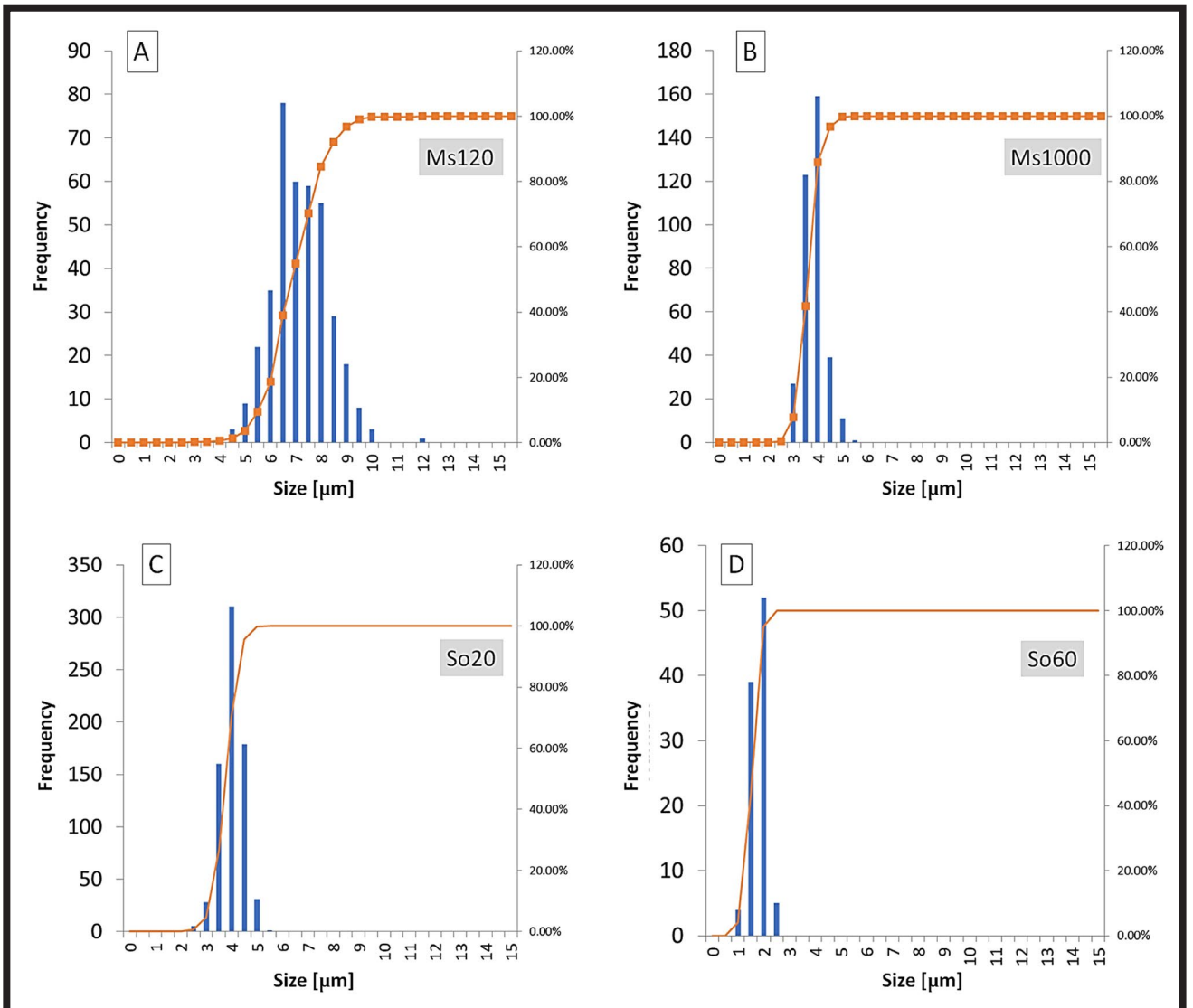
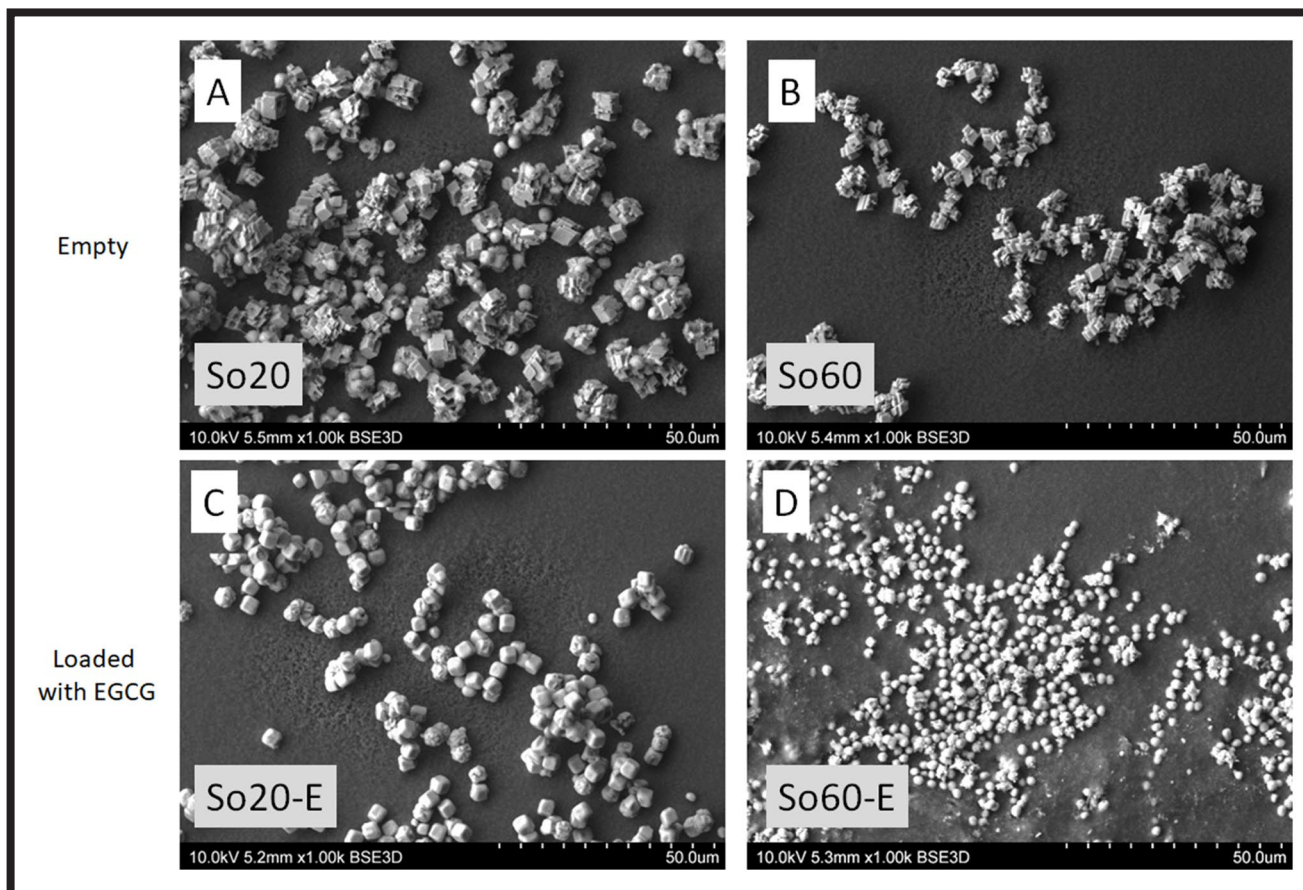


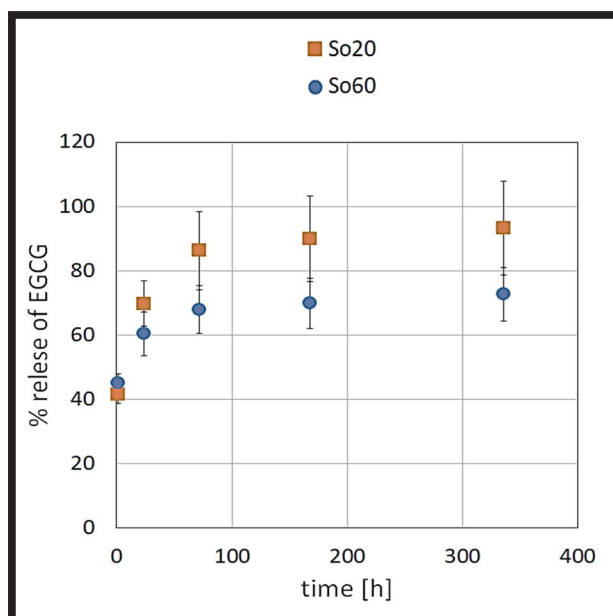
FIG. 2. Histograms of the empty calcium carbonate particles. Slow magnetic stirring particles (120 rpm, Ms120) (A); fast magnetic stirring particles (1000 rpm, Ms1000) (B); 20% amplitude sonicated particles (So20) (C); 60% amplitude sonicated particles (So60) (D).



**FIG. 3. SEM images of calcium carbonate particles: empty 20% amplitude sonicated (So20) (A), empty 60% amplitude sonicated (So60) (B), EGCG-loaded 20% amplitude sonicated (So20-E) (C), and EGCG-loaded 60% amplitude sonicated particles (So60-E) (D). Scale bar = 50  $\mu$ m.**

In the presence of EGCG phase transition was inhibited for So20, as well as for much smaller So60 (FIG. 3). Most of the particles remained rounded and only a small portion of the particles had a cuboid shape. This effect can be explained by the fact that the organic compound EGCG is adsorbing on a  $\text{Ca}_2\text{CO}_3$  surface, therefore stabilizing the structure, size, and shape and preventing its phase transition into calcite.

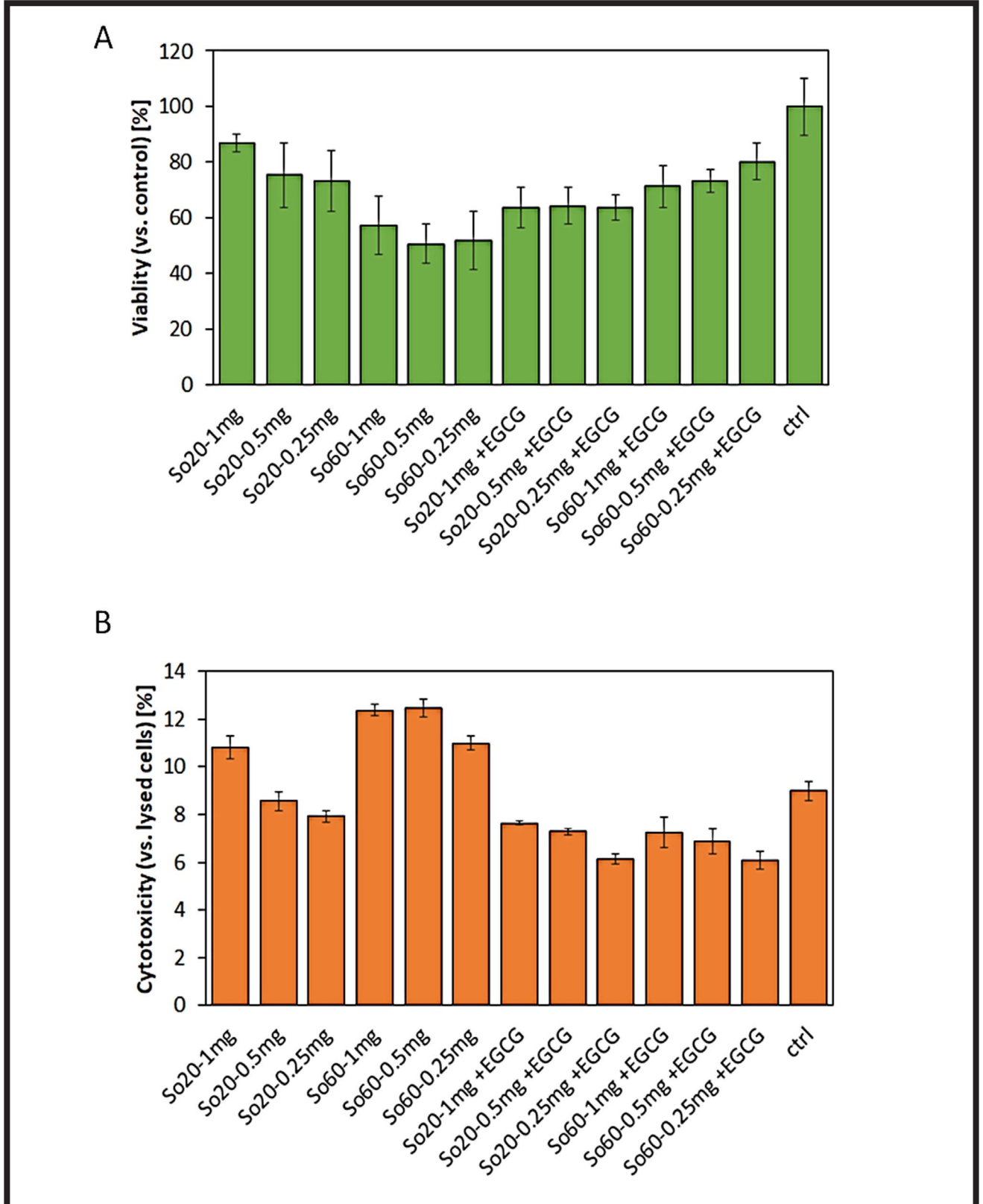
As shown by the Folin-Ciocalteu method, the EGCG content in So20 and So60 was 1.1% and 1.3%, respectively. EGCG release studies showed that between 60% and 70% of this component was released during the first 24 h of incubation, however, a significant amount was still released after 14 days (FIG. 4). For So20 almost 95% EGCG was released during the experiment time, but for So60 the level of 75% was only reached. The reason might be the lower accessibility of smaller particles to external incubation fluid, due to their higher tendency for agglomeration resulting from the higher surface area and thus higher surface free energy. The mechanism of EGCG encapsulation and release from these particles is not clear. We can speculate that EGCG can be physically entrapped inside precipitated particles or adsorbed on the surface of small calcium carbonate crystallites because of their large surface area and thus high surface free energy. The release mechanism can be related to phase changes in calcium carbonate from hexagonal vaterite to rhombohedral calcite (smaller to bigger crystals) and EGCG desorption.



**FIG. 4. Release of EGCG from calcium carbonate particles: EGCG-loaded 20% amplitude sonicated (So20-E) and EGCG-loaded 60% amplitude sonicated particles (So60-E) during 14 days of incubation in PBS at 37°C.**

The particles obtained by the 60% amplitude sonication method, both unloaded and loaded with EGCG (So60 and So60-E, respectively) were tested in contact with osteoblast-like cells in 3 different concentrations of EGCG: 1, 0.5, and 0.25 mg/ml. The same amount of particles not loaded with EGCG was also used for comparison. As a control, cells cultured in pure medium were evaluated. The Alamar Blue viability test (FIG. 5A) showed a significant decrease in cell viability for all cases as compared to the control. The loss of viability was much higher for empty So60 and reached around 60%. Concomitantly, these samples exhibited the highest cytotoxicity as studied by the LDH assay (FIG. 5B).

Interestingly, EGCG-loaded particles (So60-E) produced under the same conditions as So60 were characterized by significantly higher cell viability and lower cytotoxicity. For both unloaded So20 and EGCG-loaded particles (So20-E), cell viability was not significantly different. Intriguingly, cell viability did not depend on the amount of particles added to the cell culture wells. On the other hand, the tendency was visible with particle content in the LDH cytotoxicity test (FIG. 5B) for all samples. However, cytotoxicity was only elevated for empty So60 unloaded samples compared to the control. Other samples had a similar or lower LDH level than the control.



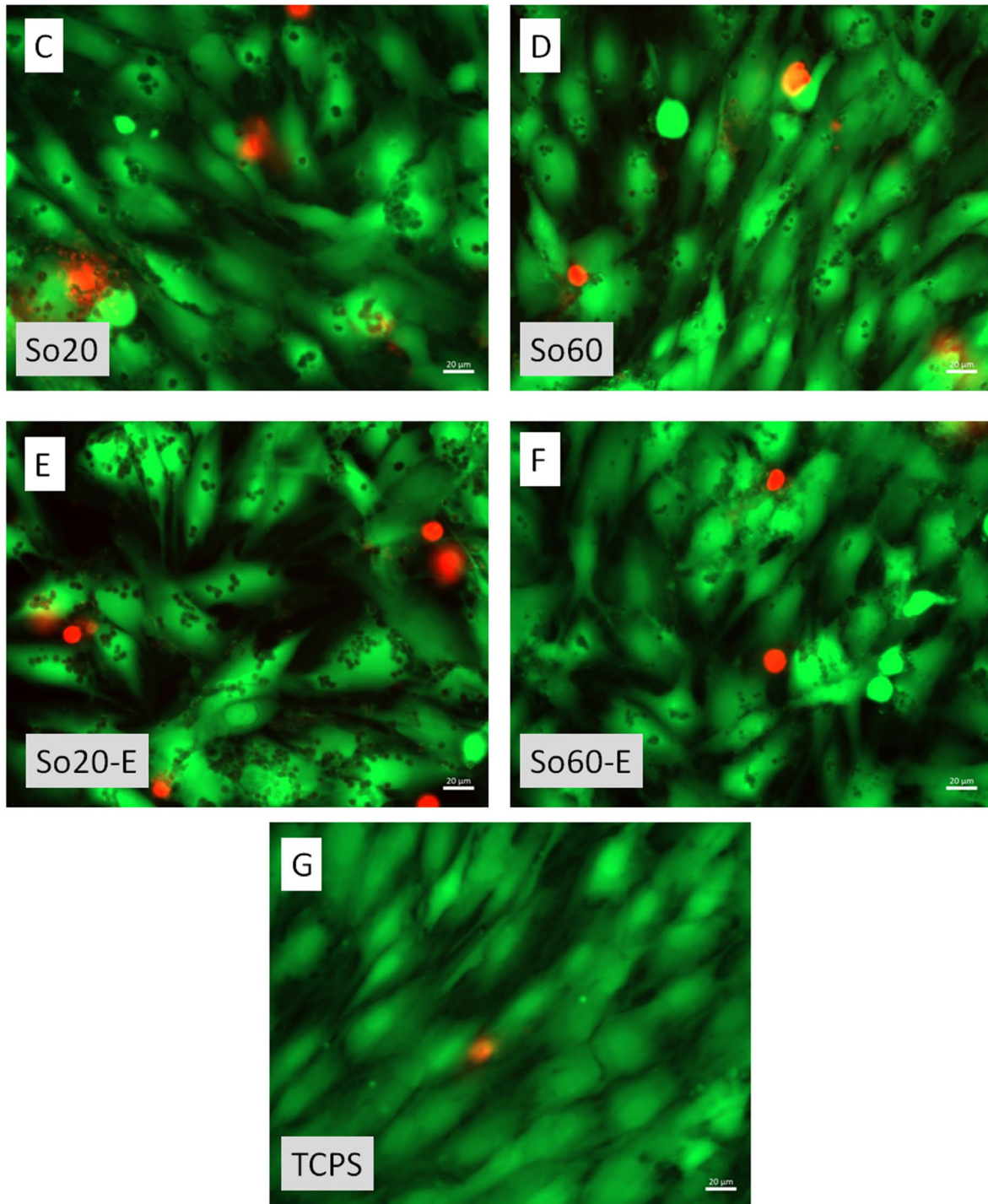


**FIG. 5.** In vitro results of MG-63 cells after 2 days of culture in contact with So20 and So60 unloaded and EGCG-loaded microparticles at 3 different concentrations: 1, 0.5 and 0.25 mg/ml in contact. Viability test (A) and LDH cytotoxicity test (B). All samples were significantly different as compared to control conditions according to ANOVA,  $p < 0.05$ . Live/dead staining for 1 mg/ml particles concentration (C-G) in comparison with culture in control conditions (tissue culture polystyrene, TCPS): green – live cells, red – dead cells. Scale bar = 20  $\mu\text{m}$ .

The live/dead staining test showed that there was only a modest change in morphology between the culture with particles compared to the control (FIG. 5C-G). The spreading area of the cells appeared slightly smaller and there were more free spaces between the cells. The results showed that the particles were found non-cytotoxic. The decrease in viability was probably related to accessibility to the surface that was hindered by the particles present. A significant cytotoxic effect was observed for the unloaded So60 samples.

This effect can be attributed to the rough and edgy surface of highly crystalline calcite particles that predominate in this case. The EGCG content in the particles did not negatively affect viability nor provoked an elevated cytotoxic effect of the particles on studied cells. On the contrary, protection of their initial spherical shape had a positive effect on proliferation and significant lowering of LDH level even compared to the control. This beneficial effect can also be derived from EGCG biological activity as it has a strong antioxidant effect [11,12].

### Hydrogels modified with mineralization and particles

Particles obtained by ultrasound loaded with EGCG were further tested as the GG-Gel hydrogel modifier. 0.15% w/v of the particles was added before gelation occurred. The gelation of the hydrogel was relatively fast (less than 2 min), which reduced the effect of possible sedimentation. The cylindrical samples were further mineralized enzymatically to introduce calcium phosphate deposits inside and create composite material for bone regeneration.

After freeze-drying porous hydrogel scaffolds were obtained (FIG. 6). The particles were distributed in the hydrogel relatively homogeneously, which was especially visible for the smaller So60 particles (FIG. 6C, E). For the samples without particles added, the pore walls were smooth (FIG. 6A).

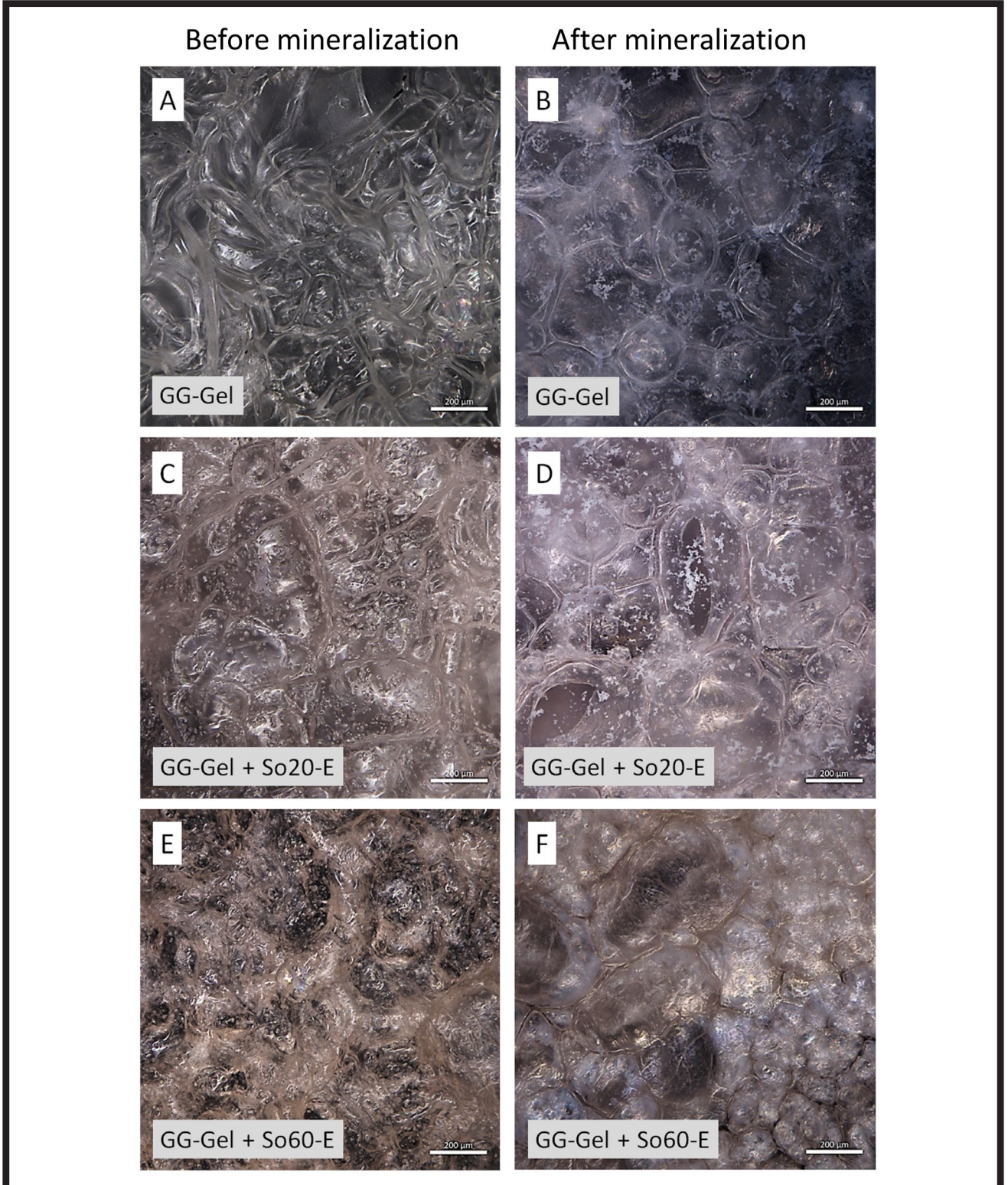


FIG. 6. Morphology by SEM of GG-Gel hydrogels: without particles before (A) and after mineralization (B) and freeze-drying. Morphology of hydrogels with particles loaded with EGCG So20-E and So60-E, before (C, E) and after mineralization (D, F) and freeze-drying. Scale bar = 200 µm.

The SEM images (FIG. 7) on cryosection revealed that the pores were 200-500  $\mu\text{m}$  in size for the unmodified hydrogel (FIG. 7A) and the one modified with So20-E (FIG. 7C), while much smaller, i.e. 50-100  $\mu\text{m}$ , for the So60-modified hydrogel (FIG. 7E). The presence of So60-E particles also led to a denser and collapsed structure. The particles were not clearly visible on the SEM images as they might have been closely entrapped within the hydrogel matrix.

Mineralization introduced precipitates of inorganic phosphates for all materials, as shown in our previous studies [5,8,13]. Bigger precipitates were visible in GG-Gel and GG-Gel+So20 samples (FIG. 6B, D). No precipitates outside the hydrogel were visible for GG-Gel+So60 (FIG. 6F). However, in this case mineralization also took place, judging by SEM images and the change in colour of the scaffolds. SEM images (FIGS. 7B, D, F) showed that in all cases mineralization led to the thickening of scaffold walls and caused calcium phosphate deposition on a surface. For GG-Gel+So60, precipitates were again hardly visible.

The presence of particles clearly affected the freeze-drying and mineralization process. Small particles can act as nucleation sites for calcium phosphate crystallization during mineralization. It can be observed for smaller So60 particles as their size is around 1-2  $\mu\text{m}$ . In that case, the mineralization is more homogeneous, and there are no precipitates inside the pores. Pore sizes in the nonmineralized material were much smaller but after mineralization this effect was reversed. All mineralized samples had a similar pore size. The reason for this effect remains unclear. Bigger particles did not affect the mineralization process, and obtained porosity was comparable with that of the non-modified GG-Gel hydrogel. It may be related to a smaller overall exposed surface area and a lower tendency to recrystallize in aqueous conditions. GG-Gel+So60 samples after mineralization had a smoother surface compared to other materials.

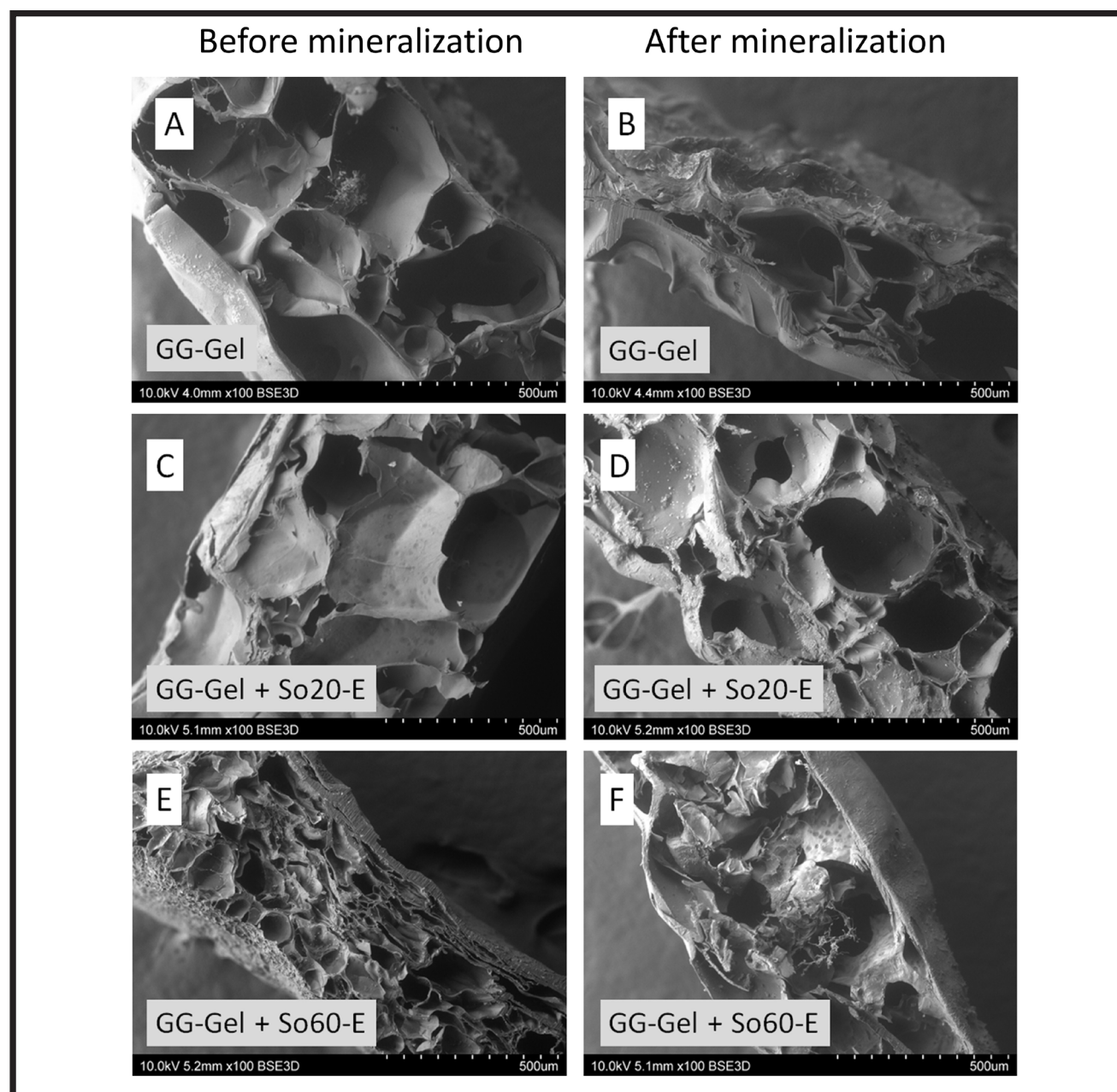
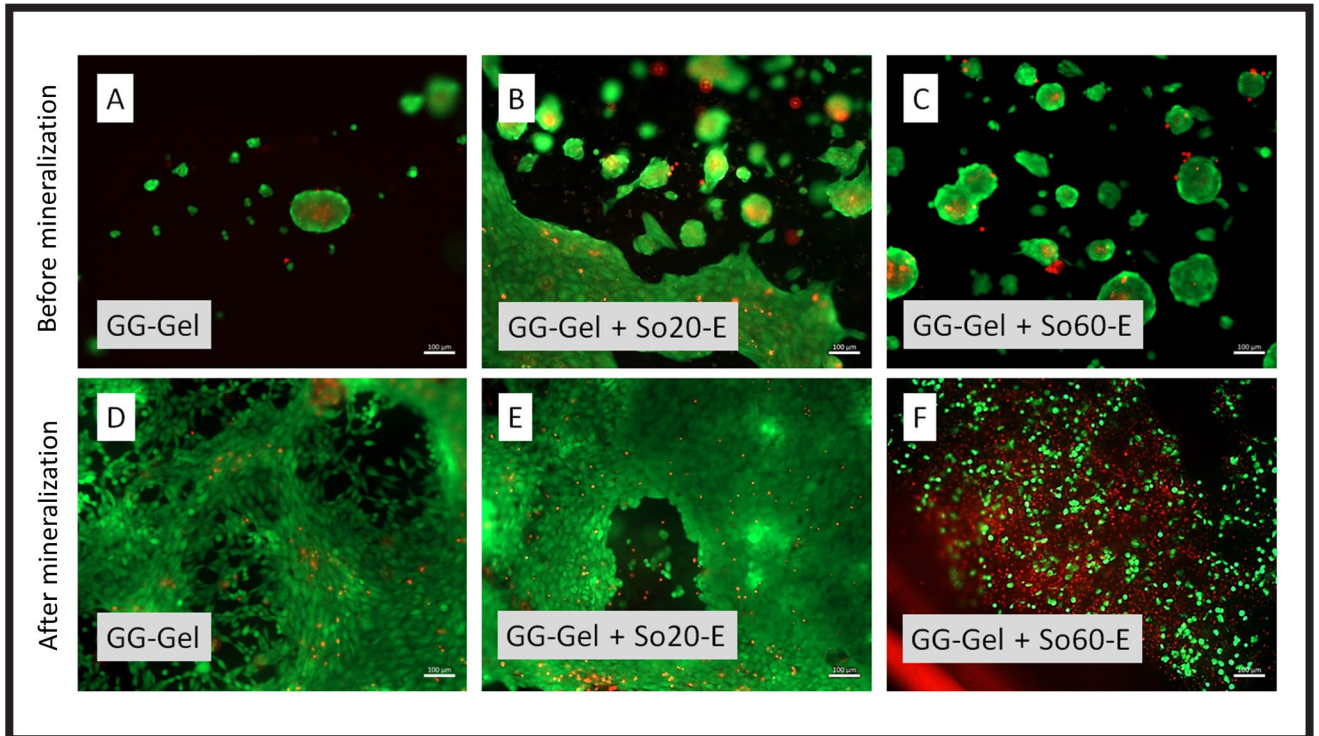


FIG. 7. SEM images of cross-sectioned freeze-dried GG-Gel hydrogels without particles before (A) and after mineralization (B). Morphology of hydrogels with particles So20-E and So60-E, before (C, E) and after mineralization (D, F). Scale bar = 500  $\mu\text{m}$ .



**FIG. 8.** Live-dead staining of 7-day culture of MG-63 on the surface of GG-Gel materials without particles (A, D) and with particles S020-E (B, E) and So60-E (C, F), prior (A, B, C) and after mineralization (D, E, F). Scale bar = 200  $\mu\text{m}$ .

Live/dead staining of MG-63 culture in materials revealed significant differences (FIG. 8). The introduction of particles into the material led to an increase in cell adhesion compared to the unmodified GG-Gel (FIG. 8A, B, C). Additional mineralization improved cell adhesion, except for the GG-Gel+So60-E sample (FIG. 8D, E, F). However, this deteriorating effect did not prevent cell agglomeration as in the case of nonmineralized sample. The presence of a small number and separated cells with a high percentage of dead cells may indicate a different reason for such a phenomenon. In fact, the surface of the hydrogel could be more mineralized than the rest of the hydrogel because mineralization proceeding in the presence of nucleation sites is more efficient. The higher level of mineralization may negatively affect the gel stability in an aqueous solution. Stronger mineralization can be toxic. In addition, swelling of interior parts of the scaffold can cause cracking of a rigid calcium phosphate layer on the surface and disintegration of the sample structure. Cells within deeper cracks could not have access to nutrients or lack stable support, which is crucial for anchorage-dependent cells, such as osteoblasts. This hypothesis is supported by the fact that a lot of dead cells were visible below the hydrogel surface.

## Conclusion

In our study, calcium carbonate microparticles of various sizes were produced by alternating shear force during the precipitation process. The feasibility of introducing EGCG into microparticles was confirmed, as well as its gradual release. EGCG had a beneficial effect on the stability of calcium carbonate microparticles, preventing its phase transformation from vaterite into calcite. The biocompatibility of smaller particles was confirmed in cell culture.

The introduction of EGCG had a beneficial effect in reducing the cytotoxicity of the crystallized particles. Particles introduced into the hydrogel influenced the microstructure of the scaffolds, lowering the pore size. The mineralization process was also affected by the presence of the microparticles that can act as nucleation sites for calcium phosphate crystal formation, causing the mineralization to be more homogenous. The particles present in the hydrogel significantly improved cell adhesion. Mineralization with calcium phosphate combined with calcium carbonate microparticles addition had even more substantial effect on scaffolds microstructure and biological properties.

Our study confirmed that the GG-Gel hydrogel can be enriched with EGCG-loaded  $\text{CaCO}_3$  microparticles and this material can be further modified with enzymatic mineralization introducing calcium phosphates. These modifications can have a positive effect on biocompatibility with bone cells, thus promising to obtain scaffolds for bone tissue regeneration.

## Acknowledgements

*This study was supported by the National Science Centre Poland (No 2018/29/N/ST8/01544) and by the program "Excellence Initiative—Research University" for AGH University of Science and Technology, Kraków, Poland.*

## ORCID iD

K. Pietryga:

A.-A. Panaite:

E. Pamuła:

<https://orcid.org/0000-0002-6343-8849>

<https://orcid.org/0009-0007-4073-370X>

<https://orcid.org/0000-0002-0464-6189>

## References

- [1] Florencio-Silva R., Sasso G.R. da S., Sasso-Cerri E., Simões M.J., Cerri P.S.: Biology of Bone Tissue: Structure, Function, and Factors That Influence Bone Cells. *BioMed Res Int* 2015 (2015) 1–17. <https://doi.org/10.1155/2015/421746>.
- [2] Roseti L., Parisi V., Petretta M., Cavallo C., Desando G., Bartolotti I., et al.: Scaffolds for Bone Tissue Engineering: State of the art and new perspectives. *Mater Sci Eng C* 78 (2017) 1246–1262. <https://doi.org/10.1016/j.msec.2017.05.017>.
- [3] Jiang S., Wang M., He J.: A review of biomimetic scaffolds for bone regeneration: Toward a cell-free strategy. *Bioeng Transl Med* 6 (2021) <https://doi.org/10.1002/btm2.10206>.
- [4] Douglas T.E.L., Messersmith P.B., Chasan S., Mikos A.G., de Mulder E.L.W., Dickson G., et al.: Enzymatic Mineralization of Hydrogels for Bone Tissue Engineering by Incorporation of Alkaline Phosphatase. *Macromol Biosci* 12 (2012) 1077–1089. <https://doi.org/10.1002/mabi.201100501>.
- [5] Pietryga K., Reczyńska-Kolman K., Reseland J.E., Haugen H., Larreta-Garde V., Pamuła E.: Biphasic monolithic osteochondral scaffolds obtained by diffusion-limited enzymatic mineralization of gellan gum hydrogel. *Biocybern Biomed Eng* 43 (2023) 189–205. <https://doi.org/10.1016/j.bbe.2022.12.009>.
- [6] Dorati R., DeTrizio A., Modena T., Conti B., Benazzo F., Gastaldi G., et al.: Biodegradable Scaffolds for Bone Regeneration Combined with Drug-Delivery Systems in Osteomyelitis Therapy. *Pharmaceuticals* 10:96 (2017) <https://doi.org/10.3390/ph10040096>.
- [7] Villarreal-Otalvaro C., Coburn J.M.: Fabrication Methods and Form Factors of Gellan Gum-Based Materials for Drug Delivery and Anti-Cancer Applications. *ACS Biomater Sci Eng* 2021:acsbiomaterials.1c00685. <https://doi.org/10.1021/acsbiomaterials.1c00685>.
- [8] Douglas T.E.L., Pilarz M., Lopez-Heredia M., Brackman G., Schaubroeck D., Balcaen L., et al.: Composites of gellan gum hydrogel enzymatically mineralized with calcium-zinc phosphate for bone regeneration with antibacterial activity: Antibacterial hydrogels mineralized with Ca-Zn phosphate. *J Tissue Eng Regen Med* 11 (2017) 1610–1618. <https://doi.org/10.1002/term.2062>.
- [9] Fadia P., Tyagi S., Bhagat S., Nair A., Panchal P., Dave H., et al.: Calcium carbonate nano- and microparticles: synthesis methods and biological applications. *3 Biotech* 11:457 (2021) <https://doi.org/10.1007/s13205-021-02995-2>.
- [10] Sovova S., Abalymov A., Pekar M., Skirtach A.G., Parakhonskiy B.: Calcium carbonate particles: synthesis, temperature and time influence on the size, shape, phase, and their impact on cell hydroxyapatite formation. *J Mater Chem B* 9 (2021) 8308–8320. <https://doi.org/10.1039/D1TB01072G>.
- [11] Honda Y., Takeda Y., Li P., Huang A., Sasayama S., Hara E., et al.: Epigallocatechin Gallate-Modified Gelatin Sponges Treated by Vacuum Heating as a Novel Scaffold for Bone Tissue Engineering. *Molecules* 23:876 (2018) <https://doi.org/10.3390/molecules23040876>.
- [12] Song L., Xie X., Lv C., Khan A. ur R., Sun Y., Li R., et al.: Electrospun biodegradable nanofibers loaded with epigallocatechin gallate for guided bone regeneration. *Compos Part B Eng* 238 (2022) 109920. <https://doi.org/10.1016/j.compositesb.2022.109920>.
- [13] Pietryga K., Costa J., Pereira P., Douglas T.E.L.: Promotion of bone cells growth on gellan gum hydrogels by enzymatic mineralization. *Eng Biomat* 125 (2014) 6–12.

# VASCULAR STENTS – MATERIALS AND MANUFACTURING TECHNOLOGIES

KLAUDIA MALISZ\* , BEATA ŚWIECZKO-ŻUREK 

INSTITUTE OF MACHINES AND MATERIALS TECHNOLOGY,  
FACULTY OF MECHANICAL ENGINEERING AND SHIP  
TECHNOLOGY, GDAŃSK UNIVERSITY OF TECHNOLOGY,  
11/12 NARUTOWICZA STR., 80-233 GDAŃSK, POLAND  
\*E-MAIL: KLAUDIA.MALISZ@PG.EDU.PL

## Abstract

*The objective of this article is to present materials and technology for the manufacture of vascular stents with appropriate design requirements. The use of the right material is very important in implantology. A biomaterial introduced into the circulatory system must be biocompatible and hemocompatible. At the same time, it should not initiate toxic, mutagenic, or immunological reactions. Currently, 316L stainless steel (316L SS), nitinol (Ni-Ti alloy) and cobalt-chromium alloy (Co-Cr) are used as standard stent materials. Additionally, drug-containing coatings are used to provide antithrombotic properties. Nowadays, scientists are trying to create biodegradable stents (BDS) using magnesium (Mg) or zinc (Zn) alloys.*

*Laser methods are generally used to manufacture stents using Nd:YAG lasers with a pulse length in the range of several milliseconds. Material removal is based on the ejection of the melt using a high-pressure gas. The result is remelting and heat-affected zones. Various post-processing procedures are necessary to remove residues, including etching and electropolishing. Minimizing the heat-affected zone could be achieved by using femtosecond lasers. Additionally, immersion of the material in water prevents the deposition of residues on the workpiece. Interesting alternatives used in the manufacture of vascular stents are electrospinning or additive techniques. 3D printing enables obtaining of geometrically complex and personalized implants and reduces the consumption of materials and the production of waste.*

**Keywords:** vascular stents, biomaterials, laser processing, 3D printing, electrospinning, post-processing

## Introduction

The development of interventional medicine has revolutionized the treatment and prevention of ischemic diseases. Cardiovascular diseases are one of the main causes of death in our century, and percutaneous coronary angioplasty is one of the most popular methods of their treatment. In Poland, more than 80% of such procedures involve stent implantation. The cause of ischemic disease is atherosclerosis of blood vessels resulting from long-term inflammation in the vascular wall [1,2].

[*Engineering of Biomaterials 166 (2022) 22-28*]

doi:10.34821/eng.biomat.166.2022.22-28

Submitted: 2023-01-16, Accepted: 2023-02-20, Published: 2023-02-28



Copyright © 2022 by the authors. Some rights reserved.  
Except otherwise noted, this work is licensed under  
<https://creativecommons.org/licenses/by/4.0>

Stents are a type of metal, elastic scaffold with a spatial cylindrical structure and small size. They are implanted in place of a critically narrowed section of the coronary artery to support its walls and widen its lumen. The initial experience with stent implantation was not very encouraging, i.e. blood clotting was common, resulting in secondary arterial occlusion and acute complications. This led to myocardial ischemia and even death of a patient [1]. Today, the phenomenon of restenosis has been reduced due to the use of drug-eluting stents (DES). Still, restenosis may occur as a result of damage to the blood vessel wall during stent implantation, thrombosis, and allergic reactions caused by ion release. Hyperplasia (hypernormal proliferation) of fibroblasts and smooth muscle cells is another potential cause of stent restenosis. Restenosis can be observed in the angiographic examination as a sudden reduction in vessel diameter by at least 50% compared to the value obtained during the angioplasty procedure [1,3-5].

The endovascular implant must be characterized, among others, by flexibility, ease of movement in the catheter and arteries, low thrombogenicity (protecting against blood clots and relapses), tissue neutrality, good extensibility (facilitating the expansion mechanism), resistance to external forces, small total stent surface, and good coverage of the vessel wall. Materials intended for a given type of an implant include austenitic steel, nitinol, tantalum, cobalt alloys, and polymer stents, which can be divided into two groups: self-expanding elastic vascular stents implanted in arteries exposed to movement and bending, and non-deformable elastic cardiological stents implanted in arteries running inside the heart muscle [1,2,6].

## Biomaterials used for vascular stents

The first types of stents used for coronary applications were bare metal stents (BMS). These stents are typically made of 316L stainless steel, platinum-iridium alloy (Pt-Ir alloy), cobalt-chromium alloy, and nitinol. They exhibit outstanding mechanical properties and improved corrosion resistance [7]. In previous studies, intracoronary stent restenosis was reported to be between 10% and 20% during a 6-month follow-up, leading to myocardial infarction and angina, which required revascularization. Healing with bare metal stents has very beneficial results, and restenosis were observed in 20-30% of patients in 6-12 months [8].

Drug-eluting stents are composed of a metallic stent, a polymeric coating, and an immunosuppressant or antiproliferative compound as a pharmacological agent [7]. The elution from polymers is influenced by a variety of factors. The release and duration of its elution are significant in the design of a drug-eluting stent [8]. Antiproliferative drugs released from DES (such as rapamycin, paclitaxel, etc.) not only inhibit excessive smooth muscle cell proliferation and prevent in-stent restenosis, but they also prevent the adhesion and growth of the endothelial cells, leading to delayed endothelial healing, late thrombosis, late restenosis, and other clinical complications. Furthermore, the polymer-drug carriers used for DES are not sufficiently biocompatible, and after long-term implantation, degradation, aging, and peeling of the coating can put patients at risk [9-12].

The use of totally bioresorbable stents, the fourth revolution in interventional cardiology, has attracted much interest over the past ten years. The most significant innovations in biodegradable stent technology include magnesium and its alloys, which have high biodegradability, biosafety, and promising mechanical properties with a low risk of restenosis [7]. Furthermore, in addition to magnesium alloys, biodegradable stents can also be made of zinc alloys and some biodegradable polymers, i.e. poly(lactic acid) (PLA) and polycaprolactone (PCL).

These materials degrade into products, which are later metabolized by the patient. Biodegradable metal stents are designed to keep the vessel open and maintain its physiological function. As the name suggests, biodegradable stents must be able to be degraded or absorbed by the human body. They do not affect subsequent treatment, have excellent mechanical properties, that guarantee stable transfer during stent compression, and maintain a sufficient radial force to support the vessel after complete expansion of the stenotic portion. The mechanical properties and degradation time of biodegradable stents can be improved by the synthesis of various types of polymers [13-15]. Additionally, the degradation rate of the biodegradable polymer is uncontrollable, and degradation products can be caused by immune and inflammatory reactions [9, 16].

The use of pure iron (Fe) as biodegradable stents is advantageous due to its good mechanical properties, radiopacity, biocompatibility, and degradability. Fe is also essential for human life if it is kept at a moderate value. Because of its high elastic modulus, it possesses greater radial strength. Consequently, the design of stents can make use of thinner struts. Studies reported no inflammation, neointimal proliferation, or thrombotic events during the follow-up of 6-18 months, but the higher degradation rate is desired for Fe stents so without any changes to their corrosion rate, they cannot be used in stent applications, because they would face similar problems as permanent stents [17, 18].

Researchers are also investigating zinc alloys for BDS. Many studies have shown that Zn degradation rate is slower than that of Mg and faster than Fe, which makes it a good candidate for this application. In addition, it has acceptable biocompatibility but low mechanical properties, preventing the use of Zn in stents. It is possible to add alloying elements; however, it should be taken into account, that some elements cannot exist in the human body, and others affect the rate of degradation, corrosion homogeneity, and elongation to failure [17]. Despite the advantages of zinc-based materials, the aging of zinc alloy makes the mechanical properties of zinc stents unstable. Vascular stents exhibit heterogeneous deformation during compression and expansion. Work-softening can prevent the stent from being firmly fixed on the balloon during compression and makes it easy to move during implantation while work-hardening can cause the stent to expand and deform unevenly. On the other hand, low density and good in vivo support performance are all characteristics of the magnesium alloy. Jiang J. et al. [19] fabricated biodegradable Zn-2.0Cu-0.5Mn alloy microtubes and vascular stents to improve the mechanical properties of pure Zn elements. The microtubes and vascular stents were manufactured by a combined process of extrusion, drawing, laser cutting, and electrochemical polishing. As-drawn microtube demonstrated appropriate mechanical properties as a stent material with an ultimate tensile strength of around 298 MPa and an elongation of approximately 26%. Additionally, the processed stent with a thickness of about 125  $\mu\text{m}$  possessed sufficient radial strength of about 150 kPa and good balloon expandability. This research suggested that the biodegradable Zn-2.0Cu-0.5Mn alloy is a good candidate for this application [19]. Another solution was proposed by Niu J. et al. [20]. They developed a new Zinc-4 wt% copper alloy (Zn-4Cu) as a biodegradable material. Cu was selected for its ability to promote the proliferation of vascular endothelial cells, thereby accelerating the revascularization process. Hot extrusion was applied to Zn-4Cu to refine the microstructure. It should improve the mechanical properties and corrosion resistance of the Zn alloy. After extrusion, the dendritic CuZn5 phases were broken and distributed along the extrusion direction. In vitro studies showed that Zn-4Cu presents acceptable toxicity to human endothelial cells.

Additionally, it could effectively inhibit bacteria adhesion and biofilm formation. Moreover, the Zn-4Cu alloy exhibits excellent strength and ductility; it is also characterized by uniform and slow degradation, good biocompatibility, and a significant antibacterial effect [20].

The magnesium alloy is biodegradable and may provide advantages over conventional non-biodegradable metal stents in preventing chronic inflammation, late thrombosis, and long-term use of antiplatelet medications. Effective solutions are used to solve the poor mechanical properties and high rate of corrosion of magnesium-based materials, e.g. heat treatment can change the second phase's shape, distribution, and internal structure. Additionally, plastic deformation can improve mechanical properties by improving dynamic recrystallization grain quality and reducing structure segregation. Furthermore, surface modification may protect the substrate from corrosion by preventing direct contact with body fluids. However, Mg alloys produce a large amount of hydrogen during the degradation process, which causes an increase in pH in the environment of the surrounding tissues. This phenomenon is disadvantageous; it can reduce the adhesion and growth of endothelial cells on the surface, and thus may cause acute and long-term complications [9, 21, 22].

To improve the biocompatibility and corrosion resistance of the magnesium alloy, Pan C. et al. [23] used chitosan functionalized graphene oxide loaded with  $\text{Zn}^{2+}$  and propranolol. They also evaluated anticorrosion properties, hemocompatibility, and endothelial cell growth behavior. Research [23] shows, that multifunctional coating can significantly enhance the corrosion resistance and minimize the degradation rate of the Mg alloy. Additionally, the blood compatibility of the coating was improved due to the inhibition of platelet adhesion, activation, and reduction of hemolysis rate [23]. However, Wang Y. et al. [24] constructed a nanocoating on Mg alloy for vascular stent application. A rapamycin-loaded nanocoating consisting of the  $\text{MgF}_2$  layer, the polydopamine layer, and targeted rapamycin-loaded nanoparticles was constructed on Mg-Zn-Y-Nd alloy (ZE21B) to improve its corrosion resistance and especially modulate smooth muscle cells. The results showed that rapamycin-loaded nanocoating reduced the degradation rate of the Mg alloy, but also improved the hemocompatibility of the material. Rapamycin-loaded nanocoating on ZE21B alloy, according to the results of in vitro cell tests, selectively inhibited the proliferation and migration of vascular smooth muscle cells, while having only marginal effects on the proliferation of vascular endothelial cells [24].

In recent years, there has been a lot of interest in functional coatings as a way to improve the performance of implants. Saadatlou G. et al. [25] presented, prepared, and characterized a tetra-functional coating exhibiting anticorrosion, antibacterial, biocompatible, and anticoagulant properties. Poly(2-ethyl-2-oxazoline)-co-polyethyleneimine (PEOX-co-PEI) stabilized silver nanoparticles (AgNPs) and heparin were used to prepare the multifunctional multilayers. The coatings were deposited on nitinol and 316L stainless steel substrates using the layer-by-layer technique, which involves sequential adsorption of complementary species with intermolecular forces such as hydrogen bonding and electrostatic interactions. Anticoagulation is generally provided by heparin. Heparin has the potential to enhance the hemocompatibility of surfaces because it inhibits blood clotting by attaching to and deactivating thrombin, a blood protein that causes coagulation. AgNPs provide antibacterial properties, and polycationic polymers, such as polyethyleneimine attracted great attention to inhibit metal corrosion.

The copolymer (PEOX-co-PEI) is temperature and pH-responsive and can provide the conditions for hydrogen-bonded assemblies. Such a combination of materials meant that the prepared coatings showed anti-corrosion, antibacterial, biocompatible, and anticoagulant properties at the same time [25].

Another way to improve the biocompatibility of stents was proposed by Li P. et al. [26], i.e. novel co-immobilization of molecules for the multifunctional coating of cardiovascular materials via layer-by-layer self-assembly. They created a phospholipid-based multifunctional coating with phospholipids-based polymers, type I collagen (Col-I), and Arg-Glu-Asp-Val (REDV) peptide. Their results showed that the multifunctional coating (Ti-PMMDA-Col-I-POMDA-REDV) could not only strongly inhibit platelet adhesion and smooth muscle cell proliferation, but also promote endothelial cell proliferation [26].

Among thin coatings, those containing titanium dioxide ( $\text{TiO}_2$ ) are gaining a lot of interest. Thin films of titanium dioxide do not corrode or release harmful ions into solutions. As a result, it can be regarded as bioinert and may even stop the release of metal ions (Cr, Ni) from underlying bulk material (e.g. nitinol). Nickel and aluminium ions should be avoided because they can promote oxidative effects within body fluids.  $\text{TiO}_2$  is characterized by low cost, non-toxicity, but also appropriate physical, mechanical, and dielectric properties for medical applications. In addition, it shows high biocompatibility [5,27,28]. Sun Z. et al. [5] used nitrogen doping of titanium dioxide thin films to improve the biological properties and biocompatibility of the coating. The titanium oxide thin films were fabricated by magnetron sputtering in a reactive gas atmosphere consisting of argon and oxygen in the first case and argon, nitrogen, and oxygen in the second case. Control of the nitrogen and oxygen gas flow rates and their mixing ratios allow adjustment of the nitrogen-doping level within the titanium dioxide thin films. The surface energy, wettability, cell adhesion, and consequently cellular proliferation on top of the thin films were all impacted by different nitrogen doping amounts. The results showed that the 1.5 times more nitrogen-doped titanium dioxide thin film can be used to modify the surface of stents to reduce the risk of vascular stent restenosis [5].

Diamond-like carbon (DLC) coatings have excellent mechanical properties, a low coefficient of friction, wear resistance, strong adherence to the substrate, and high biocompatibility. Furthermore, DLC films can enhance endothelialization on vascular stents and reduce thrombotic clots [29,30]. Modern DLC-coated Co-Cr stents demonstrated more effective fibrin deposition and platelet activation prevention and more comprehensive and uniform endothelialization, which reduced the incidence of thrombotic clots. Due to the coating's decreased inflammatory activation, the vascular repair was stabilized within 30 days [30,31]. Numerous studies have suggested a connection between surface energy, wettability, and cell adhesion in DLC films. They claimed that blood cell adsorption was commonly prevented by hydrophobic surfaces. Fluorocarbon polymers are well known for having exceptional water-shedding properties when it comes to hydrophobicity [30,32,33]. Additionally, platelet adhesion and activation on the surface of the F-DLC films were significantly reduced. Saito T. et al. [32] showed that the addition of fluorine considerably increased the antithrombogenicity of DLC coatings [32].

## Design requirements for the manufacture of vascular stents

Vascular stents should be scientifically and rigorously designed and developed to ensure, that the stent can effectively treat blocked blood vessels, open up thrombi, and restore vascular functions [34]. Specific design requirements must be met and appropriate material properties must be ensured to safely introduce the stent to the target site and minimize the risk of restenosis.

Radial force plays a key role in preventing stent retraction by providing radial or structural support to the vessel. The ability of the stent to move through the vessel to its destination using the recommended accessories is also important. It depends on the low friction and high flexibility of the stent body. The profile of the stent defines the maximum diameter along the device. To avoid disruption of blood flow during implantation, the stent should have a minimal profile. Accurate placement of the stent is very important during vessel dilation, so it should have minimal foreshortening. Another important aspect is the optimal scaffold that minimizes the aggressive thrombotic response to the stent material, for this purpose, the smallest possible contact surface of the stent with the blood vessel should be ensured [35].

Each material must also be evaluated in terms of biocompatibility, as it must not cause adverse reactions in the body. Evaluation for stent visualization by fluoroscopy is also required both during insertion and after withdrawal of the delivery system. To place the stent in the correct position, the absorption of X-rays by the material is very important to obtain a good image and minimize the risk of vessel damage. It is also necessary to evaluate the stent's susceptibility to corrosion in a real or simulated environment. Corrosion mechanisms can include pitting, crevice, and galvanic corrosion. Each corrosion mechanism should be properly evaluated for the specific stent design. For example, fretting corrosion should be evaluated for stents that can be used with a tab. Another evaluation criterion is fatigue safety. Fatigue stress or strain analysis requires the determination of average and cyclic stresses or strains and comparison with the corresponding properties of the material. The selection of the stent material is such that it can withstand at least 380 million cyclic loads, i.e. up to 10 years of presence in the body. The resistance to the occurrence of cracks on the stents is particularly important from the point of view of their safe use. Stent ruptures can be initiated by all kinds of structural defects in the volume of the material, as well as by defects on the surface (notches, cavities, pits) [35].

The requirements for the biodegradable metallic stent tube include aspects such as degradations, biocompatibility, and mechanical properties. For degradation, scaffold integrity of 3-6 months and complete dissolution of 1-2 years are important. Biocompatibility requirements are non-toxicity of the material, no tissue inflammatory response, and no harmful release and/or residence of particles. The requirements for mechanical properties include tensile yield strength  $\text{TYS} > 200 \text{ MPa}$ , tensile strength  $\text{UTS} > 300 \text{ MPa}$ , tensile elongation  $> 15-18\%$ , and elastic recoil  $< 4\%$  [17]. The mechanical properties of the metals used for vascular stents are shown in TABLE 1.

Stent manufacturing technologies are most often based on laser cutting of an openwork structure from tubes of a specific diameter [35]. Other methods include the braided technique, electrospinning generation, and additive production generation [8].

**TABLE 1. Mechanical properties of metals used for stents [36-40].**

Material	Elastic modulus [GPa]	Yield strength [MPa]	Tensile strength [MPa]	Elongation [%]
Ti6Al4V	110	795	860	10
Ta	190	138	207	30
316L SS	196-210	205	515	40
CoCrMo	210	450	655	8
Ni-Ti	20-50 martensitic phase; 40-90 (approx. 83) austenitic phase	70-140 martensitic phase; 195-690 austenitic phase	895	25-50
Magnesium	41-45	65-100	207	2
Iron	200	150	210	40

## Laser processing in the manufacture of coronary stents

The most typical technique used to make a vascular stent is laser cutting. During the laser cutting process, a high-power laser beam focuses on the tubular material, the material melts, evaporates, or wears out rapidly, and then the material is blown away by high-velocity airflow [8].

Due to the requirements for precise coronary stent sizes, e.g. diameter 2.5-4.0 mm, length 8-38 mm, and wall thickness 80-100  $\mu\text{m}$ , high accuracy is essential in its production. Nd:YAG, fiber, and disk lasers are used for this purpose. Process parameters include average power, pulse repetition rate, pulse width, processing speed, and energy. The heat-affected zone is proportional to the laser-matter interaction time. Lasers with short pulse duration, such as picosecond and femtosecond lasers, have no or minimal heat-affected zone, offering the best quality in stent fabrication [35].

Typical laser cutting processing involves CAD design with an optimized stent configuration, then the design is transferred to the laser processing system. The metal tube is mounted on the lathe with a Teflon rod passing through the inner diameter of the tube. The tube is then rotated and moved longitudinally relative to the laser to produce the desired programmed pattern [35].

After laser processing, it is common to encounter abrasive sticking to the underside of the cut as a result of the temperature gradient, beam divergence, and turbulent gas stream. To remove the abrasive and the oxide layer, etching is used, i.e. the laser-processed part is immersed in a thermoplastic tank containing dilute HCl. The use of ultrasound can improve the efficiency of digestion. The state-of-the-art surface finishing process for metallic stents is electropolishing, used to remove abrasive and contaminants, as well as metallic and non-metallic inclusions (introduced during production) and the heat-affected zone, eliminating surface irregularities, but also rounding off sharp edges and increasing corrosion resistance. In addition, electropolishing improves reflectivity and surface brightness [35]. Examples of the electrolyte composition and operating conditions used for electropolishing of the stent are shown in TABLE 2.

A new approach to stent processing using a 100 fs pulsed laser uses immersion of the treated material in a liquid. It has been shown that femtosecond lasers can provide high-quality cut surfaces without a heat-affected zone with optimal selection of parameters in both cutting environments. However, the main obstacles to the use of this technology in the air environment are the residues (in the form of deposits of previously evaporated material) and the remelted layer.

**TABLE 2. Composition of solutions used for polishing and working conditions [35,41,42].**

1 [35]		2 [41]		3 [42]		4 [42]	
Solution	Contents, parameter values	Solution	Contents, parameter values	Solution	Contents, parameter values	Solution	Contents, parameter values
H <sub>3</sub> PO <sub>4</sub> (85%)	650 ml/l	H <sub>3</sub> PO <sub>4</sub>	42 wt%	H <sub>2</sub> SO <sub>4</sub> (95-97%)	40 ml	H <sub>3</sub> PO <sub>4</sub> (85 wt%)	42 wt%
H <sub>2</sub> SO <sub>4</sub> (98%)	250 ml/l	Glycerol	47 wt%	H <sub>3</sub> PO <sub>4</sub> (85 wt%)	45 ml	Glycerol	47 wt%
CrO <sub>3</sub>	80 g/l	H <sub>2</sub> O	11 wt%	H <sub>2</sub> O	14 ml	H <sub>2</sub> O	11 wt%
Addition	10 g/l	Current density	1.3 A/cm <sup>3</sup>	Cathode	Stainless steel sheet	Cathode	Stainless steel sheet
Temp.	70-80°C	Time	1 min	Temp.	75°C	Temp.	90-95°C
Tension	18 V	-	-	Time	0.5 min	Time	1 min
Time	2 min	-	-	Applied voltage	3.5 V	Applied voltage	10-12 V
Cathode and anode surface	4:1	-	-	Anodic current	0.4 A	Anodic current	1.2 A
Cathode material	Stainless steel	-	-	-	-	-	-

Residues can be removed by ultrasonic cleaning, while the melted part is permanently attached to the material and requires subsequent treatment [43].

The presence of water around the workpiece minimizes the redeposition of material, resulting in a better cut surface finish and eliminating the need for residue removal. In addition, it has been observed that the use of water can reduce emissions of gases and particulates into the atmosphere. High-quality machining with well-defined edges, no chipping, and no remelting is achieved immediately after the cutting process. This indicates that underwater cutting can reduce the cost of the production process by reducing the need for cleaning and finishing, but it is a more energy-intensive solution [43].

## Electrospinning

Electrospinning is a unique technique that uses an applied voltage for the liquid atomization process. The electrospinning technique has undergone rapid development in recent years. This technique can provide the unlimited potential to achieve vascular implants [8]. Electrospinning is a representative technology for producing various polymer solutions into fibers using an electric field. A multifunctional stent, such as one with a biodegradable coating and a drug-release mechanism, can be created using electrospinning. However, there are several disadvantages, such as weak mechanical properties and peeling from the stent due to the features of the electrospun fiber [44,45]. Electrospinning can be used to create drug-loaded stents in a variety of ways. After electrospinning, the fiber membrane is immersed in the drug solution to adsorb the drug. Emulsions for electrospinning, which can be used to create micro/nanofibers with core-shell structures, can be produced by combining the water and oil phases [46].

Chan Lee J. [44] used silicone to fabricate a silicone/polycaprolactone (PCL) multilayer film for stent coating. They received a multilayer membrane with high mechanical properties. Furthermore, the multilayer membrane cured at a low temperature had no problem with cell growth [44]. Chalony C. et al. [47] tried to create a drug-free coating on vascular stents that prevents cellular and platelet adhesion. To achieve this goal, they used co-axial electrospinning of Poly-ethyl-2-cyanoacrylate (PECA) and Polyurethane (PU). This drug-free stent coating was developed that attenuates biological element adhesion. Furthermore, the coating was characterized by hemocompatibility and biocompatibility, and it also had adequate mechanical strength [47].

## 3D printing technologies in the production of vascular stents

Additive techniques use material addition, resin curing, or powder sintering a specific model by applying successive thin layers of material. The accuracy of technological machines creating real "layer-by-layer" models is determined, among others, by the thickness of the built layer. Incremental methods include, among others: stereolithography (SLA, Stereolithography), Selective Laser Sintering (SLS), Selective Laser Melting (SLM), modeling with liquid thermoplastic (FDM -Fused Deposition Modeling) [48].

Stereolithography consists of polymerization (photocuring) of liquid acrylic or epoxy resin with a UV laser beam. The platform on which the model is created is lowered by a layer thickness, while the scraper levels and applies a new layer of liquid resin. The accuracy of the model is affected by the thickness of the hardened layer, the type of resin, or the diameter of the laser spot. In the FDM method, the model is built in layers from a polymer extruded from the nozzle. The material (round plastic wire, wrapped on a spool) is melted in a heated nozzle to the appropriate flow temperature and then applied to the build platform, where it merges with the previous layers as it cools. Selective laser sintering of powders of various materials, i.e. polymers or metals, consists in combining powders as a result of their melting. Some materials (e.g. metal powders) require additional coating with substances that are a kind of binder melted with the use of a laser and binding powder particles. Sometimes, to increase the strength or density of the material obtained by the SLS technique, it is required to infiltrate the pores remaining between the particles, e.g. in the case of steel, infiltration is performed using copper alloys. Using SLM methods, components can be produced from virtually any material that can be powdered and melted. Most often, stainless steel, titanium, and its alloys are used; it is also possible to use low-melting materials, e.g. zinc alloys. Thanks to the full remelting of the material, no pores are formed and infiltration is not required [48].

Metal stents, due to the inability to dissolve in the body, remain permanently in the human blood vessel. Chronic exposure of the vessels to the presence of a foreign body may result in a decrease in their elasticity, which leads to restenosis in the stent. Therefore, biodegradable stents are of interest to scientists. 3D printing is of great importance in their production, which is economical and allows the development of innovative stent models, and gives the possibility of implant personalization [13,49]. Despite its exceptional accuracy and precision, laser cutting is a thermal process that can lead to structural problems such as residual stresses, micro-cracks, or, more commonly, heat-affected zones. In addition, surface finishing further increases the price of stents. Despite many advantages of additive methods, the SLM technique involves the use of high processing temperatures, which can cause damage to the material similar to laser cutting and requires subsequent surface finishing [14].

Due to the growing interest in printed implants, scientists investigated the effect of nozzle temperature, material flow, and speed on the accuracy of FDM printing. They found that both material flow and nozzle temperature strongly influenced the fineness of the process, as opposed to speed. Due to the ultrashort pulse emission duration of femtosecond lasers as well as the fact that the majority of the heat is removed by gas-phase evaporation, the area of the workpiece surface affected by thermal diffusion is incredibly small. Additionally, femtosecond lasers can achieve great processing precision and postprocessing workpiece surface quality and are applicable for use in micromachining [13]. When considering bioresorbable stents, it is necessary to evaluate the degradation of the material. For a lower fill percentage, the number of pores inside the printed structure will be greater. As a consequence, it will facilitate the degradation process, thanks to a larger contact surface, which easily allows the diffusion of water molecules, and thus the hydrolysis of the material and its resorption. However, an increase in percentage fill leads to a higher tensile strength value. In addition, the bending properties depend on the percentage of filling.

Furthermore, as the layer thickness decreases, the load resistance increases, which means that vascular stents should be printed with a minimum layer thickness to achieve better radial strength and withstand the loads imposed by arterial walls. The reduction of layer thickness correlates with greater bending strength, which is important due to the good fit of the stent to the blood vessel [14].

Coronary artery stents can be as small as 1 mm in diameter, so there is a technical challenge in 3D printing these implants. Virtual testing using finite element analysis makes it possible to predict the material behavior of selected nonresorbable polymers in a closed artery. A virtual testing framework is a numerical platform designed to realistically reproduce the characteristics of a physical experiment/study. This method makes it possible to improve processes and assess the behavior of materials. In addition, it also helps to shorten the time needed from the conceptualization of the project to market launch [50].

## Conclusions

A stent implantation is associated with the risk of restenosis, which is why scientists continue to improve the properties of stents and research is conducted on new manufacturing technologies, surface modification, and methods of drug release. The coating is supposed to enhance antithrombotic properties and reduce the possibility of migration of alloy metals to the surrounding tissues. Nowadays, biodegradable materials, such as magnesium and polymers, which are supposed to reduce the risk of late complications, are becoming more and more popular.

The production of vascular stents has been dominated by laser processing methods, where the Nd:YAG laser is mainly used. It works well for steel and nitinol stents. Before introducing new materials to the market, the stent is tested and evaluated in many ways to ensure that it is as demanded. Manufacturing technology must ensure appropriate surface smoothness, edge rounding, and high dimensional accuracy. The main problem of laser processing is the heat-affected zones, which significantly reduce the strength of the material, to minimize their occurrence, the duration of the pulses should be shortened – that is why femtosecond lasers are characterized by the best results. In addition, immersion of the material in water prevents the deposition of residues on the workpiece. Another possibility for producing vascular stents is the use of additive techniques, which by adding thin layers of material, i.e. by hardening the resin or sintering powders, to build a specific model. Due to the many technological problems encountered in the 3D printing of coronary stents, virtual testing becomes useful, which allows examining the material's behavior in the occluded artery and shortens the time of introducing the appropriate project to the market.

## Acknowledgments

*This research did not receive external funding.*

## ORCID iD

K. Malisz:  <https://orcid.org/0000-0003-0596-3140>  
B. Świczko-Żurek:  <https://orcid.org/0000-0001-7742-0052>

## References

- [1] Grygier D.: Wpływ wybranych własności krzemionkowych warstw wierzchnich na możliwości ich zastosowania jako pokrycia na stenty wieńcowe. Politechnika Wroclawska 2008.
- [2] Borhani S., Hassanajili S., Ahmadi Tafti S.H., Rabbani S.: Cardiovascular Stents: Overview, Evolution, and next Generation; Springer Berlin Heidelberg 7 (2018) 175-205.
- [3] Hrycek E., Syzdół M., Wojakowski W.: Gojenie i Dysfunkcja Śród-blonka Tętnic Wieńcowych Po Implantacji Stentów Uwalniających Leki Antyproliferacyjne. Via Medica 6 (2011) 44-48.
- [4] Pietrasik A., Rdzanek A.: Restenoza po zabiegach przezskórnej angioplastyki wieńcowej - przyczyny, rozpoznawanie, postępowanie. Choroby Serca i Naczyń 14 (2017) 352-356.
- [5] Sun Z., Khlusov I.A., Evdokimov K.E., Konishchev M.E., Kuzmin O.S., Khaziakhmatova O.G., Malashchenko V.V., Litvinova L.S., Rutkowski S., Frueh J., Kozelskaya A.I., Tverdokhlebov S.I.: Nitrogen-Doped Titanium Dioxide Films Fabricated via Magnetron Sputtering for Vascular Stent Biocompatibility Improvement. Journal of Colloid and Interface Science 626 (2022) 101-112.
- [6] Bakoń A., Brzeziński M.R., Marchlewski P.: Specyfika Mechanicznej Obróbki Wykończeniowej Implantów i Endoprotez. Mechanik 8-9 (2015) 15-19.
- [7] Korei N., Solouk A., Haghbin Nazarpak M., Nouri A.: A Review on Design Characteristics and Fabrication Methods of Metallic Cardiovascular Stents. Materials Today Communications 31 (2022) 1-23.
- [8] Ahadi F., Azadi M., Biglari M., Bodaghi M., Khaleghian A.: Evaluation of Coronary Stents: A Review of Types, Materials, Processing Techniques, Design, and Problems. Heliyon 9 (2023) e13575.
- [9] Pan C., Liu X., Hong Q., Chen J., Cheng Y., Zhang Q., Meng L., Dai J., Yang Z., Wang L.: Recent Advances in Surface Endothelialization of the Magnesium Alloy Stent Materials. Journal of Magnesium and Alloys 11 (2023) 48-77.
- [10] De Luca G., Smits P., Hofma S.H., Di Lorenzo E., Vlachojannis G.J., van't Hof A.W.J., van Boven A.J., Kedhi E., Stone G.W., Suryapranata H.: Everolimus Eluting Stent vs First Generation Drug-Eluting Stent in Primary Angioplasty: A Pooled Patient-Level Meta-Analysis of Randomized Trials. International Journal of Cardiology 244 (2017) 121-127.
- [11] Cheng Q., Shafiq M., Rafique M., Shen L., Mo X., Wang K.: Extracellular Matrix and Nitric Oxide Based Functional Coatings for Vascular Stents. Engineered Regeneration 3 (2022) 149-153.
- [12] Wawrzyńska M., Duda M., Wysokińska E., Strządała L., Biały D., Ulatowska-Jarża A., Kałas W., Kraszewski S., Paślowski R., Biernat P., Paślowska U., Zielonka A., Podbielska H., Kopaczyńska M.: Functionalized CD133 Antibody Coated Stent Surface Simultaneously Promotes EPCs Adhesion and Inhibits Smooth Muscle Cell Proliferation - A Novel Approach to Prevent in-Stent Restenosis. Colloids and Surfaces B: Biointerfaces 174 (2019) 587-597.
- [13] Chang F.Y., Liang T.H., Wu T.J., Wu C.H.: Using 3D Printing and Femtosecond Laser Micromachining to Fabricate Biodegradable Peripheral Vascular Stents with High Structural Uniformity and Dimensional Precision. International Journal of Advanced Manufacturing Technology 116 (2021) 1523-1536.
- [14] Sousa A.M., Amaro A.M., Piedade A.P.: 3D Printing of Polymeric Bioresorbable Stents: A Strategy to Improve Both Cellular Compatibility and Mechanical Properties. Polymers 14 (2022) 1099.
- [15] Hua W., Shi W., Mitchell K., Raymond L., Coulter R., Zhao D., Jin Y.: 3D Printing of Biodegradable Polymer Vascular Stents: A Review. Chinese Journal of Mechanical Engineering: Additive Manufacturing Frontiers 1 (2022) 1-15.
- [16] Szustakiewicz K., Kryszak B., Dzienny P., Poźniak B., Tikhomirov M., Hoppe V., Szymczyk-Ziółkowska P., Tylus W., Grzymajło M., Gadomska-Gajadur A., Antończak A.J.: Cytotoxicity Study of UV-laser-irradiated PLLA Surfaces Subjected to Bio-ceramisation: A New Way towards Implant Surface Modification. International Journal of Molecular Sciences 22(16) (2021) 8436.
- [17] Amani S., Faraji G.: Processing and Properties of Biodegradable Magnesium Microtubes for Using as Vascular Stents: A Brief Review. Metals and Materials International 25 (2019) 1341-1359.
- [18] Waksman R., Pakala R., Baffour R., Seabron R., Hellinga D., Tio F.: Short-Term Effects of Biocorrodible Iron Stents in Porcine Coronary Arteries. Journal of Interventional Cardiology 21 (2008) 15-20.

- [19] Jiang J., Huang H., Niu J., Zhu D., Yuan G.: Fabrication and Characterization of Biodegradable Zn-Cu-Mn Alloy Micro-Tubes and Vascular Stents: Microstructure, Texture, Mechanical Properties and Corrosion Behavior. *Acta Biomaterialia* 151 (2022) 647-660.
- [20] Niu J., Tang Z., Huang H., Pei J., Zhang H., Yuan G., Ding W.: Research on a Zn-Cu Alloy as a Biodegradable Material for Potential Vascular Stents Application. *Materials Science and Engineering: C* 69 (2016) 407-413.
- [21] Wang J., Dou J., Wang Z., Hu C., Yu H., Chen C.: Research Progress of Biodegradable Magnesium-Based Biomedical Materials: A Review. *Journal of Alloys and Compounds* 923 (2022) 166377.
- [22] Mochizuki A., Kaneda H.: Study on the Blood Compatibility and Biodegradation Properties of Magnesium Alloys. *Materials Science and Engineering C* 47 (2015) 204-210.
- [23] Pan C., Zhao Y., Yang Y., Yang M., Hong Q., Yang Z., Zhang Q.: Immobilization of Bioactive Complex on the Surface of Magnesium Alloy Stent Material to Simultaneously Improve Anticorrosion, Hemocompatibility and Antibacterial Activities. *Colloids and Surfaces B: Biointerfaces* 199 (2021) 111541.
- [24] Wang Y., Chen L., Hou R., Bai L., Guan S.: Rapamycin-Loaded Nanocoating to Specially Modulate Smooth Muscle Cells on ZE21B Alloy for Vascular Stent Application. *Applied Surface Science* 615 (2023) 156410.
- [25] Saadatlou G. A., Ijaz A., Sipahiođlu D., Surme S., Kavakli I. H., Gurpinar Y., Yalcin O., Motallebzadeh A., Guner P.T.: Tetra-Functional Multilayer Coatings for Cardiovascular Stent Materials. *Colloids and Surfaces A: Physicochemical and Engineering Aspects* 670 (2023) 131571.
- [26] Li P., Li X., Cai W., Chen H., Chen H., Wang R., Zhao Y., Wang J., Huang N.: Phospholipid-Based Multifunctional Coating via Layer-by-Layer Self-Assembly for Biomedical Applications. *Materials Science and Engineering: C* 116 (2020) 111237.
- [27] Cheng W., Li C., Ma X., Yu L., Liu G.: Effect of SiO<sub>2</sub>-Doping on Photogenerated Cathodic Protection of Nano-TiO<sub>2</sub> Films on 304 Stainless Steel. *Materials & Design* 126 (2017) 155-161.
- [28] Sansone V., Pagani D., Melato M.: The Effects on Bone Cells of Metal Ions Released from Orthopaedic Implants. A Review. *Clinical Cases in Mineral and Bone Metabolism* 10 (2013) 34-40.
- [29] Zhu W., Su Z., Guo J., Li K., Chen K., Li W., Yi A., Liao Z., Luo Y., Hu Y., Xu Y., Lin Q., Meng X.: Preparation and Characterization of Diamond-like Carbon (DLC) Film on 316L Stainless Steel by Microwave Plasma Chemical Vapor Deposition (MPCVD). *Diamond and Related Materials* 122 (2022) 108820.
- [30] Malisz K., Świeczko-Żurek B., Sionkowska A.: Preparation and Characterization of Diamond-like Carbon Coatings for Biomedical Application - A Review. *Materials* 16 (2023) 3420.
- [31] Castellino M., Stolojan V., Virga A., Rovere M., Cabiale K., Galloni M.R., Tagliaferro A.: Chemo-Physical Characterisation and in Vivo Biocompatibility Assessment of DLC-Coated Coronary Stents. *Analytical and Bioanalytical Chemistry* 405 (2013) 321-329.
- [32] Saito T., Hasebe T., Yohena S., Matsuo Y., Kamijo A., Takahashi K., Suzuki T.: Antithrombogenicity of Fluorinated Diamond-like Carbon Films. *Diamond and Related Materials* 14 (2005) 1116-1119.
- [33] Nurdin N., François P., Mugnier Y., Krumeich J., Moret M., Aronsson B.-O., Descouts P.: Haemocompatibility Evaluation of DLC- and SiC-Coated Surfaces. *European cells & materials* 5 (2003) 17-18.
- [34] Pan C., Han Y., Lu J.: Structural Design of Vascular Stents: A Review. *Micromachines* 12 (2021) 1-26.
- [35] Zheng Y., Yang H.: *Manufacturing of Cardiovascular Stents. Metallic Biomaterials Processing and Medical Device Manufacturing*, Woodhead Publishing 2020.
- [36] Tammareddi S., Li Q.: Effects of Material on the Deployment of Coronary Stents. *Advanced Materials Research* 125 (2010) 315-318.
- [37] Lee P.-Y., Chen Y.-N., Hu J.-J., Chang C.-H.: Comparison of Mechanical Stability of Elastic Titanium, Nickel-Titanium, and Stainless Steel Nails Used in the Fixation of Diaphyseal Long Bone Fractures. *Materials (Basel)* 11 (2018) 2159.
- [38] Bucsek A.N., Paranjape H.M., Stebner A.P.: Myths and Truths of Nitinol Mechanics: Elasticity and Tension-Compression Asymmetry, Shape Memory and Superelasticity 2 (2016) 264-271.
- [39] Tanzi M.C., Farè S., Candiani G.: *Biomaterials and Applications. Foundations of Biomaterials Engineering*, Academic Press 2019.
- [40] Chen J., Tan L., Yu X., Etim I. P., Ibrahim M., Yang K.: Mechanical Properties of Magnesium Alloys for Medical Application: A Review. *Journal of the Mechanical Behavior of Biomedical Materials* 87 (2018) 68-79.
- [41] De Scheerder I., Sohler J., Wang K., Verbeken E., Zhou X.R., Froyen L., Van Humbeeck J., Piessens J., Van de Werf F.: Metallic Surface Treatment Using Electrochemical Polishing Decreases Thrombogenicity and Neointimal Hyperplasia of Coronary Stents. *Journal of Interventional Cardiology* 13 (2000) 179-185.
- [42] Zhao H., Van Humbeeck J., Sohler J., De Scheerder I.: Electrochemical Polishing of 316L Stainless Steel Slotted Tube Coronary Stents. *Journal of Materials Science: Materials in Medicine* 13 (2002) 911-916.
- [43] Muhammad N., Li L.: Underwater Femtosecond Laser Micromachining of Thin Nitinol Tubes for Medical Coronary Stent Manufacture. *Applied Physics A: Materials Science and Processing* 107 (2012) 849-861.
- [44] Chan Lee J., Hwan In S., Hee Park C., Sang Kim C.: Development of Multi-Layer Membrane Manufacturing Technology for Stent Coating Using Electrospinning Technology. *Materials Letters* 331 (2023) 133415.
- [45] Rickel A.P., Deng X., Engebretson D., Hong Z.: Electrospun Nanofiber Scaffold for Vascular Tissue Engineering. *Materials Science and Engineering: C* 129 (2021) 112373.
- [46] Feng Y., Chen Y., Chen Y., He X., Khan Y., Hu H., Lan P., Li Y., Wang X., Li G., Kaplan D.: Intestinal Stents: Structure, Functionalization and Advanced Engineering Innovation. *Biomaterials Advances* 137 (2022) 212810.
- [47] Chalony C., Erik Aguilar L., Hee Park C., Sang Kim C.: Drug Free Anti-Cell Proliferative and Anti-Platelet Adhesion Coating for Vascular Stents via Polymeric Electrospun Fibers. *Materials Letters* 291 (2021) 129545.
- [48] Siemiński P., Budzik G.: *Techniki Przyrostowe: Druk 3D. Drukarki 3D; Oficyna Wydawnicza, Politechnika Warszawska* (2015).
- [49] Lei Y., Chen X., Li Z., Zhang L., Sun W., Li L., Tang F.: A New Process for Customized Patient-Specific Aortic Stent Graft Using 3D Printing Technique. *Medical Engineering and Physics* 77 (2020) 80-87.
- [50] Okereke M.I., Khalaj R., Tabriz A.G., Douroumis D.: Development of 3D Printable Bioresorbable Coronary Artery Stents: A Virtual Testing Approach. *Mechanics of Materials* 163 (2021) 104092.

# POLYLACTIDE-BASED COMPOSITE MATERIALS FOR 3D PRINTING AND MEDICAL APPLICATIONS - THE EFFECT OF BASALT AND SILICON DIOXIDE ADDITION

MACIEJ PYZA<sup>1\*</sup>, NATALIA BRZEZIŃSKA<sup>1</sup>,  
KAROLINA KULIŃSKA<sup>2</sup>, JADWIGA GABOR,  
ADRIAN BARYLSKI<sup>1</sup>, KRZYSZTOF ANIOŁEK,  
ŻANETA GARCZYK-MUNDAŁA<sup>1</sup>, KAYODE ADEBESIN,  
ANDRZEJ SWINAREW<sup>1,2</sup>

<sup>1</sup> FACULTY OF SCIENCE AND TECHNOLOGY,  
UNIVERSITY OF SILESIA, 75 PUŁKU PIECHOTY 1A,  
41-500 CHORZÓW, POLAND

<sup>2</sup> INSTITUTE OF SPORT SCIENCE,  
THE JERZY KUKUCZKA ACADEMY OF PHYSICAL EDUCATION,  
MIKOŁOWSKA 72A, 40-065 KATOWICE, POLAND

\*E-MAIL: MACIEJ-PYZA@WP.PL

## Abstract

Polymers are compounds that play a key role in the development of many fields of science, including emergency medicine. Currently, there are increasing requirements for biomedical polymers in terms of producing lighter and more ecological equipment. To meet these requirements, a composite material was developed: polylactide (PLA) with the addition of modifiers - basalt and silicon dioxide (SiO<sub>2</sub>). PLA was chosen as a biodegradable polymer that naturally decomposes in the environment. This is very important, regarding a large number of single-use materials made of microplastics polluting the environment. The samples were made by additive 3D printing and then immersed in swimming pool water, chlorine solution, and distilled water. FTIR analysis showed the influence of the environment on the intensity and shift of PLA absorption bands. Microscopic analysis provided information on surface morphology, roughness, and potential defects. Tribological and micro-mechanical tests showed that the additions of basalt and silica to the PLA material influenced the morphological structure and the average area of the wear trace, volumetric wear, and average coefficient of friction. In the presence of chlorine solution, distilled water, and pool water under real conditions, the SiO<sub>2</sub> addition made the PLA material more resistant to abrasion, as compared to the basalt addition. However, additives did not significantly affect the PLA material hardness, and the samples with basalt turned out to be more resistant to deformation.

**Keywords:** polylactide, 3D printing, polymer, basalt, SiO<sub>2</sub>

[Engineering of Biomaterials 166 (2022) 29-39]

doi:10.34821/eng.biomat.166.2022.29-39

Submitted: 2023-01-25, Accepted: 2023-02-22, Published: 2023-02-28



Copyright © 2022 by the authors. Some rights reserved.  
Except otherwise noted, this work is licensed under  
<https://creativecommons.org/licenses/by/4.0>

## Introduction

Polymers are a group of compounds that are being increasingly applied in many fields. In medicine, polymers are used to produce medical devices for reconstructive surgery, cardiac surgery, transplantology, or dentistry. In addition, polymers are also successfully employed in emergency medicine and water rescue. The polymer design offers better, more ergonomic, lighter, and eco-friendlier equipment necessary to save human lives. However, the materials developed for this solution must have suitable mechanical properties as compared to traditional materials. Applications of polymers contribute to the medical market as well as to the field of additive technologies [1]. One of such materials is polylactide (PLA), i.e. an aliphatic linear polyester made of α-hydroxy acids (FIG. 1).

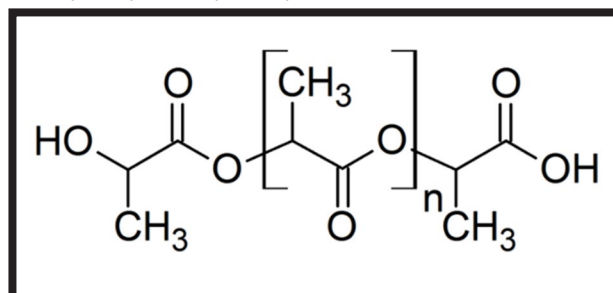


FIG. 1. PLA structural scheme.

PLA is a biodegradable, thermoplastic polyester formed in the process of polymerization of lactic acid. It is obtained as a result of the fermentation of sugars from carbohydrate sources, such as corn or sugar cane [2]. It can be produced with a capacity of more than 140,000 tons per year on a global scale, making it easily available and relatively cheap. It is one of the most promising biopolymers due to the low greenhouse gases emission and the small amount of energy used for its production [3]. PLA belongs to polyesters which are the most versatile biodegradable materials due to the presence of bonds susceptible to attack by hydrolytic enzymes in their main chain [4]. In the pharmaceutical industry, PLA is used as a carrier of active substances, and in medicine for the regeneration of damaged tissues. PLA is also increasingly found in areas such as textiles and the packaging industry. The wide variety of applications results from its good mechanical properties, i.e. tensile strength, Young's modulus, and flexural strength. Additionally, the beneficial physical and chemical properties of PLA, as well as its biocompatibility, make it applicable for drug delivery systems, medicinal products, surgical implants, orthopaedic devices, and bioresorbable scaffolds for tissue engineering [5]. However, PLA has low rate of crystallization, low strength and heat resistance that are limiting factors for its long-term use.

Additives such as mineral fibers or natural organic compounds make it possible to modify the PLA properties, including mechanical strength, chemical resistance, or plasticity. For instance, basalt fibers are 100% natural and thus environmentally friendly. They are made of igneous rocks and are non-toxic. They have high temperature resistance, chemical resistance, and mechanical properties, such as abrasion resistance [6]. Basalt is characterized by high hardness, corrosion resistance, as well as high thermal and chemical stability [7]. Such additives in the PLA material can increase its applications in various fields due to improved properties.

Taking into account the properties of the selected polymer matrix and its modifiers, such as  $\text{SiO}_2$  and basalt, the plan was to obtain the material for printing by extrusion in the appropriate temperature regime. The research aimed to evaluate the properties of PLA enhanced with silica and basalt and to determine its potential applications. The samples were immersed in chlorine solution, swimming pool water, and distilled water to examine the material applicability in water and medical rescue. For this purpose, the FTIR analysis was carried out to identify changes in the chemical structure of the modified material, and the tribological analysis to assess their impact on the material wear resistance. Micromechanical testing determined the effect of additives on the micromechanical properties of the material, i.e., hardness, fracture toughness and elasticity modulus. The confocal microscopy examination visualized the material structure, its surface properties and the morphological structure changes.

The use of PLA/basalt, PLA/ $\text{SiO}_2$  composites and the 3D printing technology provided an opportunity to develop an innovative project - an ultra-light and universal rescue board for use in water and medical rescue. Its characteristic feature is the profiled bottom distinguished by the presence of fins based on the utility model no. 67456 [8]. Such a design increases the buoyancy of the equipment and improves its efficiency in water rescue. One variant of the device assumed a "honeycomb"-type HDPE filling in the ratio of 20% full to 80% empty volume. In the research, it was decided to replace the material with the modified PLA to reduce the total weight of the device without a significant loss of strength.

## Materials and Methods

In order to obtain PLA/basalt and PLA/ $\text{SiO}_2$  composite materials, the fibers were shortened via pulverization. Each fiber of 9 g in weight was placed in the sample chamber of the Pulverizer. The rotation speed was set to 350, the repetition 47 with the timer set to 15 min for each repetition. Mixing was performed with a self-made mixer in order to homogenize the matrix and the reinforcement. For adhesive purposes, polyol was used as a homogenizing agent. The composites were vacuum dried at  $55^\circ\text{C}$ , under a pressure of 760 mmHg for 6 h. The extrusion took place in the temperature regime with the set appropriate parameters. The temperature parameters for the PLA/ $\text{SiO}_2$  composite were  $230^\circ$ ,  $220^\circ$ ,  $212^\circ$  and  $199^\circ$ , respectively. For the PLA/basalt composite, they were  $235^\circ$ ,  $225^\circ$ ,  $215^\circ$  and  $204^\circ$  for the single-screw extruder with  $L/d = 32/1$ .

Basalt is a volcanic material with ceramic properties. As a modifier, it enhances mechanical strength, wear resistance, and thermal stability in the 3D printed objects. On the other hand,  $\text{SiO}_2$  is a well-known ceramic material with high hardness and wear resistance. Its presence in the composite improves the mechanical and thermal properties of the 3D printed models. PLA in the form of granules and modifiers were liquefied in a continuous process. Thanks to the use of a linear head and the synchronization of the pick-up tape, a filament with a diameter of 1.75 mm was obtained.

The first step of the 3D printing process was the preparation of spatial models using CAD software - SolidWorks. Then, thanks to the Slic3r program, they were converted into a "g-code" file, ready for use on a 3D printer. The Urbicum DX device with a working area of 305 (X) x 305 (Y) x 380 mm (Z) was employed. The set temperature parameters were  $80^\circ\text{C}$  for the worktable and  $200\text{-}210^\circ\text{C}$  for the head. For proper printing and better adhesion to the build plate, the temperatures were increased for PLA/ $\text{SiO}_2$  and PLA/basalt by about  $20^\circ\text{C}$ , as compared to the pure PLA. The printing speed in the additive technology was set at 60 mm/s for the 4 inner layers and 50 mm/s for the two top layers and the two bottom layers. The average layer thickness was 0.2-0.3 mm. The "solid" type filling was used, i.e. 100%. There was no need for supports for the models. The resulting 3D printed samples were cuboid with the dimensions 50 x 50 x 10 mm (FIG. 2).

The preliminary research stage was the samples immersion in distilled water, swimming pool water, and a solution of sodium dichloroisocyanurate in distilled water (FIG. 3) for 7 days. The dissolutions ratio was 5 mg  $\text{Cl}_2$  (1 tablet 8.5 mg of sodium dichloroisocyanurate containing 5 mg  $\text{Cl}_2$ ) / 1 l  $\text{H}_2\text{O}$  (chlorine solution). The samples were drilled with a bench drill to a diameter of between 2 and 10 mm and threaded. The reference sample was the PLA material immersed in the same substances and with the same parameters as the samples containing PLA/basalt and PLA/ $\text{SiO}_2$ .

The next step was drying carried out using the DZ-3BC dryer with a power of 2000 W. It was conducted at  $50^\circ\text{C}$  for two hours under vacuum conditions.

The FTIR (Fourier Transform Infrared Spectroscopy) spectroscopy was carried out to evaluate the chemical composition and the molecular structure of the obtained samples. The tests were performed on the FTIR spectrophotometer - IRTracer-100, equipped with the ATR accessory (attenuated total reflectance). The measurements were made at 100 scans per sample.

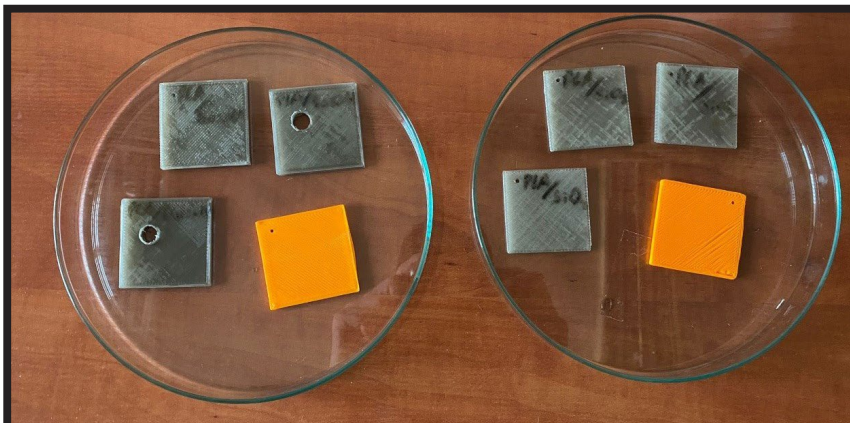


FIG. 2. Prepared test samples.

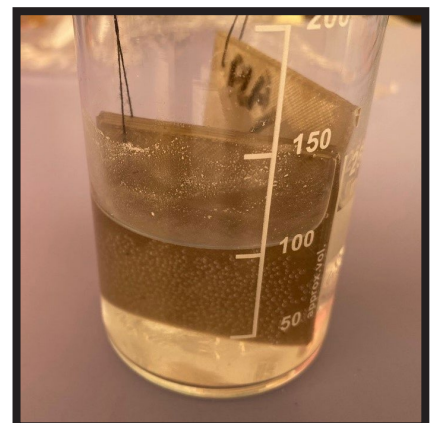


FIG. 3. An example of immersing a sample in a chlorine solution.

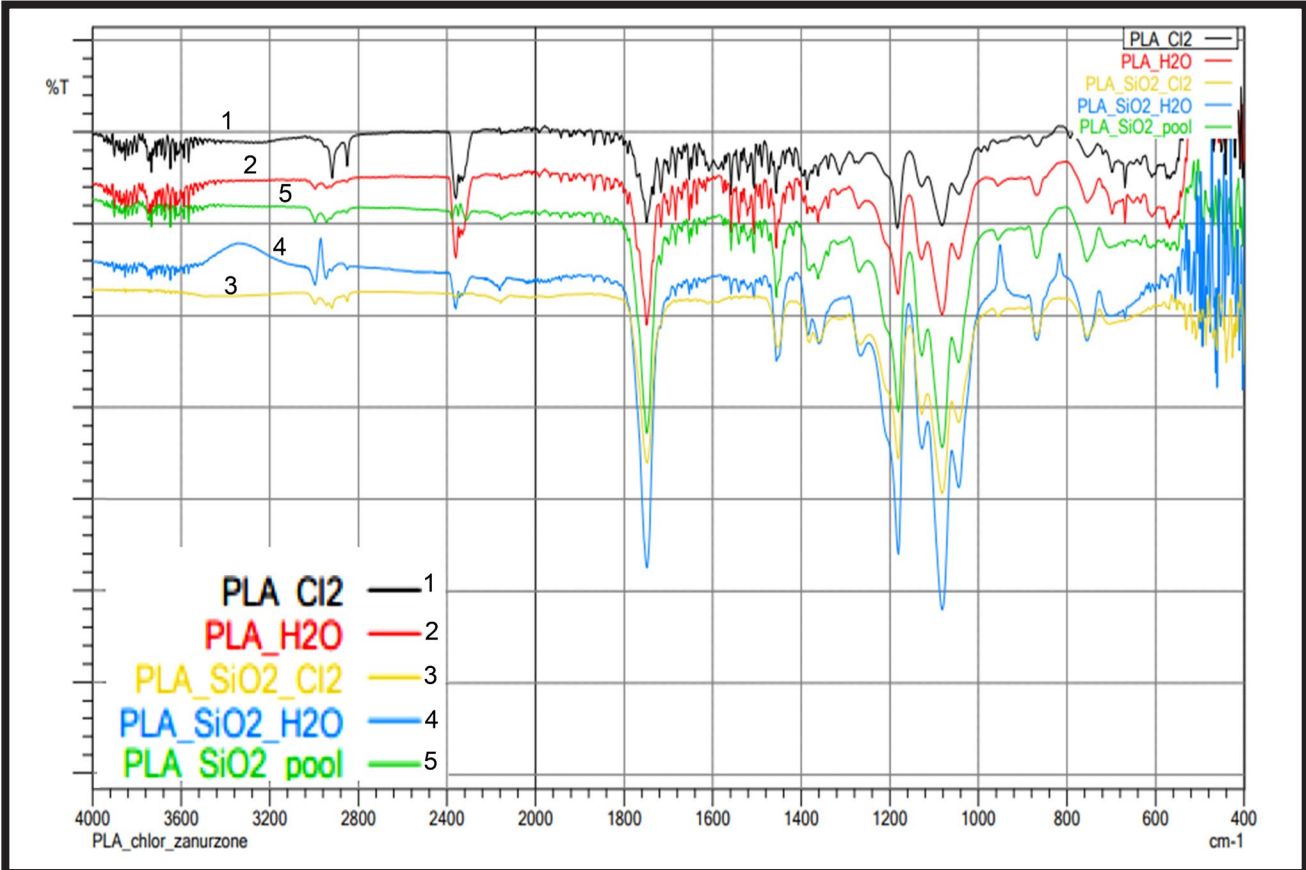


FIG. 4. Spectrum obtained for the PLA/SiO<sub>2</sub> sample immersed in chlorine solution, H<sub>2</sub>O and pool water in relation to the PLA reference sample immersed in chlorine solution and H<sub>2</sub>O.

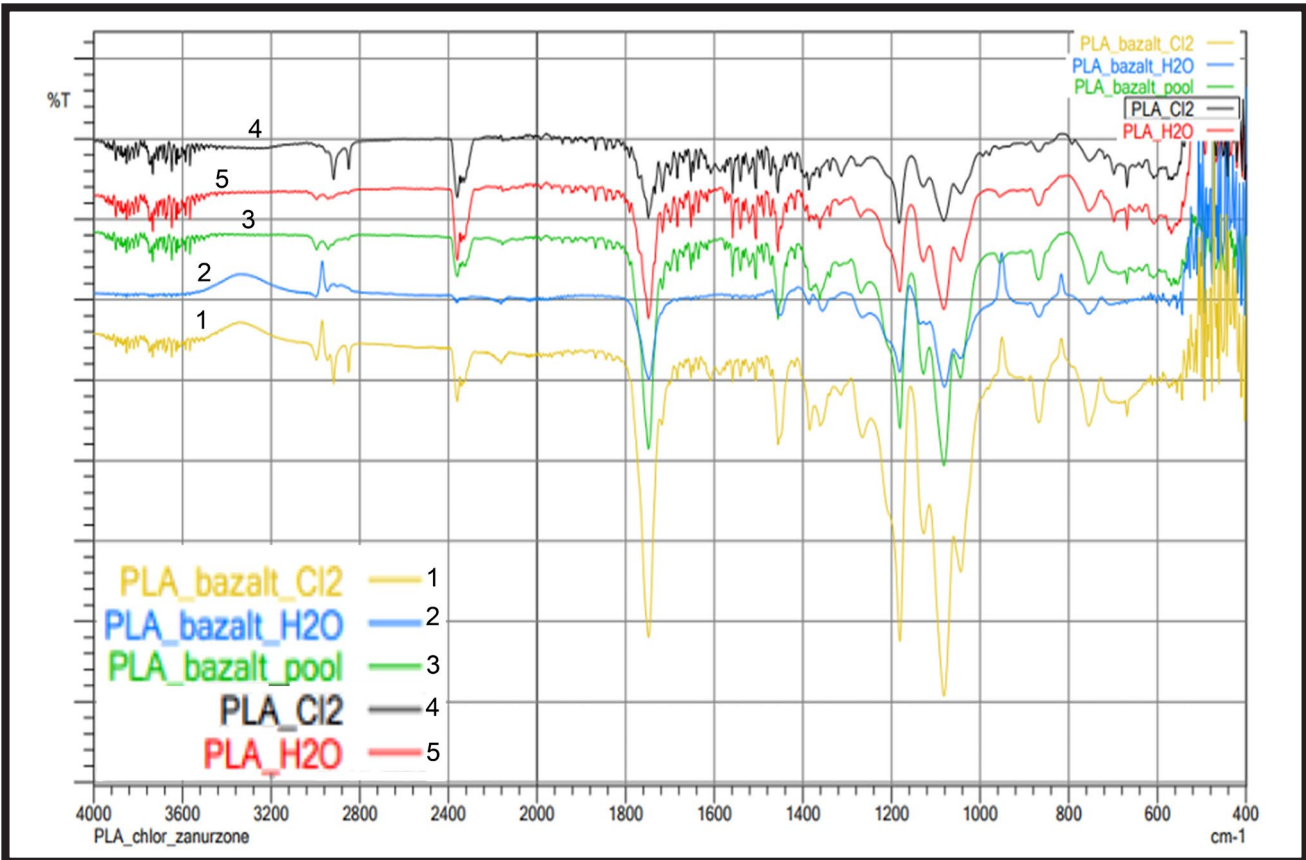


FIG. 5. Spectrum obtained for the PLA/basalt sample immersed in chlorine solution, H<sub>2</sub>O and pool water in relation to the PLA reference sample immersed in chlorine solution and H<sub>2</sub>O.

The LEXT OLS4000 scanning confocal microscope was used to obtain microscopic images. The surface images were analyzed using the MountainsMap® Premium software.

The material evaluation in terms of friction, wear resistance, and friction coefficient was performed via tribological tests. The dimensions of the samples were adjusted to 25 x 25 x 1 mm and then ground to remove the excess material. This was achieved by dry grounding edges with silicon carbide sandpaper with grits of P820 and P600. Tribological tests were performed using the ball-on-disc friction junction on the Anton-Paar device (Tribometer - TRN, Corcelles-Cormondèche, Switzerland). Steel bearing balls (100Cr6) with a diameter of 6 mm were used as counter samples. The tests were carried out in conditions of the technically dry friction in a reciprocating linear motion. The pressure force in the friction node was  $F_N = 20$  N, the friction distance amplitude  $L = 10$  mm, the frequency  $f = 3.18$  Hz, and the number of cycles 1250 (friction distance  $s = 25$  m). The average wear trace area  $P$  was determined using the SurfTest SJ-500 profilographometer (Mitutoyo, Tokyo, Japan). The volumetric wear  $V_w$  was determined according to the formula:

$$V_w = \frac{V}{F_N \cdot s} \left[ \frac{\text{mm}^3}{\text{Nm}} \right]$$

where:  $F_N$  – load [N],  $s$  – friction distance [m],  $V$  – volume of the wear trace calculated for linear reciprocating motion from the formula  $V = P \cdot L$  [mm<sup>3</sup>],  $P$  – average wear trace area [mm<sup>2</sup>],  $L$  – friction distance amplitude [mm] [9,10]

Micromechanical tests were performed with the Micro Combi Tester - MCT3 device (Anton Paar, Corcelles-Cormondèche, Switzerland). The Berkovich diamond indenter (B-V 83) was used, with a maximum load of 100 mN (0.1 N). The load-unload of the indenter was performed at a speed of 200 mN/min, the holding time under a maximum load was 10 s. For each sample, 5 indentations were made. The hardness HIT and elasticity modulus EIT were determined using the Oliver-Pharr method [11]. The measurements stayed in accordance with the ISO 14577 standard [12]. On the basis of the recorded load-unload curves, the values of the total indentation work  $W_{\text{tot}}$  and its components (plastic indentation work  $W_{\text{pl}}$  and elastic indentation work  $W_{\text{el}}$ ) were determined. The percentage of elastic recovery work  $\eta_{\text{IT}}$  was also established.

## Results and Discussions

According to preliminary studies, the composite material, i.e. PLA with the addition of basalt and silica, underwent a plastic deformation due to a force causing its flow through the matrix. This material adopted the cross-sectional profile of the matrix. Thanks to the appropriate properties, the fiber shape was retained in the final phase of extrusion.

The FTIR infrared spectroscopy was carried out to determine the chemical composition of the tested samples. The examination of the characteristic bands for functional groups allowed the identification of the chemical components of the material and the changes in its chemical structure. In general, these changes are caused by the immersion in water-based environments, which may affect mechanical properties. After placing the properly prepared samples in the FTIR equipment, the following results were obtained and compared to evaluate possible differences (FIGS 4 and 5).

In the FTIR analysis of the samples, the characteristic two bands are: the absorption one of the hydroxyl group (-OH) around 3600-3200 cm<sup>-1</sup>, present in the lactic acid, and the band of the aromatic group around 1600-3200 cm<sup>-1</sup>. The absorption bands present in the PLA sample are the methyl group (-CH<sub>3</sub>) 3000-2800 cm<sup>-1</sup>, the carbonyl group (C=O) 1750-1700 cm<sup>-1</sup>, the methylene group (-CH<sub>2</sub>-) 1450-1350 cm<sup>-1</sup>, group C-O 1300-1200 cm<sup>-1</sup> and C-O-C 1150-1050 cm<sup>-1</sup>. Each absorption band in the FTIR spectrum corresponds to the absorption of energy by a specific functional group, which allows to identify its presence and amount in the material [13]. Analyzing the above graphs, in the plain PLA (PLA\_Cl<sub>2</sub>, PLA\_H<sub>2</sub>O) a characteristic absorption band associated with ester carbonyl groups and CH<sub>3</sub> groups can be observed. Banding is typical and it appears as narrow peaks. There is also a characteristic band shift in the case of PLA\_H<sub>2</sub>O, which may be due to the water moisture.

Basalt and SiO<sub>2</sub> modifiers affected the characteristic absorption bands exhibited by PLA for carbonyl ester groups and methyl groups. The basalt presence made the bands shift slightly, while the addition of SiO<sub>2</sub> affected their intensity and shape. The characteristic absorption bands for silica are in the range of 1050-1200 cm<sup>-1</sup> and the absorption bands for Si-O-Si groups are in the range of 1000-1200 cm<sup>-1</sup>, while for basalt and minerals contained in it - silica and oxides are in the range of 1050-1200 cm<sup>-1</sup> and 400-900 cm<sup>-1</sup>, respectively [14,15].

The shape, intensity, and shift can be influenced by the samples immersion in water, chlorine solution, or pool water. Water affects the PLA chemical structure through hydrolysis of ester bonds, which leads to the polymer decomposition, and thus to its strength decrease [16]. The same applies to Cl<sub>2</sub> which can react with the PLA functional groups. This reaction also leads to changes in the absorption bands characteristic for these groups, via hydrolysis and the reaction with chlorine compounds [17]. Pool water has a similar effect due to chlorine. Changes in these bands indicate the chemical structure alterations and thus the changes in mechanical properties. In the analyzed samples, the absorption bands did not undergo significant shifts, nor did their shape and intensity change. However, this may change in a long-term study, hence, it needs further tests.

The examination using the LEXT OLS4000 confocal microscope produced the 3D images of the sample structures to determine the surface morphology, roughness, and potential defects that may occur in the printed samples. Their surface structure was also compared depending on the basalt/SiO<sub>2</sub> modifier present in the PLA material and after immersing the samples in solutions. The images were taken at different magnifications for a more detailed analysis (20x, 50x).

FIGS 6a and 7a show the microscopic images of the PLA material - a reference sample soaked in H<sub>2</sub>O. This material has noticeable characteristics that can be attributed to impurities or variations in its properties caused by the extrusion process. The surface is rough and irregular. The ribbed structure may result from the movement of the printhead during the extrusion and cooling process, and it may be also affected by heat retention in the sample.

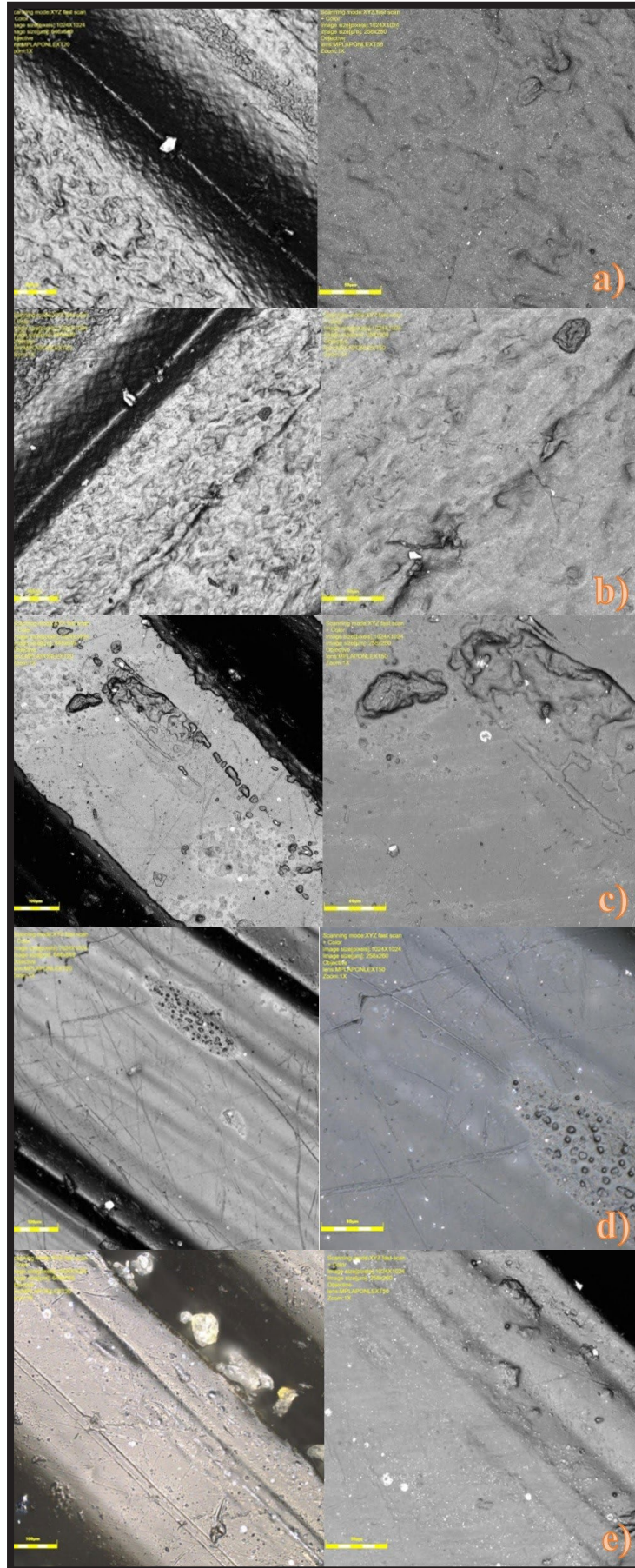


FIG. 6. Confocal microscope images of a reference sample of PLA material after tribological testing immersed in: a)  $\text{Cl}_2$ , b)  $\text{H}_2\text{O}$  in relation to PLA material with the addition of basalt immersed in: c)  $\text{Cl}_2$ , d)  $\text{H}_2\text{O}$ , e) swimming pool water.

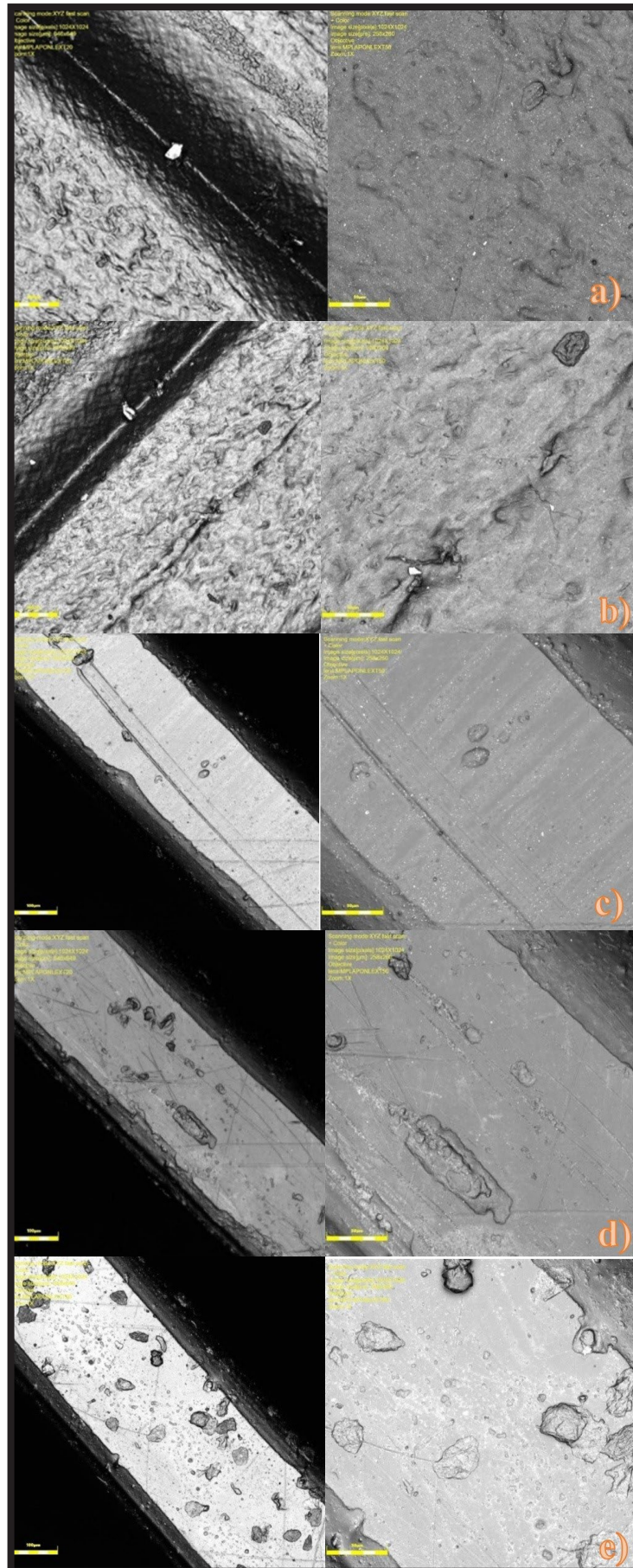


FIG. 7. Confocal microscope images of a reference sample of PLA material after tribological testing immersed in: a)  $\text{Cl}_2$ , b)  $\text{H}_2\text{O}$  in relation to PLA material with the addition of  $\text{SiO}_2$  immersed in: c)  $\text{Cl}_2$ , d)  $\text{H}_2\text{O}$ , e) swimming pool water.

Additionally, the PLA surface morphology can be impacted by processing conditions, such as temperature, cooling rate, and pressure. The PLA material is hydrophilic, so it can easily absorb moisture from the environment, including water. Being soaked in H<sub>2</sub>O, PLA can swell and soften, which leads to a decrease in its mechanical strength and stiffness [17, 18]. The degree of swelling and changes in the PLA properties depend on the duration, temperature, and pH of the water. Soaking the samples for 7 days did not cause significant changes in the morphological structure of the material. On the contrary, wetting PLA in a chlorine solution can lead to its dissolution and degradation. Chlorine is a strong oxidant and can react with ester groups in the PLA polymer chains, which leads to acid hydrolysate and polymer decomposition [16, 19].

The result of wetting PLA in chlorine dilution depends on the duration and concentration of the solution. In the images from the confocal microscope (FIGs 6b and 7b), one can observe the surface morphology after 7 days of soaking the material in free chlorine. The surface roughness increased. The shape was more irregular and the structure was rougher. It proves that chlorine affects the morphological properties of PLA, thus changing its mechanical properties. In turn, the PLA behavior in pool water shows its susceptibility to hydrolysis, which is a chemical reaction that occurs when water molecules break down the polymer chains in the material. This can reduce the material mechanical strength and other physical properties over time [20]. However, if the PLA material is properly reinforced and protected from the effects of H<sub>2</sub>O and chlorine solution, it can retain its strength and shape. The PLA enriched with modifiers such as basalt and SiO<sub>2</sub> increases its resistance to various environments.

Analyzing the above confocal microscope images, it can be seen that the surface of PLA with the addition of basalt (FIGs 6c, d, e) is rougher than the surface with SiO<sub>2</sub> (FIGs 7c, d, e). The reason lies in the nature of basalt, as it is a volcanic mineral with a rougher surface than silica [6]. These differences can affect surface properties, such as adhesion and wettability. The addition of SiO<sub>2</sub> also supports a regular distribution of grains on the PLA surface, which can affect mechanical properties, such as stiffness and tensile strength. In the presence of basalt, there is a more random distribution of grains on the surface, which affects the mechanical properties. The addition of SiO<sub>2</sub> or basalt may influence the PLA structure. In the presence of silica (FIGs 7c, d, e), a more even and regular fibers distribution is visible in the entire structure of the PLA material. On the other hand, the basalt addition results in an irregular structure with protrusions of irregular shapes (FIGs 6c,d,e).

The study using the ball-disk friction node on the Anton-Paar device (Tribometer - TRN, Corcelles-Cormondrèche, Switzerland) and a profilographometer provided information on the mechanical properties of PLA, PLA/basalt and PLA/SiO<sub>2</sub> samples. This study also assessed the properties changes after the samples were immersed in pool water, chlorine solution, and distilled water for 7 days. The parameters such as: average coefficient of friction (FIG. 8), average area of the wear trace (FIG. 9) and volumetric wear (FIG. 10) were determined. The results are presented in the form of graphs.

FIG. 8 shows the average coefficient of friction for the tested samples. The higher the friction coefficient, the greater the friction force that occurs between the two surfaces [21]. Based on the given graph, it is possible to compare the resistance of each sample and identify the samples with greater resistance to friction. The PLA\_Cl<sub>2</sub> sample has the lowest average friction coefficient ( $\mu = 0.301$ ), which proves its higher resistance to friction as compared to the other samples. On the other hand, the PLA\_H<sub>2</sub>O sample has a higher average friction coefficient ( $\mu = 0.443$ ), which suggests its lower friction resistance compared to the PLA\_Cl<sub>2</sub> sample. The highest average coefficient of friction is 0.486 for the PLA\_SiO<sub>2</sub>\_Cl<sub>2</sub> sample. Thus, this sample is the least resistant to wear in contact with chlorinated substances, compared to the other samples containing an admixture of SiO<sub>2</sub> or basalt. FIG. 9 represents the Area Wear Track obtained during the tribological test. The values differ significantly between individual samples, which means that the presence of the modifier and immersion of the material in the solutions had a significant impact on their wear.

The smaller the average area of the wear trace, the greater the wear resistance and durability of the material [21]. It can also be concluded that PLA in contact with water has the highest average wear trace area (714750  $\mu\text{m}^2$ ), so this material is the least resistant to abrasion compared to the other tested samples. The PLA\_basalt\_H<sub>2</sub>O sample has a lower value (126500  $\mu\text{m}^2$ ) than the PLA\_SiO<sub>2</sub>\_H<sub>2</sub>O one with the average of 132250  $\mu\text{m}^2$ , which proves its better wear resistance. Among the samples in contact with chlorine, the PLA\_basalt\_Cl<sub>2</sub> one revealed the highest average surface of the wear trace (474,750  $\mu\text{m}^2$ ). The PLA\_SiO<sub>2</sub>\_Cl<sub>2</sub> obtained the lower wear surface value (113925  $\mu\text{m}^2$ ) than PLA\_Cl<sub>2</sub> (169000  $\mu\text{m}^2$ ). It can be concluded that the PLA\_basalt\_Cl<sub>2</sub> is the least resistant to abrasion in contact with chlorine chemicals. Summing up, as compared to basalt, SiO<sub>2</sub> is a better modifier of PLA matrix in terms of abrasion resistance, in the presence of chlorine, water, or pool water which usually reduce this resistance. Analyzing the volumetric wear results in FIG. 10, the smallest wear occurred in the PLA\_basalt\_H<sub>2</sub>O ( $2.531 \cdot 10^{-3} \text{ mm}^3/\text{Nm}$ ) sample, i.e. during the water test. On the other hand, a higher consumption was observed in the PLA\_H<sub>2</sub>O sample ( $1.43 \cdot 10^{-2} \text{ mm}^3/\text{Nm}$ ) but this value was several times higher than in the other samples. Comparing the results for each sample, the presence of chlorine in the environment reduced the volume consumption in the samples: PLA\_basalt\_Cl<sub>2</sub> ( $9.498 \cdot 10^{-3} \text{ mm}^3/\text{Nm}$ ), PLA\_SiO<sub>2</sub>\_Cl<sub>2</sub> ( $2.279 \cdot 10^{-3} \text{ mm}^3/\text{Nm}$ ) and PLA\_Cl<sub>2</sub> ( $3.381 \cdot 10^{-3} \text{ mm}^3/\text{Nm}$ ), as compared to the samples without chlorine. However, in the PLA\_basalt\_pool sample, the presence of pool water significantly increased the volume consumption ( $1.324 \cdot 10^{-2} \text{ mm}^3/\text{Nm}$ ), compared to the PLA\_SiO<sub>2</sub>\_pool sample ( $2.511 \cdot 10^{-3} \text{ mm}^3/\text{Nm}$ ). It is also worth mentioning that the smallest standard deviation (the smallest variability of the results) was revealed by the PLA\_basalt\_H<sub>2</sub>O sample ( $7.026 \cdot 10^{-5} \text{ mm}^3/\text{Nm}$ ).

The micromechanical tests using the Micro Combi Tester MCT3 device, determined the hardness and elasticity modulus of the samples - parameters important when choosing the right materials for medical applications and 3D printing. Thanks to the indentation (cavities), the load-unload curves (FIGs 11 and 12) were recorded for each sample to obtain information about the hardness and other mechanical properties. The following parameters were calculated: the Young's instrumental modulus, instrumental hardness, work of elastic and plastic deformation, total indentation work, maximum indentation depth, and elastic component of indentation work.

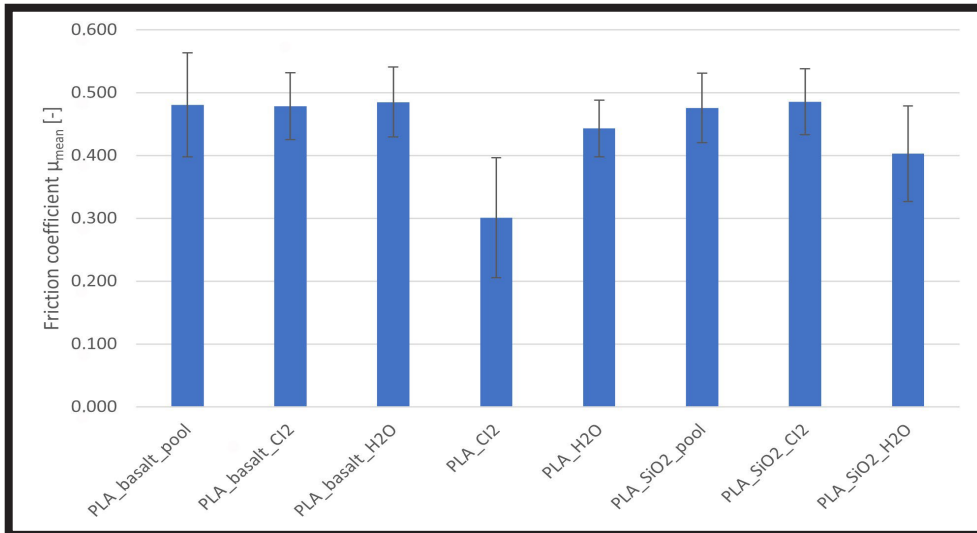


FIG. 8. Average friction coefficient.

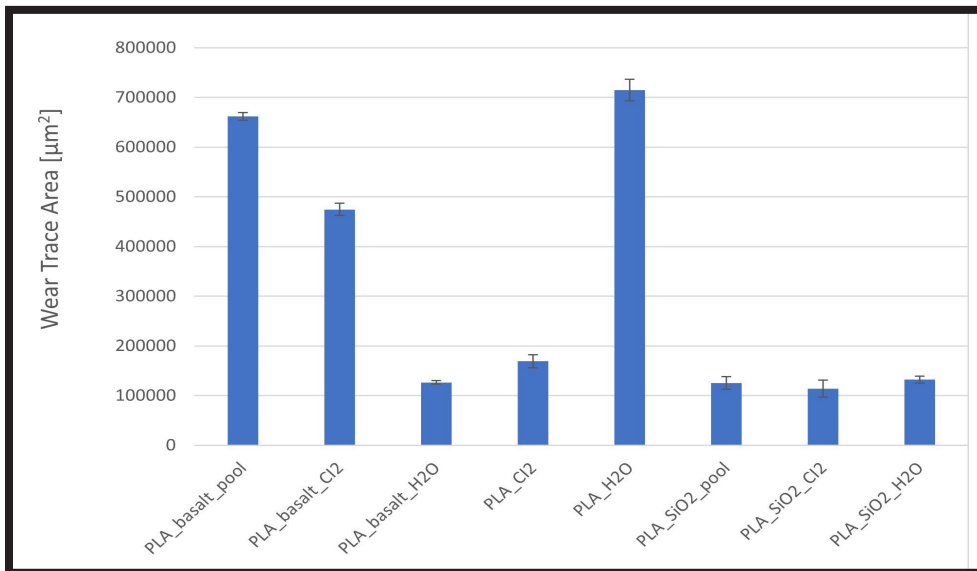


FIG. 9. Average wear trace area.

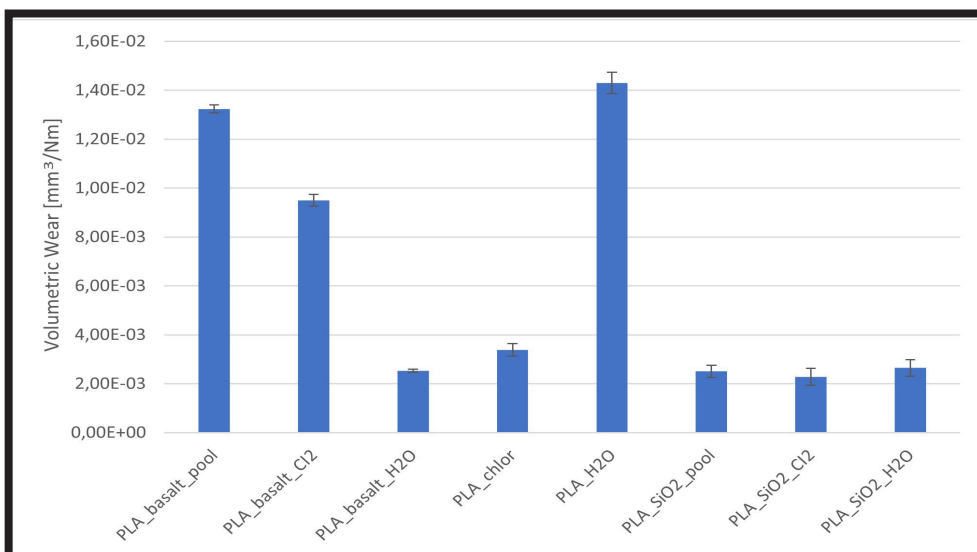


FIG. 10. Volumetric wear.

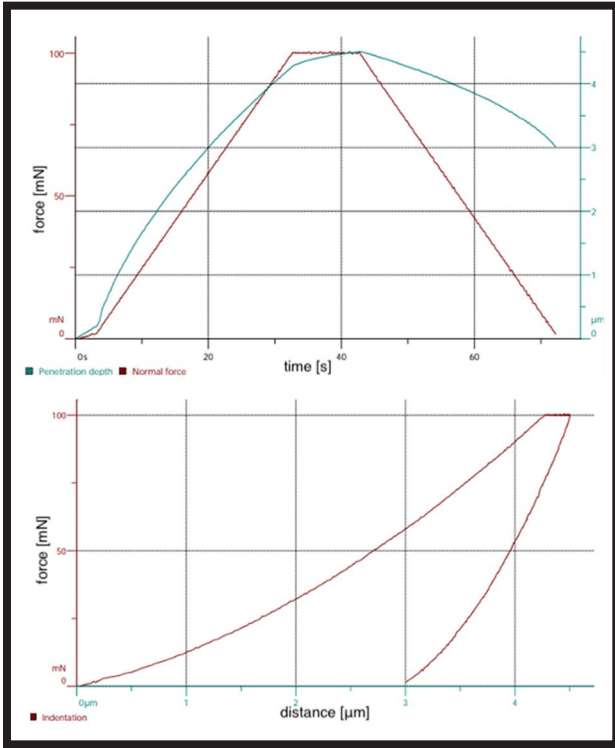


FIG. 11. Example of load-unload curves after indentation for PLA\_SiO<sub>2</sub>\_pool samples.

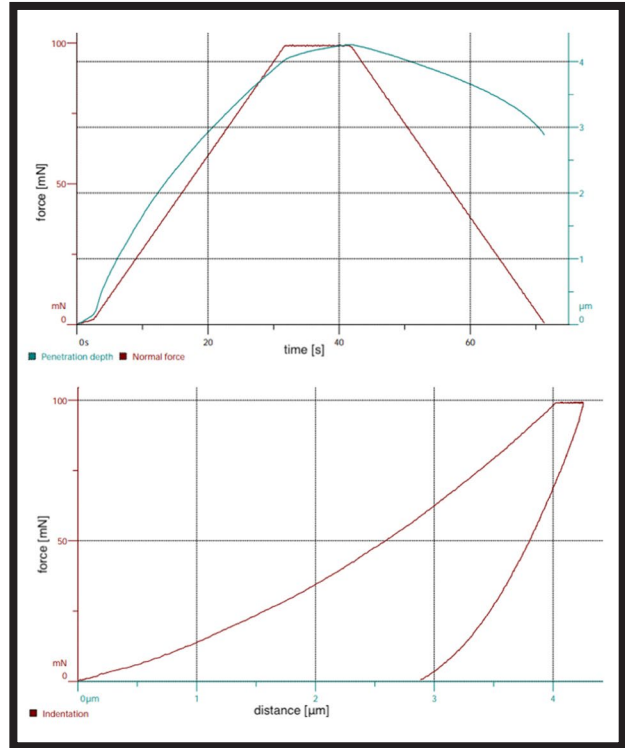


FIG. 12. Example of load-unload curves after indentation for PLA\_basalt\_Cl<sub>2</sub> samples.

TABLE 1. Results of micromechanical test samples,  $E_{IT}$  - indentation modulus of elasticity,  $H_{IT}$  – hardness,  $W_{el}$  – elastic forces,  $W_{pl}$  - plastic forces,  $W_{tot}$  – total forces,  $H_{max}$  - maximum indentation depth,  $\eta_{IT}$  - elastic component of indentation work.

Name	$E_{IT}$ [GPa]	$H_{IT}$ [MPa]	$W_{el}$ [MJ]	$W_{pl}$ [MJ]	$W_{tot}$ [MJ]	$H_{max}$ [Mm]	$\eta_{IT}$ [%]
PLA_BASALT_POOL	5.488	0.323	0.051	0.127	0.177	4.067	28.652
	0.114	0.008	0.002	0.004	0.006	0.029	0.424
PLA_BASALT_Cl <sub>2</sub>	5.366	0.293	0.052	0.13	0.181	4.254	28.51
	0.078	0.003	0.001	0.001	0.001	0.018	0.495
PLA_BASALT_H <sub>2</sub> O	3.192	0.249	0.075	0.135	0.209	4.911	35.594
	0.059	0.009	0.002	0.002	0.004	0.057	0.315
PLA_Cl <sub>2</sub>	5.661	0.310	0.049	0.131	0.18	4.099	27.608
	0.11	0.022	0.003	0.018	0.015	0.047	3.788
PLA_H <sub>2</sub> O	5.918	0.336	0.051	0.117	0.168	4.02	30.394
	0.498	0.035	0.002	0.011	0.012	0.159	1.761
PLA_SiO <sub>2</sub> _POOL	4.23	0.27	0.061	0.133	0.194	4.535	31.436
	0.1	0.005	0.002	0.001	0.003	0.03	0.481
PLA_SiO <sub>2</sub> _Cl <sub>2</sub>	3.885	0.264	0.065	0.134	0.199	4.636	32.603
	0.116	0.006	0.001	0.003	0.003	0.048	0.735
PLA_SiO <sub>2</sub> _H <sub>2</sub> O	3.079	0.247	0.075	0.139	0.214	4.94	35.144
	0.11	0.015	0.001	0.002	0.004	0.1	0.107

TABLE 1 presents results of the indentation modulus of elasticity ( $E_{IT}$ ) for the tested samples. The  $E_{IT}$  values indicate the material stiffness, i.e. its ability to resist deformation. The higher the  $E_{IT}$  value, the stiffer the material. The PLA\_BASALT\_pool and PLA\_BASALT\_Cl<sub>2</sub> revealed the  $E_{IT}$  values of 5.488 and 5.366 GPa, respectively. Both results were quite similar, suggesting that the chlorine solution immersion did not significantly affect the  $E_{IT}$  value. Therefore, basalt as a modifier in the material proved to be relatively stiff. The PLA\_Cl<sub>2</sub> samples immersed in chlorine solution and the PLA\_H<sub>2</sub>O samples in distilled water revealed their  $E_{IT}$  values to be 5.661 and 5.918 GPa, respectively. Both results were quite high, suggesting that the presence of chlorine and water positively effect the material stiffness. The PLA\_SiO<sub>2</sub>\_pool, PLA\_SiO<sub>2</sub>\_Cl<sub>2</sub> and PLA\_SiO<sub>2</sub>\_H<sub>2</sub>O containing silica had the  $E_{IT}$  values amounting to 4.23, 3.885 and 3.079 GPa, respectively. Compared to the results for basalt and chlorine, these values were lower, indicating that silica is less rigid than basalt. The highest instrumental hardness value was obtained for the PLA\_H<sub>2</sub>O sample, and the lowest for PLA\_SiO<sub>2</sub>\_H<sub>2</sub>O. It is worth noting that the samples immersed in chlorine dilution (PLA\_basalt\_Cl<sub>2</sub> and PLA\_SiO<sub>2</sub>\_Cl<sub>2</sub>) had lower hardness than the samples immersed in pool water (PLA\_basalt\_pool and PLA\_SiO<sub>2</sub>\_pool). Similarly, the PLA\_basalt\_H<sub>2</sub>O sample had a lower hardness than the PLA\_basalt\_pool sample after immersion in the respective environment. Analyzing the results, it can be seen that the samples containing additives (basalt, chlorine, SiO<sub>2</sub>) showed  $H_{IT}$  values comparable to the samples without additives (PLA\_H<sub>2</sub>O, PLA\_Cl<sub>2</sub>). In conclusion, the additives did not significantly affect the hardness of the PLA material.

The test results also showed the values of elastic forces ( $W_{el}$ ), plastic forces ( $W_{pl}$ ), and total forces ( $W_{tot}$ ). Compared to the reference samples (without modifiers), the PLA samples with basalt showed the higher elastic force, which means that the material was more resistant to deformation. At the same time, it was less plastic (lower plastic force). The samples after immersion in chlorine dilution and H<sub>2</sub>O showed a lower value of elastic and plastic force than the control samples. The addition of SiO<sub>2</sub> lowered the elastic and total force, but the plastic force value was close to the one of the control samples. These results suggest that the basalt addition can improve the PLA mechanical strength but at the expense of its ductility, while the immersion in chlorine dilution and H<sub>2</sub>O can weaken the mechanical strength. The SiO<sub>2</sub> addition can negatively affect the elastic and total strength, but it minimally influences the plastic strength.

Analyzing the results of the maximum indentation depth ( $H_{max}$ ), the PLA with basalt and the PLA with SiO<sub>2</sub> reached the highest  $H_{max}$  (4.067  $\mu$ m and 4.535  $\mu$ m, respectively). This means that these additives in the material increased its resistance to deformation. The PLA samples after immersion in H<sub>2</sub>O and chlorine dilution reached the lowest  $H_{max}$  values (4.02  $\mu$ m and 4.099  $\mu$ m, respectively), so the additives reduced the resistance. The higher the  $H_{max}$  value, the more resistant to deformation the material is. It can also be seen that the samples immersion in H<sub>2</sub>O reduced the  $H_{max}$  more than chlorine, which indicates the greater stiffness of the material in chlorine dilution. On the other hand, the addition of basalt and SiO<sub>2</sub> introduces elements with greater hardness into the material, which increases its resistance to deformation.

The results presented in the  $\eta_{IT}$  [%] column refer to the elastic component of indentation work. The  $\eta_{IT}$  value of all the samples was relatively high, which means that most of the indentation work was used for elastic deformation. The highest  $\eta_{IT}$  value of 35.594% was observed for the PLA\_basalt\_H<sub>2</sub>O sample, so this material has the greatest ability to deform reversibly under pressing. The lowest  $\eta_{IT}$  value of 27.608% was revealed the PLA\_Cl<sub>2</sub> sample, which means its lower elastic deformation capacity.

The analysis showed that the both basalt and SiO<sub>2</sub> modifiers had an impact on the PLA mechanical properties. The addition of basalt slightly shifted the characteristic absorption bands associated with carbonyl ester groups and methyl groups in the FTIR analysis. In turn, SiO<sub>2</sub> affected the intensity and shape of the absorption bands. Basalt facilitated the material strength, which was manifested by a greater force required to break it. Basalt also improved the material elasticity, which manifested itself in greater resistance to deformation and cracking. In turn, the SiO<sub>2</sub> addition had a smaller effect on the elastic and plastic strength of the material. Based on the  $E_{IT}$  results for the tested samples, it can be concluded that basalt as a modifier in the material is relatively stiff. This was proved by the similar  $E_{IT}$  results for the samples immersed in pool water and chlorine. The lower  $E_{IT}$  scores for the silica samples revealed them to be less stiff than the basalt ones, as the higher the  $E_{IT}$ , the stiffer the material. The basalt samples showed the higher instrumental hardness than the samples without the modifier. They also showed a higher elastic force ( $W_{el}$ ), which means they are more resistant to deformation, but at the same time they are less plastic (lower plastic force –  $W_{pl}$ ). In contrast, the silica samples had the lower  $E_{IT}$  values than the basalt ones, thus, silica is less rigid than basalt. The silica sample showed the lowest instrumental hardness, proving its lower resistance to deformation than the other samples. The  $E_{IT}$  values for the samples with basalt were quite similar, so the immersion in chlorine solution had no significant effect on their stiffness. The basalt materials showed the high instrumental hardness, proving their resistance to deformation. The elastic forces ( $W_{el}$ ) for the basalt samples were higher, indicating their greater resistance to deformation. Yet, the plastic forces ( $W_{pl}$ ) were lower, which means the lower plasticity. The silica samples showed the lower instrumental hardness, which means the lower resistance to deformation compared to the basalt samples. In conclusion, in terms of the corrosive environment, the basalt-enhanced materials showed similar stiffness values, regardless of the immersion in different solutions. These materials are relatively stiff and deformation resistant, but less ductile. On the other hand, the silica-enhanced materials are less stiff and less resistant to deformation. Unfortunately, it is not possible to supplement the research results with the mechanical properties of the pure PLA and the PLA doped in the initial state, as these are topics for further research.

## Conclusions

The study aimed to investigate the effects of modifiers, such as basalt and SiO<sub>2</sub>, on the properties of the PLA composite material. The material was obtained through extrusion and 3D printing, and its chemical composition was analyzed using the FTIR spectroscopy. The immersion tests in different solutions revealed that the characteristic absorption bands of the material remained unchanged. The confocal microscopy provided the information on the surface structure of the tested samples. The immersion in water, chlorine, and pool water affected the material mechanical strength and physical properties, due to swelling, dissolution, and hydrolysis. The presence of modifiers influenced the morphological structure. The tribological tests demonstrated that the wear characteristics varied significantly between the samples, hence the modifiers and the solution immersion affected their wear and durability. Basalt enhanced the abrasion resistance, especially in the presence of chlorine, while silica had a positive effect on stiffness. Chlorine and water increased the material stiffness but the modifiers did not significantly affect hardness. The basalt-modified samples showed the higher elastic force and resistance to deformation but lower plasticity. Overall, the modifiers positively influenced the PLA properties, proving a potential for modifying its mechanical strength, chemical resistance, and plasticity. The research findings contributed to improving the 3D printing technology and enhancing the product quality. The results led to the better understanding of the material behavior at a microscopic level, particularly for advanced materials used in water and medical rescue applications.

## Acknowledgments

*The work was carried out as part of the statutory research of the Institute of Biomedical Engineering.*

### ORCID iD

M. Pyza:	 <a href="https://orcid.org/0000-0002-7904-9303">https://orcid.org/0000-0002-7904-9303</a>
N. Brzezińska:	 <a href="https://orcid.org/0000-0002-8648-2498">https://orcid.org/0000-0002-8648-2498</a>
K. Kulińska:	 <a href="https://orcid.org/0000-0002-6676-1502">https://orcid.org/0000-0002-6676-1502</a>
J. Gabor:	 <a href="https://orcid.org/0000-0003-4850-1608">https://orcid.org/0000-0003-4850-1608</a>
A. Barylski:	 <a href="https://orcid.org/0000-0002-1863-1471">https://orcid.org/0000-0002-1863-1471</a>
K. Aniołek:	 <a href="https://orcid.org/0000-0002-5382-2038">https://orcid.org/0000-0002-5382-2038</a>
Ż. Garczyk-Mundała:	 <a href="https://orcid.org/0000-0003-4345-5315">https://orcid.org/0000-0003-4345-5315</a>
K. Adebessin:	 <a href="https://orcid.org/0000-0003-1841-0588">https://orcid.org/0000-0003-1841-0588</a>
A. Swinarew:	 <a href="https://orcid.org/0000-0001-6116-9510">https://orcid.org/0000-0001-6116-9510</a>

## References

- [1] W. Kanabenta, K. Passarapark: 3D printing filaments from plasticized Polyhydroxybutyrate/Poly(lactic acid) blends reinforced with hydroxyapatite. *Additive Manufacturing* (2022). <https://doi.org/10.1016/j.addma.2022.103130>
- [2] V. Nagarajan, A.K. Mohanty, M. Misra: Perspective on Poly(lactic acid) (PLA) based Sustainable Materials for Durable Applications: Focus on Toughness and Heat Resistance. *ACS Sustainable Chemistry & Engineering* 4(6) (2016) 2899-2916. <https://doi.org/10.1021/acssuschemeng.6b00321>
- [3] B. Bax, J. Müssig: Impact and tensile properties of PLA/Cordenka and PLA/flax composites. *Composites Science and Technology* 68 (2008) 1601-1607. <https://doi.org/10.1016/j.compscitech.2008.01.004>
- [4] S. Łabuzek, B. Nowak, J. Pająk, G. Rymarz: Activity of extracellular depolymerase secreted by *Gliocladium solani* strain during "Bionolle®" polyester degradation. *Polimery* 53 (2008) 465-470.
- [5] P. Ruśkowski, A. Gadomska-Gajadur: Polilaktyd w zastosowaniach medycznych: Tworzywa Sztuczne w Przemyśle 2 (2017) 32-35.
- [6] V. Dhand, G. Mittal, K. Yop Rhee et al.: A short review on basalt fiber reinforced polymer composites, *Composites Part B Engineering* 73 (2015) 166-180.
- [7] Yi Zhang, Junrong Yu, Chengjun Zhou et al.: Preparation, morphology, and adhesive and mechanical properties of ultrahigh-molecular-weight polyethylene/SiO<sub>2</sub> nanocomposite fibers. *Polymer Composites* 31(4) (2010) 684-690. <https://doi.org/10.1002/pc.20847>
- [8] A. Ostrowski: Łódź wielofunkcyjna. Zgłoszony: 09.12.2013. Ochronny wzór użytkowy PL 67456.
- [9] H. Czichos, S. Becker, J. Lexow: Multilaboratory tribotesting: results from the VAMAS program on wear test methods. *Wear* 114 (1987) 109-130.
- [10] ASTM Standard G133-05, Standard Test Method for Linearly Reciprocating Ball-on-Flat Sliding Wear, ASTM International, West Conshohocken, PA (2016).
- [11] W.C. Oliver, G.M. Pharr: An improved technique for determining hardness and elastic modulus using load and displacement sensing indentation experiments. *J. of Mater. Res.* 7 (1992) 1564-1583. <https://doi.org/10.1557/JMR.1992.1564>;
- [12] ISO 14577-4, Metallic materials - Instrumented indentation test for hardness and materials parameters - Part 4: Test method for metallic and non-metallic coatings (2016).
- [13] G. Mele, E. Bloise, F. Cosentino et al.: Influence of Cardanol Oil on the Properties of Poly(lactic acid) Films Produced by Melt Extrusion. *ACS Omega* 4(1) (2019) 718-726. DOI: 10.1021/acsomega.8b02880
- [14] <https://www.sciencedirect.com/science/article/abs/pii/S0142941811001899?via%3Dihub>
- [15] B. Wei, S. Song, H. Cao: Strengthening of basalt fibers with nano-SiO<sub>2</sub>-epoxy composite coating. *Materials & Design* 32(8-9) (2011) 4180-4186. doi: <https://doi.org/10.1016/j.matdes.2011.04.041>
- [16] G.H. Yew, A.M. Mohd Yusof, Z.A. Mohd Ishak et al.: Water absorption and enzymatic degradation of poly(lactic acid)/rice starch composites. *Polymer Degradation and Stability* 90(3) (2005) 488-500. <https://doi.org/10.1016/j.polyimdegradstab.2005.04.006>
- [17] G.L. Siparsky, K.J. Voorhees, J.R. Dorgan et al.: Water transport in poly(lactic acid) (PLA), PLA/ polycaprolactone copolymers, and PLA/polyethylene glycol blends. *J Environ Polym Degr* 5 (1997) 125-136. <https://doi.org/10.1007/BF02763656G>
- [18] F. Iñiguez-Franco, R. Auras, G. Burgess et al.: Concurrent solvent induced crystallization and hydrolytic degradation of PLA by water-ethanol solutions. *Polymer* 99 (2016) 315-323. <https://doi.org/10.1016/j.polymer.2016.07.018>
- [19] J.C. Fleischer, J.C. Diehl, L.S.G.L. Wauben et al.: The Effect of Chemical Cleaning on Mechanical Properties of Three-Dimensional Printed Poly(lactic acid). *J. Med. Device* 14(1) (2020) 011109. doi: 10.1115/1.4046120
- [20] S.R. Subramaniam, M. Samykan, S.K. Selvamani, et al.: Preliminary investigations of poly(lactic acid) (PLA) properties. *AIP Conference* 2059(1) (2019) 020038. <https://doi.org/10.1063/1.5085981>
- [21] M.M. Hanon, M. Kovács, L. Zsidai: Tribology behaviour investigation of 3D printed polymers, *International Review of Applied Sciences and Engineering* 10(2) (2019) 173-181. <https://doi.org/10.1556/1848.2019.0021>